The Spatial State of Non-Interacting Photons

by

Megan Agnew

Submitted for the degree of
Doctor of Philosophy

Heriot-Watt University
School of Engineering and Physical Sciences
May 2018

Abstract

High-dimensional quantum systems are becoming an increasingly important area of study. Due to their ability to encode more information than a two-dimensional system, high-dimensional systems are useful in many applications, from quantum communication to quantum computing. In particular, spatial states of light, such as orbital angular momentum and spatial position, are inherently high-dimensional by nature and lend themselves well to manipulation and measurement. As light is commonly used in communication applications, spatial states could extend the information capacity of quantum communication and make it easier to detect eavesdroppers in the system.

This thesis comprises four experiments in which the spatial state of photons is manipulated and measured. The first experiment describes a filter for two-dimensional anti-symmetric spatial states. We use a pair of photons entangled in multiple orbital angular momentum states in order to test the filter. We are able to manipulate which two-dimensional subspaces are in symmetric states and which are in anti-symmetric states, and as such we are able to filter out particular subspaces, effectively engineering high-dimensional states via Hong-Ou-Mandel interference.

In the second experiment, we use the anti-symmetric state filter in a four-photon system. We begin with two pairs of photons, with entanglement within the pairs but not between the pairs. Combining one photon from each pair in our anti-symmetric state filter, we create entanglement between the other two photons, achieving entanglement swapping. Additionally, due to the two-dimensional nature of the filter, we transcribe entanglement into several two-dimensional subspaces in the process.

In the third experiment, we investigate the quantum teleportation that occurs as a side effect of the entanglement swapping. We demonstrate teleportation of several two-dimensional OAM states, and we describe the result of attempted high-dimensional teleportation.

In the fourth and final experiment, we turn our attention from the OAM of light to the spatial position of light. Using our four-photon system and anti-symmetric state filter, we demonstrate ghost imaging between photons that have never interacted. This is enabled by taking advantage of the correlations produced when entanglement swapping occurs in the filter.

Beam me up, Scotty.

– An apocryphal quote attributed to Captain Kirk, *Star Trek*

Acknowledgements

First, I would like to thank my supervisor, Jonathan Leach, for providing me the opportunity to do cool research and the guidance to complete my PhD. I also offer thanks to my fellow group members for their help and support throughout my time at Heriot-Watt. I have greatly appreciated the insight provided by my colleagues in South Africa who collaborated on all of the work in this thesis.

I would also like to thank all of my friends for the support during my degree and the much-needed distraction from my work. In particular, Sporran has done an excellent job of setting me straight when it felt like my PhD would never end. I'd also like to thank Duncan for his patience and support during the writing of my thesis.

My final thanks, as always, is reserved for my mom, my dad, and my sister, without whom I could never have come this far. I am also forever grateful to Theo for helping me through every difficult moment in the past few years.

Table of Contents

List of Tables viii

List of Figures ix

List of Publications xi

1 Introduction 1

1.1 Quantum States . . . 4

1.1.1 Qubits . . . 4

1.1.2 Mixed States . . . 5

1.1.3 Qudits . . . 8

1.1.4 Multiple Particles . . . 10

1.2 Manipulation of Quantum States . . . 10

1.2.1 Operators . . . 11

1.2.2 Projective Measurements . . . 11

1.2.3 Partial Trace . . . 13

1.2.4 Measuring OAM . . . 13

1.3 Tomography . . . 18

1.3.1 Maximum Likelihood Estimation . . . 21

1.3.2 Example Data . . . 22

1.3.3 Fidelity . . . 23

1.4 Entanglement . . . 25

1.4.1 Mathematical Description of Entanglement . . . 27

1.4.2 Bell States . . . 27

1.4.3 Producing Entanglement . . . 29

1.4.4 Remote State Preparation 31
1.4.5 Concurrence 32
1.5 Hong-Ou-Mandel Interference 33
1.5.1 Mathematical Description 34
1.5.2 Bell State Measurements 35
1.5.3 Quantum Teleportation 38
1.5.4 Entanglement Swapping 41

2 Engineering Two-Photon High-Dimensional States through Quantum Interference 44
2.1 Notes and Acknowledgements 44
2.2 Overview 45
2.3 Background 45
2.4 Anti-Symmetric State Filter 46
2.5 State Preparation 49
2.6 Hong-Ou-Mandel Interference 52
2.7 Summary of Experimental Methods 53
2.8 Results 54
2.9 Discussion 59

3 Entanglement Swapping of Orbital Angular Momentum States 60
3.1 Notes and Acknowledgements 60
3.2 Overview 61
3.3 Background 61
3.4 Entanglement Swapping in High Dimensions 62
3.5 Experiment 73
3.6 Results 76
3.6.1 Estimation of Four-Dimensional State 80
3.7 Background Subtraction 82
3.7.1 Expected 4-Way Coincidence 82
3.7.2 Background of 4-Way Coincidence 84
3.7.3 Impact of Background Subtraction 84
3.8 Pure Final State 85

4 Teleportation of Multiple Orbital Angular Momentum States of Light **87**

4.1 Notes and Acknowledgements 87

4.2 Overview 88

4.3 Background 88

4.4 Theory 89

4.5 Experiment 91

4.6 Results 92

4.7 Conclusions 97

5 Ghost Imaging Using Photons that Have Not Interacted **98**

5.1 Notes and Acknowledgements 98

5.2 Overview 99

5.3 Background 99

5.4 Theory 102

5.5 Experiment 104

5.6 Results 105

5.7 Discussion 106

5.7.1 Expected Counts 107

6 Conclusions **110**

APPENDICES **112**

A Aligning a four-photon system **113**

A.1 Upconversion 113

A.2 Downconversion 114

A.3 Back-Alignment 118

A.4 Finding the Coincidences 118

A.5 Turning on the SLMs 121

A.6 Bringing It All Together 122

References **123**

List of Tables

1.1 Example tomography data. 23

2.1 The trace of each subspace $\rho_{\ell-\ell}$ before and after the filter 59

3.1 Measures of entanglement 79

3.2 Raw count rates 83

3.3 Raw vs. background-subtracted 85

4.1 Fidelity of teleported qubits 94

4.2 Fidelity of teleported qubits (continued) 95

4.3 Average fidelities of teleported qubits. 95

List of Figures

1.1 Example density matrices 6
1.2 The Bloch sphere 7
1.3 Orbital angular momentum 10
1.4 Plane waves 14
1.5 OAM mode sorter 16
1.6 Measurement of OAM 18
1.7 Spatial light modulator 19
1.8 Density matrices of Bell states 28
1.9 Conservation rules 29
1.10 OAM entanglement 30
1.11 OAM distribution 30
1.12 Remote state preparation 32
1.13 Concurrence vs. probability 33
1.14 Beamsplitter modes 34
1.15 Bell state behaviour at a beamsplitter 37
1.16 Bell state measurement 37
1.17 Quantum vs. regular teleportation 38
1.18 Teleportation 40
1.19 Entanglement swapping 42

2.1 Behaviour of orbital angular momentum in a beamsplitter 47
2.2 Dove prism 50
2.3 High-dimensional Hong-Ou-Mandel setup 52
2.4 Photon coincidence counts measured as a function of the path length difference 55

2.5 Coincidence counts as a function of input state 56
2.6 The high-dimensional density matrices corresponding to the state before and after the filter 57
2.7 Two-dimensional density matrices 58

3.1 A conceptual diagram of entanglement swapping 62
3.2 Terms in entanglement swapping calculation 63
3.3 Transcription of entanglement 72
3.4 Experimental setup 74
3.5 Hong-Ou-Mandel (HOM) interference 76
3.6 Two-dimensional density matrices 77
3.7 Fidelity vs. visibility 79
3.8 Experimentally measured OAM distribution 80
3.9 Four-dimensional density matrix 81
3.10 Background subtraction 83

4.1 Teleportation using remote state preparation 91
4.2 Teleported qubit states. 93

5.1 Methods of ghost imaging 100
5.2 Two-photon vs. four-photon ghost imaging 101
5.3 Hong-Ou-Mandel dip 105
5.4 Contrast-reversed image 106
5.5 Comparison between expected and measured counts 108
5.6 Coincidences vs. UV pump power 108
5.7 Variation of expected counts by pixel 109

A.1 Alignment apertures 116
A.2 When to touch which mirrors 119

List of Publications

Papers

1. Y. Zhang*, M. Agnew*, T. Roger, F.S. Roux, T. Konrad, D. Faccio, J. Leach, A. Forbes, *Simultaneous entanglement swapping of multiple orbital angular momentum states of light*, Nature Communications **8**, 632 (2017).
   *These authors contributed equally to this work.

2. L. Mertens, M. Sonnleitner, J. Leach, M. Agnew, M.J. Padgett, *Image reconstruction from photon sparse data*, Scientific Reports **7**, 42164 (2017).

3. Y. Zhang, F.S. Roux, T. Konrad, M. Agnew, J. Leach, A. Forbes, *Engineering two-photon high-dimensional states through quantum interference*, Science Advances **2**, e1501165 (2016).

First author conference contributions

1. M. Agnew, N. Bornman, D. Faccio, A. Forbes, J. Leach, *Ghost imaging using photons that have not interacted*. Poster, ICOAM, Italy (September 2017).

2. M. Agnew, Y. Zhang, T. Roger, F.S. Roux, T. Konrad, D. Faccio, J. Leach, A. Forbes, *Entanglement swapping of orbital angular momentum states*. Oral presentation, Photon 16, Leeds, UK (September 2016).

3. M. Agnew, F. Tonolini, S. Chan, A. Lindsey, J. Leach, *Compressive sensing of orbital angular momentum states*. Oral presentation, ICOAM, New York (August 2015).

4. M. Agnew, E. Bolduc, K. Resch, S. Franke-Arnold, J. Leach. *Discriminating single-photon states unambiguously in high dimensions*. Invited oral presentation, Symposium on structured light and orthogonality in imaging, Rank Prize Funds (November 2014).

5. M. Agnew, E. Bolduc, K. Resch, S. Franke-Arnold, J. Leach. *Discriminating single-photon states unambiguously in high dimensions*. Oral presentation, Photon 14 (September 2014).

Chapter 1

Introduction

The strange nature of quantum mechanics – the theory governing the behaviour of sub-atomic particles – was discussed in the early 20^{th} century by Einstein, Podolsky, and Rosen in their seminal paper on entanglement [1]. It examined whether the theory of quantum mechanics was complete under the assumption of local realism. Local realism is a principle true in classical physics, combining the ideas of locality (that effects of actions are limited to the speed of light) and realism (that an object must have a pre-existing value that is revealed upon measurement). The authors argue that quantum mechanics could not be complete if local realism were true.

This of course does not seem so paradoxical today: it has since become clear that local realism does not apply to quantum mechanics. In particular, Bell and others [2, 3] provided stringent bounds for quantum mechanical systems that could be described by local hidden variables; these bounds are often referred to as Bell inequalities. A violation of these inequalities invalidates local hidden variable theories in the quantum realm, and thus also local realism. Violations have been demonstrated experimentally many times [4–9], including violations in which there were no possible loopholes in the experiment [10, 11].

Since these early forays into the nature of quantum mechanics, the field has matured from foundations to applications. Nowadays, quantum science is an extensive field of research that encompasses a wide range of topics: fundamental research into the reality of the wavefunction and causality (see, for example, [12–14]); laboratory experiments taking the first steps toward real-world applications; and technologies that are at or near market readiness.

One of the most intriguing technologies arising from quantum mechanics is quantum computing. The principles of superposition and entanglement enable advantages in tasks a classical computer struggles with [15]. An excellent example of this is factoring large numbers: classical computers are so inept at this task that we use this fact as a basis for encryption. Using Shor's algorithm [16], a quantum computer

can theoretically complete this task in a fraction of the time a classical computer would take, rendering many of our current encryption protocols effectively useless. Quantum computers with significant computing power, however, are a long way off yet; so far, quantum computers have been small [17–21], and the highest number factored to date using Shor's algorithm is twenty-one [22].

Quantum communication, on the other hand, is an advanced field with commercial products already available. This field encompasses mature technologies such as quantum cryptography [23, 24], implementations of which are already on the market, to younger technologies such as entanglement swapping [25], which has been performed in laboratories [26–30] but is not ready for general use.

Quantum communication usually uses light as its carrier of information due to its naturally high speed of transmission. Most mature technologies use the polarisation of light due to the ease of manipulating it. However, other degrees of freedom are providing promising avenues for more efficient communication. For example, spatial modes have the advantage of being scalable to higher dimensions [9, 31–35]. Similarly, encoding information in photon arrival time provides access to higher dimensions (though not as easily as with spatial modes) as well as being less vulnerable to mixing between the modes [36–42].

There are many communication protocols that are only made possible using quantum mechanics. One of these is dense coding [43], which uses entanglement to send two bits of information on a single qubit. In practice, the best information capacity achieved is 1.58 bits per qubit [44]; by using ancillary entanglement, a channel capacity of 1.63 bits has been achieved [45]. This is due to the difficulty in measuring entangled states; with linear optics, it is not possible to distinguish all four maximally entangled states, meaning that the theoretical limit of two bits cannot be reached [46].

Quantum mechanics also enables rapid sharing of one-time-use secret keys, allowing more secure encryption than classical encryption. Quantum key distribution (QKD) can be accomplished in a number of ways. The most commonly known protocols are BB84 [47] and E91 [48]. The BB84 protocol involves one party, Alice, encoding a random bit in a randomly chosen basis and sending the encoded photon to a recipient, Bob. Bob then measures the photon in a randomly chosen basis and records the result. After many iterations of this, Alice and Bob publicly share which bases they encoded/measured in. They discard any result for which the bases don't match, and the remainder becomes their secret key. No one else can have this information: if an eavesdropper attempts to intercept it, then some of Bob's results will not match Alice's even when their bases match, and a public comparison of a fraction of the measurements will reveal the presence of an eavesdropper. The E91 protocol works in a very similar fashion, except that it uses two entangled photons,

and Alice and Bob are both making measurements.

An interesting phenomenon that originally was thought to arise from quantum mechanics is termed *ghost imaging* [49]. It originally required spatially entangled photons, one incident on an object and bucket detector and one incident on a spatially resolving detector but not encountering the object. Using the correlations between the two photons, it was possible to create an image of the object, despite the light striking the object never encountering a spatially resolving detector, and the light striking the spatially resolving detector never encountering the object. However, it was later discovered that this could be done without the entanglement; in fact, simply creating two correlated beams of classical light was sufficient [50].

Arguably the most well-known application of quantum mechanics is quantum teleportation [51]. While Star Trek and other science fiction media have popularised the concept of teleportation to move a person instantly from one location to another, this is unfortunately not what quantum teleportation allows. However, using a pair of entangled photons in addition to the photon we would like to teleport, we can move the *information* from one photon to another instantly, even when the original photon and the new photon are spatially separated. However, due to the no-cloning theorem, this necessarily destroys the initial state. Quantum teleportation has been demonstrated experimentally in many systems, including polarisation [52], and most recently both the polarisation and spatial mode of a single photon [53,54]. Teleportation has been performed in both free space [55–57] and fibre [58–61] and, in an experiment gaining wide (and often inaccurate) press coverage, to a satellite [62].

This thesis is largely based on the interaction that allows quantum teleportation to occur: Hong-Ou-Mandel (HOM) interference [63]. One of the less intuitive parts of quantum optics, HOM interference occurs when two photons arrive at the two input ports of a beamsplitter at the same time. As long as the two photons are completely indistinguishable – in polarisation, spatial mode, time of arrival, etc. – then they will both leave the beamsplitter in the same output port. This is in contrast to classical light or even two distinguishable photons, which will sometimes leave in the same output port but an equal amount of the time will leave from opposite output ports. The strange behaviour of indistinguishable photons gives rise to several of the most fascinating applications of quantum technology, including teleportation and entanglement swapping.

In this thesis, we explore the HOM interference of photons in particular spatial modes referred to as orbital angular momentum (OAM) modes [64–66]. OAM is becoming an increasingly important property in which to encode information – in both classical and quantum regimes. One of the main advantages of OAM is that it is in principle infinite-dimensional; unlike polarisation, which can only take on one of two possible states, OAM exists in a high-dimensional (but discrete) state

space. This allows encoding of more information on a single photon, expanding our information capacity from one bit per photon (e.g., the two states of polarisation) to many bits per photon (e.g., 16 OAM modes resulting in 4 bits per photon).

In Chapter 1, we first discuss in more detail the topics we have touched on here: quantum states, entanglement, and HOM interference. In Chapter 2, we examine the behaviour of two photons entangled in their OAM undergoing HOM interference. Then we use the knowledge gained from Chapter 2 to expand our experiment to four photons: we use two entangled pairs and send one photon from each pair to a beamsplitter to undergo HOM interference. This allows us to measure entanglement swapping of OAM states in Chapter 3 and teleportation of OAM states in Chapter 4. Finally, we look at spatial modes more generally, using four photons (two pairs each entangled in the position basis) to perform entanglement swapping as in Chapter 3, but this time using the resulting correlations to create a ghost image of an object in Chapter 5.

1.1 Quantum States

The key building block of any quantum process is the quantum state. A quantum state completely describes the behaviour of a quantum particle. However, this behaviour is inherently probabilistic, meaning that we cannot always predict the result of a measurement. The quantum state of a particle is described by a wavefunction ψ, which can be denoted in Dirac notation as a vector $|\psi\rangle$ in the d-dimensional Hilbert space $\mathcal{H}^d$.

1.1.1 Qubits

A two-dimensional state space has the basis vectors

$$|0\rangle = \begin{pmatrix} 1 \\ 0 \end{pmatrix}; \;\; |1\rangle = \begin{pmatrix} 0 \\ 1 \end{pmatrix}. \tag{1.1}$$

A particle existing in this space is referred to as a qubit. Any pure qubit state $|\psi\rangle$ can then be described as a superposition of these two states

$$|\psi\rangle = \alpha|0\rangle + \beta|1\rangle, \tag{1.2}$$

where α and β are complex numbers, and $|\alpha|^2$ ($|\beta|^2$) denotes the probability of finding the particle in state $|0\rangle$ ($|1\rangle$). As probabilities must sum to unity, the state must be normalised such that $|\alpha|^2 + |\beta|^2 = 1$.

The polarisation of a single photon is an example of a qubit state. Typical basis states for polarisation are horizontally polarised light ($|H\rangle$) and vertically polarised

light ($|V\rangle$). Thus any pure polarisation state can be represented by

$$|\psi\rangle = \alpha|H\rangle + \beta|V\rangle. \tag{1.3}$$

Recall that α and β can be complex numbers, allowing the description of right- and left-circular polarisations $\big(|R\rangle = (|H\rangle + i|V\rangle)/\sqrt{2}$ and $|L\rangle = (|H\rangle - i|V\rangle)/\sqrt{2}$, respectively$\big)$ in addition to linear polarisation states $\big(|D\rangle = (|H\rangle + |V\rangle)/\sqrt{2}$ and $|A\rangle = (|H\rangle - |V\rangle)/\sqrt{2}\big)$.

Qubits are the building blocks of quantum information science, including important applications such as quantum computing [17–22, 67–70] and quantum cryptography [43, 47, 48, 71–76]. Many different systems and degrees of freedom make use of qubits, including the polarisation of light [52], spatial modes of light [77], photon arrival time [36], electron spin [78], nuclear spin [79], and superconducting circuits [80].

1.1.2 Mixed States

Not all particles can be described by a pure state as above. A pure state describes a superposition of states, such as diagonally polarised light, which is in an equal superposition of horizontally and vertically polarised light $|D\rangle = (|H\rangle + |V\rangle)/\sqrt{2}$. However, it is possible to have a particle in a statistical mixture of states; for example, a light source might have a probability p of emitting horizontally polarised light and a probability $1-p$ of emitting vertically polarised light. This kind of state cannot be described simply with vectors; we require a different description called a density matrix, typically denoted ρ.

The density matrix of a pure state is simply the outer product of the state $|\psi\rangle\langle\psi|$. A mixed state is then the weighted sum of several pure density matrices

$$\rho = \sum_i p_i |\psi_i\rangle\langle\psi_i|, \tag{1.4}$$

where p_i is the probability of finding the particle in state $|\psi_i\rangle$, and $\sum_i p_i = 1$.

For a qubit, the state is described by a 2×2 density matrix. For example, the mixed state mentioned above would be described by the density matrix

$$\begin{aligned} \rho &= p|H\rangle\langle H| + (1-p)|V\rangle\langle V| \\ &= \begin{pmatrix} p & 0 \\ 0 & 1-p \end{pmatrix}. \end{aligned} \tag{1.5}$$

This state cannot be represented as a pure state vector, thus requiring the density matrix description.

A density matrix by definition has several properties:

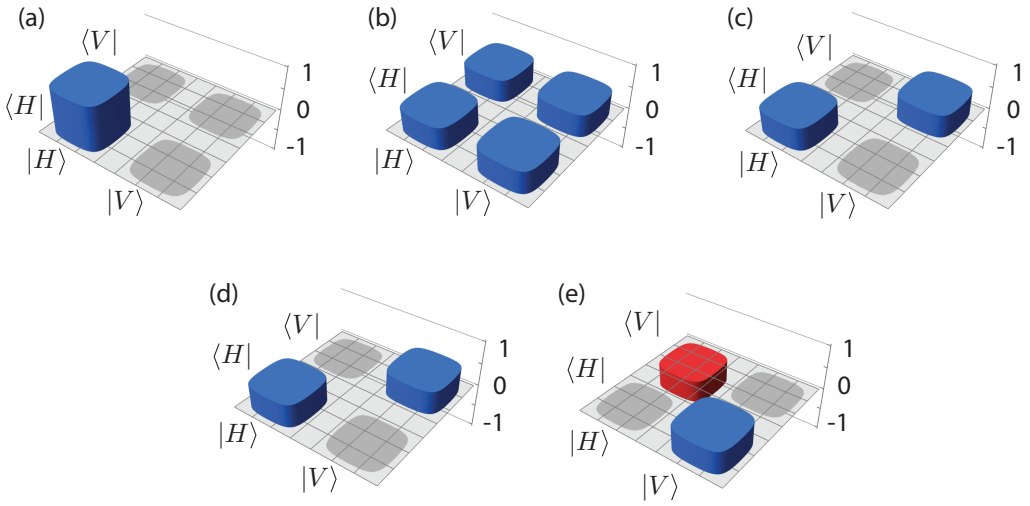

Figure 1.1: **Example density matrices.** (a) Horizontally polarised pure state. (b) Diagonally polarised pure state. (c) Mixed state of Eq. (1.5) with $p = 0.5$. (d) The real part of a right-circularly polarised pure state. (e) The imaginary part of a right-circularly polarised pure state. In all cases, blue bars indicate positive values, while red bars indicate negative values. Grey bars indicate zero values.

1. It must have unit trace. The trace of a quantum state ρ in a state space with basis $\{|0\rangle, |1\rangle, ..., |d\rangle\}$ is defined as

$$\mathrm{Tr}(\rho) = \sum_{i=0}^{d} \langle i|\rho|i\rangle. \tag{1.6}$$

   Thus the trace is the sum of all possible measurements in a particular basis, which must of course be equal to unity.

2. It must be Hermitian, i.e., it must equal its complex conjugate ($\rho = \rho^\dagger$).

3. It must be positive semi-definite. A positive semi-definite matrix satisfies the condition $\langle\psi|\rho|\psi\rangle \geq 0$ for all $|\psi\rangle$; i.e., any projective measurement results in a non-negative outcome. This is equivalent to all the eigenvalues of ρ being non-negative.

Fig. 1.1 shows several qubit density matrices in graphical form for illustration. This is how the majority of matrices will be presented in this thesis. The diagonal of the density matrix is oriented horizontally; the left-most bar represents the top-left element of the matrix, and the right-most bar represents the bottom-right element of the matrix. Each bar's height indicates the value of the corresponding matrix element.

Fig. 1.1(a) and (b) represent pure states $|H\rangle$ and $|D\rangle$, while Fig. 1.1(c) represents the mixed state in Eq. (1.5). All three of these show only the real portions of the matrices; the imaginary portions are expected to be zero. Fig. 1.1(d) and (e) show

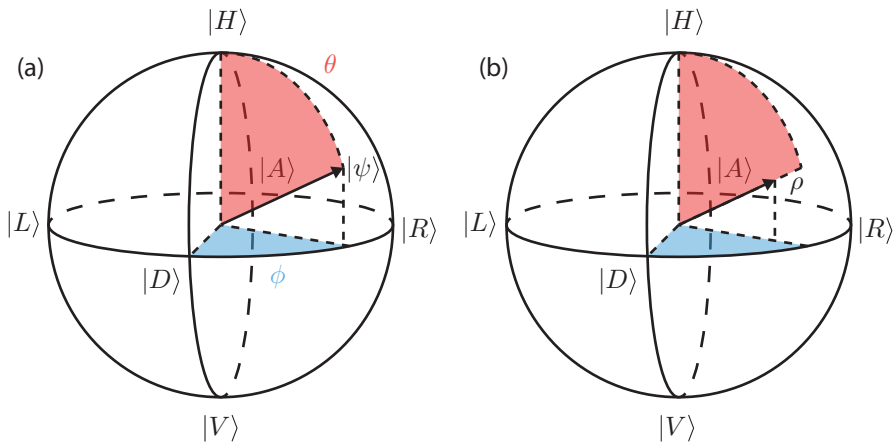

Figure 1.2: **The Bloch sphere.** (a) A pure state on the surface of the Bloch sphere. (b) A mixed state inside the Bloch sphere.

the real and imaginary parts, respectively, of the pure state $|R\rangle$. Note that the mixed state (c) and the real part of $|R\rangle$ (d) are identical; it is only upon examining the imaginary components that we find that the two states are very different.

Bloch Sphere

It is instructive at this point to introduce the Bloch sphere. This is a means of visualising all possible qubit states: pure and mixed. It can be defined as follows [15].

Consider a pure qubit state as in Eq. (1.3); we will use polarisation states for simplicity. We know the coefficients α and β are complex; however, we can factor out a common phase between the two coefficients, resulting in a global phase that can be ignored. Then we can assume one of the coefficients α is real and non-negative, with the remaining phase part of the other coefficient β. Along with the knowledge that $|\alpha|^2 + |\beta|^2 = 1$, we can parametrise the state as

$$|\psi\rangle = \cos\left(\frac{\theta}{2}\right)|H\rangle + e^{i\phi}\sin\left(\frac{\theta}{2}\right)|V\rangle, \tag{1.7}$$

where $0 \leq \theta \leq \pi$ and $0 \leq \phi < 2\pi$. Each pure state $|\psi\rangle$ can then be represented by a position on the unit sphere defined by the vector

$$\vec{a} = (\sin\theta\cos\phi,\ \sin\theta\sin\phi,\ \cos\theta). \tag{1.8}$$

Note that $|\vec{a}| = 1$, meaning that any pure state will be situated on the surface of the Bloch sphere, as shown in Fig. 1.2(a).

We can extend this definition to mixed states by considering the general representation of a qubit density matrix

$$\rho = (\mathbb{1} + \vec{a}\cdot\vec{\sigma})/2, \tag{1.9}$$

where $\vec{a} = (a_1, a_2, a_3)$ is not necessarily of the form (1.8). We also introduce $\vec{\sigma} = (\sigma_x, \sigma_y, \sigma_z)$, which are the Pauli matrix operations

$$\sigma_x = \begin{pmatrix} 0 & 1 \\ 1 & 0 \end{pmatrix} \tag{1.10}$$

$$\sigma_y = \begin{pmatrix} 0 & -i \\ i & 0 \end{pmatrix} \tag{1.11}$$

$$\sigma_z = \begin{pmatrix} 1 & 0 \\ 0 & -1 \end{pmatrix}. \tag{1.12}$$

Thus the general density matrix is given by

$$\rho = \frac{1}{2} \begin{pmatrix} 1 + a_2 & a_1 - ia_3 \\ a_1 + ia_3 & 1 - a_2 \end{pmatrix}, \tag{1.13}$$

which for a pure state becomes

$$\rho_{\text{pure}} = \frac{1}{2} \begin{pmatrix} 1 + \sin\theta \sin\phi & \sin\theta \cos\phi - i\cos\theta \\ \sin\theta \cos\phi + i\cos\theta & 1 - \sin\theta \sin\phi \end{pmatrix}. \tag{1.14}$$

Note that the eigenvalues of the matrix ρ are $(1 \pm |\vec{a}|)/2$. However, we know that any physical density matrix must have non-negative eigenvalues, i.e., $(1 \pm |\vec{a}|)/2 \geq 0$, meaning that $|\vec{a}| \leq 1$. For pure states, $|\vec{a}| = 1$; thus we can see that any mixed state will be situated within the unit sphere, as shown in Fig. 1.2(b).

1.1.3 Qudits

So far, we have only discussed quantum systems that have two possible states and exist in a two-dimensional space. We can extend this concept to systems that have more than two possible states and exist in high-dimensional spaces. A state in a high-dimensional space is referred to as a qudit.

A pure qudit state can be described as a superposition of d basis states $|\psi\rangle = \sum_{i=0}^{d-1} c_i |i\rangle$, where $|c_i|^2$ is the probability of finding the particle in state $|i\rangle$, and $\sum_{i=0}^{d-1} |c_i|^2 = 1$. For example, a three-dimensional state (qutrit) exists in the basis

$$|0\rangle = \begin{pmatrix} 1 \\ 0 \\ 0 \end{pmatrix}; \;\; |1\rangle = \begin{pmatrix} 0 \\ 1 \\ 0 \end{pmatrix}; \;\; |2\rangle = \begin{pmatrix} 0 \\ 0 \\ 1 \end{pmatrix}. \tag{1.15}$$

Any pure qutrit state $|\psi\rangle$ can then be described as a superposition of these three states

$$|\psi\rangle = \alpha|0\rangle + \beta|1\rangle + \gamma|2\rangle, \tag{1.16}$$

where as always $|\alpha|^2 + |\beta|^2 + |\gamma|^2 = 1$. We can also have mixed states in high dimensions, which are described by $d \times d$ density matrices.

Orbital Angular Momentum

One high-dimensional property of light is the orbital angular momentum (OAM) of a photon, which is commonly used to define qudit states. The electric and magnetic fields of light give rise to the Poynting vector, defined as the cross product between the two. This vector is then perpendicular to the phasefront of the light; it points along the direction of energy propagation. For a plane wave, it points parallel to the axis of propagation of the light. For a helical phase structure, the Poynting vector spirals around the light's axis of propagation. It is this azimuthal nature of the Poynting vector that gives rise to orbital angular momentum.

There are a range of modes of light that are solutions to Maxwell's equations and also contain OAM. These include the Laguerre-Gaussian (LG) modes of light and Bessel modes, both of which are defined by two indices: a radial and azimuthal index. This thesis concerns modes of light where we integrate over the radial index, as we are only interested in the effects of the azimuthal index, typically denoted ℓ. These modes of light have an $e^{i\ell\phi}$ phase component, which we use to define an OAM state.

Light with OAM $\ell\hbar$ per photon can be written as the quantum state $|\ell\rangle$. As OAM is quantised, the index ℓ can be any integer number, positive, negative, or zero. Thus, the OAM state of light is a qudit; any pure OAM state can be described as

$$|\Psi\rangle = \sum_{\ell=-\infty}^{\infty} a_\ell |\ell\rangle, \tag{1.17}$$

where $|a_\ell|^2$ is the probability of the photon having OAM $\ell\hbar$.

The helical phase structure of OAM is shown in Fig. 1.3(a) for a variety of OAM values, including the Gaussian mode $\ell = 0$. Taking a cross-section of the phase perpendicular to the direction of propagation, we see that the phase goes through the range 0 to 2π ℓ times, as shown in Fig. 1.3(b). However, as the phase changes azimuthally, the centre of the beam has an undefined phase where all the phases converge, resulting in a dislocation. There can be no intensity at a phase dislocation, and thus beams with nonzero OAM are ring-shaped, as shown in Fig. 1.3(c).

Orbital angular momentum has been investigated as a high-dimensional system both in classical applications [66, 81–84] and in quantum information science [9, 31–33, 85–96]. OAM has been shown to increase information capacity in quantum cryptographic systems [97–99], and quantum memories for OAM are being developed with a view to enable long-distance communication [100, 101].

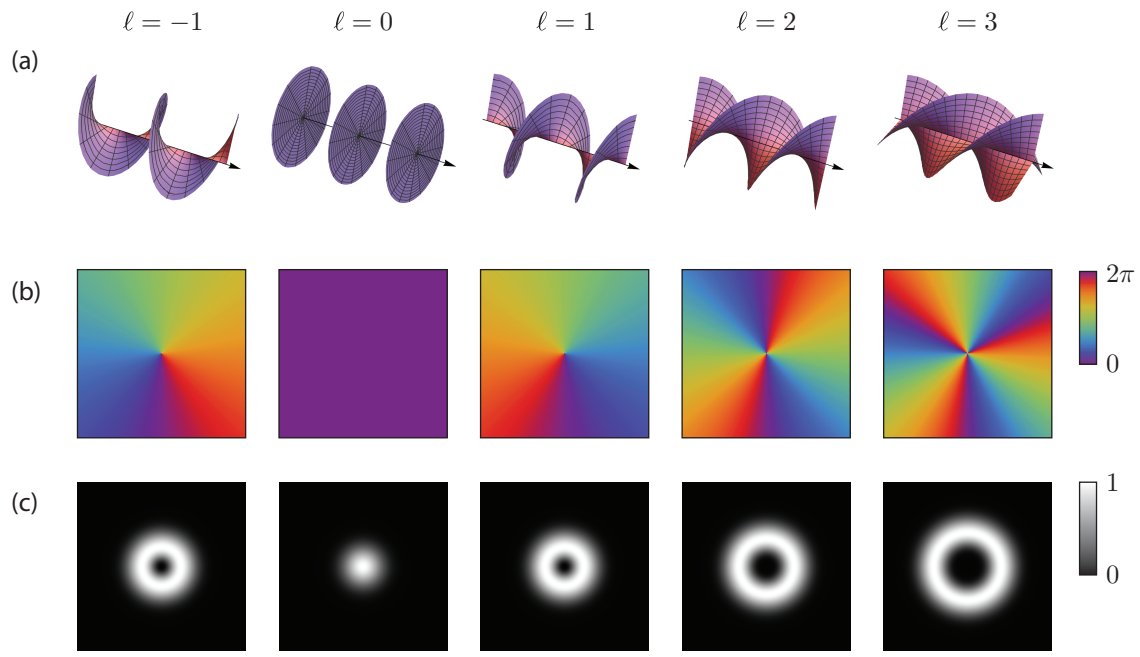

Figure 1.3: **Orbital angular momentum.** (a) Surfaces of constant phase. (b) Cross-section of phase perpendicular to the direction of propagation. (c) Intensity.

1.1.4 Multiple Particles

We can also describe the quantum state of multiple particles; to do this, we use the tensor product of each particle's state. For example, one particle in the state $|\psi_1\rangle \in \mathcal{H}_1^{d_1}$ and a second particle in the state $|\psi_2\rangle \in \mathcal{H}_2^{d_2}$ would be in the combined state $|\psi_1\rangle \otimes |\psi_2\rangle \in \mathcal{H}_1^{d_1} \otimes \mathcal{H}_2^{d_2}$. This is frequently denoted as $|\psi_1\rangle|\psi_2\rangle$ for simplicity.

In general, it is not necessarily possible to write a multi-particle state as the tensor product of the constituent states; we will explore this possibility further in the next section. A more general description of a multi-particle state can be given by realising the basis of the combined Hilbert space $\mathcal{H}_1^{d_1} \otimes \mathcal{H}_2^{d_2}$ consists of tensor products of all the basis states in each constituent Hilbert space. Thus any two-particle pure state can be described by

$$|\psi\rangle = \sum_{j=1}^{d_1} \sum_{k=1}^{d_2} c_{jk} |j\rangle|k\rangle, \tag{1.18}$$

where $\{|j\rangle\}$ and $\{|k\rangle\}$ represent the basis states of the two Hilbert spaces and $|c_{jk}|^2$ is the probability of finding the particles in the combined state $|j\rangle|k\rangle$.

1.2 Manipulation of Quantum States

In order to use quantum states in research, as well as in real-world applications, we must be able to verify what quantum state we are working with. We can do this by

performing various operations on the state in order to manipulate and characterise it.

1.2.1 Operators

Any process $\mathcal{E}$ acting on a state ρ can be represented as

$$\mathcal{E}(\rho) = \sum_k \hat{E}_k \rho \hat{E}_k^\dagger, \tag{1.19}$$

where $\{\hat{E}_k\}$ are operators that act on the state space of ρ.

The resultant matrix $\rho' = \mathcal{E}(\rho)$ must be a physical density matrix with unit trace such that

$$\begin{aligned} 1 &= \mathrm{Tr}(\mathcal{E}(\rho)) && (1.20)\\ &= \mathrm{Tr}\left(\sum_k \hat{E}_k \rho \hat{E}_k^\dagger\right) && (1.21)\\ &= \sum_k \mathrm{Tr}\left(\hat{E}_k \rho \hat{E}_k^\dagger\right) && (1.22)\\ &= \sum_k \mathrm{Tr}\left(\hat{E}_k^\dagger \hat{E}_k \rho\right) && (1.23)\\ &= \mathrm{Tr}\left(\sum_k \hat{E}_k^\dagger \hat{E}_k \rho\right). && (1.24) \end{aligned}$$

From this, as $\mathrm{Tr}(\rho) = 1$, we deduce that $\sum_k \hat{E}_k^\dagger \hat{E}_k = \mathbb{1}$. This is called the completeness relation and requires the map $\mathcal{E}$ to be trace-preserving.

1.2.2 Projective Measurements

The most common and versatile type of measurement in quantum mechanics is the projective measurement, so named because the operator applied to the system of interest is a projector. A projector $\Pi_m = |m\rangle\langle m|$ projects a system into the state $|m\rangle$. This type of measurement is important as it is used often to obtain the probability of a particular outcome.

A projector can be thought of as a single operator $\hat{E}_k$ that operates on a state in the same way as a quantum process; however, we must divide by the trace of the final state as a single operator is not necessarily trace-preserving. Thus a projective

measurement has the following effect on a system [15]:

$$\begin{aligned}\rho' &= \frac{\Pi_m \rho \Pi_m^\dagger}{\mathrm{Tr}(\Pi_m \rho \Pi_m^\dagger)} \\ &= \frac{|m\rangle\langle m|\rho|m\rangle\langle m|}{\mathrm{Tr}(\Pi_m^\dagger \Pi_m \rho)} \\ &= \frac{|m\rangle \mathrm{Tr}(\Pi_m \rho)\langle m|}{\mathrm{Tr}(\Pi_m \rho)} \\ &= |m\rangle\langle m|, \end{aligned} \tag{1.25}$$

where we have used the cyclic property of the trace and the fact that $\Pi_m^\dagger \Pi_m = \Pi_m$. Thus after the measurement, the state has been projected into the pure state $|m\rangle$.

Similarly, the probability of outcome m occurring when measuring a system in the state ρ is given by

$$p(m) = \mathrm{Tr}(\Pi_m \rho) = \langle m|\rho|m\rangle, \tag{1.26}$$

which reduces to $p(m) = |\langle m|\psi\rangle|^2$ if the state is pure.

Count rates

In practice, we cannot measure probabilities directly; instead, we measure the rate of photons arriving at a detector after the projection into state $|m\rangle$. The count rate $n(m)$ is then proportional to the probability. We can deduce the associated probabilities by choosing a set of measurements $\{\Pi_m\}$ that satisfy the completeness relation $\sum_m \Pi_m^\dagger \Pi_m = \mathbb{1}$ such that the probabilities $p(m)$ must sum to unity. Then

$$p(m) = \frac{n(m)}{\sum_i n(i)}. \tag{1.27}$$

Even this description is an oversimplification of our actual measurements; while the probability of a photon being projected into the state $|m\rangle$ is constant, the actual photon arrival rate is not. To understand this, consider a simple coin toss experiment. While the probability of the coin showing heads is 50%, tossing the coin four times may result in any combination, including four heads or zero heads. It is only when tossing the coin many, many times that the statistics approach 50% heads.

Similarly, a photon in the state $\big(|H\rangle + |V\rangle\big)/\sqrt{2}$ may be statistically 50% likely to project into the state $|H\rangle$, but if we examine the outcome of only four photons, sometimes we will have all four project into the state $|H\rangle$ and sometimes none of them will. It is only after many, many photons that the statistics approach 50%.

To describe the incidence of independent, random events such as photon arrivals, we can use a Poisson distribution [102]. The probability of obtaining k events in a particular interval is

$$P = e^{-\lambda} \frac{\lambda^k}{k!}, \tag{1.28}$$

where λ is the average number of events in the interval and k is a non-negative integer. A key characteristic of this distribution is that the variance of the distribution is equal to the mean. Thus the standard deviation of a Poisson distribution is $\sqrt{\lambda}$.

In order to estimate uncertainties on our measurements, we assume our count rates $n(m)$ follow a Poisson distribution with mean $n(m)$. Then the uncertainty on the measurement is $\sqrt{n(m)}$.

1.2.3 Partial Trace

Sometimes if we have a multi-particle state, we are interested in determining the state of only one particle. To accomplish this, we can perform a partial trace. For example, given a two-photon state $\rho_{\mathrm{AB}} \in \mathcal{H}_{\mathrm{A}}^{d_{\mathrm{A}}} \otimes \mathcal{H}_{\mathrm{B}}^{d_{\mathrm{B}}}$, we are interested in only the state of photon A. Thus we trace over photon B

$$\begin{aligned} \rho_{\mathrm{A}} &= \mathrm{Tr}_{\mathrm{B}}(\rho_{\mathrm{AB}}) \\ &= \sum_{i=0}^{d_{\mathrm{B}}} \langle i|_{\mathrm{B}} \rho_{\mathrm{AB}} |i\rangle_{\mathrm{B}}. \end{aligned} \tag{1.29}$$

Physically, tracing over a photon involves detection without a projective measurement. In the two-photon state above, assuming photon B is encoded in the polarisation degree of freedom, this would entail sending photon B directly to a detector, without encountering a polariser of any kind first. Thus (assuming perfect detection efficiency) photon B will always be detected, regardless of its polarisation, leaving photon A in its original state.

1.2.4 Measuring OAM

As orbital angular momentum is characterised by a rotating phase distribution, we can distinguish between different OAM states based on the phase of the light. There are two main methods that take advantage of this fact to measure OAM. The first method manipulates the phase of the light to spatially separate different OAM values. The second method manipulates the phase of the light to produce a flat phase, which can then be coupled into a single-mode fibre.

Mode Sorter

When measuring polarisation states, it is common to use a polarising beamsplitter (PBS) to measure an entire basis of states at once. A PBS works by spatially separating the two orthogonal basis states using a polarisation-sensitive reflection, allowing for simultaneous detection of both states. By default a PBS measures

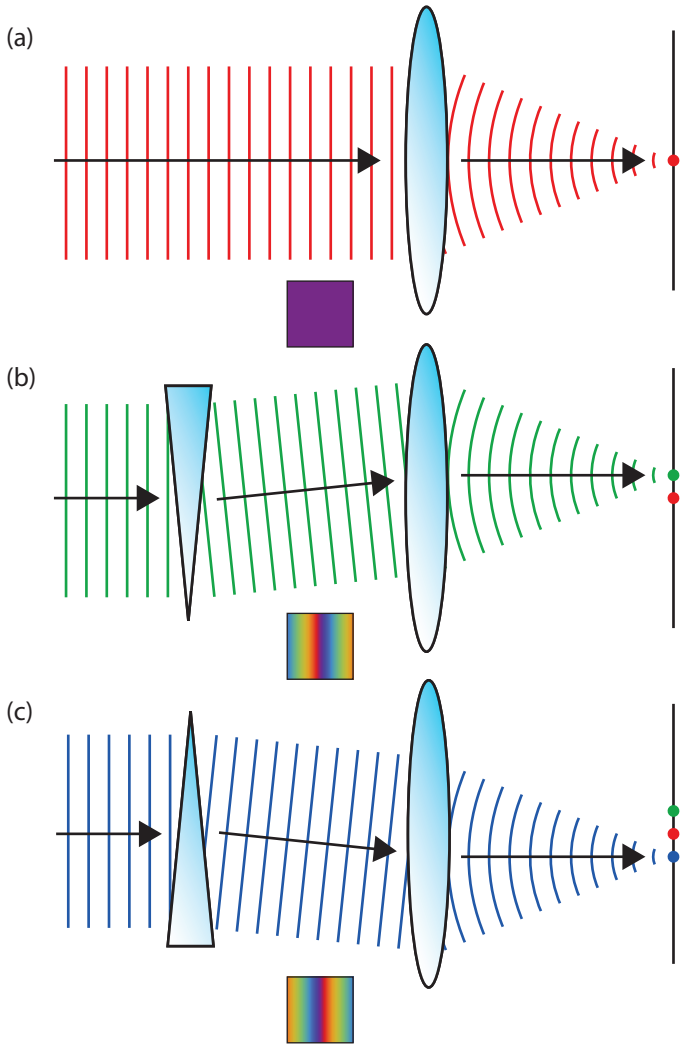

Figure 1.4: **Plane waves.** (a) A plane wave passing at normal incidence through the centre of a lens focuses at a point in line with the centre of the lens. (b) Passing through a glass wedge, the plane wave acquires a linearly varying phase, thus focusing to the left of the centre of the lens. (c) A glass wedge in opposite orientation makes the plane wave focus to the right of the centre of the lens. The insets show the phase profile of the light just before the lens.

in the H/V basis, but with a combination of waveplates we can measure any two orthogonal polarisation states.

The analogue of the PBS for OAM is referred to as a mode sorter. It is capable of spatially separating all OAM values, thus allowing simultaneous measurement of a full high-dimensional basis. It relies on the behaviour of light with a linear, tilted phasefront.

Consider for a moment a flat plane wave, as shown in Fig. 1.4. Passing it through a lens, it focuses at a point in line with the centre of the lens. However, if we pass it through a glass wedge prior to the lens, we obtain a tilted plane wave with a linearly varying phase (see inset). The tilted plane wave will focus at a point to the left of the centre line. Similarly, a glass wedge tilting the plane wave in the opposite direction will result in a focused point to the right of the centre line. In this way, we can distinguish between different linearly tilted phases by spatially separating them with a lens.

Now note that the spiral phasefront of an OAM mode is very similar to a linearly tilted phasefront; the angular position in the spiral version can be mapped to the horizontal position in the linear version, as shown in Fig. 1.5(a). Thus if we could create a physical device to complete this mapping, this would provide a means by which to distinguish between OAM modes.

In fact, we can complete the above operation with just two optical elements [103]. The first optical element, whose phase profile is shown in Fig. 1.5(b), maps concentric circles in the input plane to parallel horizontal lines in the output plane. However, this results in a drastically different optical path length for different parts of the beam; this necessitates the second element, shown in Fig. 1.5(c), which corrects the path length difference.

With this mapping from OAM states to tilted plane waves, we are able to spatially separate different OAM states. This is the high-dimensional equivalent of a polarising beamsplitter, with a few caveats. Firstly, a PBS has two inputs and two outputs, whereas the mode sorter has one input and d outputs; this limits the variety of uses for the mode sorter in comparison to the PBS. Secondly, while a PBS can be used to measure any basis using waveplates to rotate incoming polarisation, the mode sorter can only measure in the OAM basis. It can measure the contribution of several different OAM modes in a single beam; however, it cannot provide phase information.

Additionally, this method of measurement is very involved, requiring careful setup and alignment. If simultaneous measurement of all basis states is not necessary, then projective measurements are more straightforward and easier to implement.

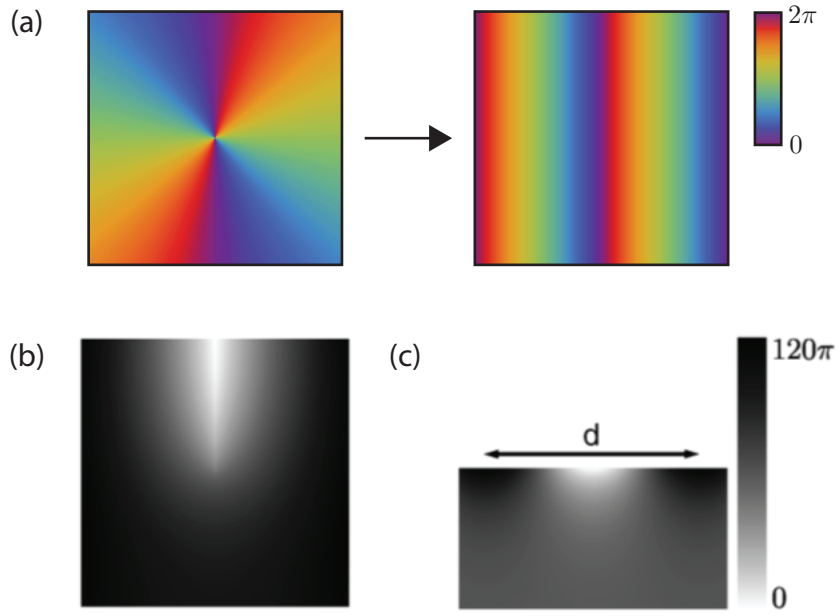

Figure 1.5: **OAM mode sorter.** (a) The desired mapping from an $\ell = 2$ OAM mode to a linearly varying phase that goes through 2π twice. (b) The phase profile of the optical element that achieves the mapping in (a). (c) The phase profile of the optical element that corrects for the optical path length difference resulting from the optical element in (b). Parts (b) and (c) of this figure were taken from Berkhout et al [103].

Projective Measurements

To make a projective measurement of OAM, we first note that the only OAM mode that will couple into a single-mode fibre is the Gaussian mode $\ell = 0$. Thus if we can take the OAM mode that we would like to measure and flatten the phasefront of that mode to the Gaussian mode, we will obtain the probability of obtaining that particular OAM mode.

To flatten an OAM mode, we note that light with OAM $\ell\hbar$ has an exactly opposite phase profile to light with OAM $-\ell\hbar$. In fact, at each point in the phase structure, if the phase of one beam is ϕ, the phase of the other beam will be $2\pi - \phi$. Thus, we can make every phase point zero by simply adding the negative of the phase profile we would like to measure.

For example, light with OAM $\ell = 3$ has a phasefront that goes through 2π three times in a clockwise direction, as shown in Fig. 1.6(a). The opposite handedness of OAM, $\ell = -3$, has exactly opposite phase in that it goes through 2π three times in an anticlockwise direction [Fig. 1.6(b)]. If the phase of an $\ell = -3$ beam is added to light with OAM $\ell = 3$, the phase of the light will become a flat phasefront – the light then has OAM $\ell = 0$ [Fig. 1.6(c)] as the energy is no longer rotating around the axis of propagation. This light will then couple into a single-mode fibre, while nonzero OAM modes will not.

This method can be used to perform a projective measurement of the OAM of light by adding the negative of the phase of interest to a light beam and noting how much resulting light can couple into a single-mode fibre. For example, any light that successfully couples into a single-mode fibre when the $\ell = -3$ phase is added to it must have originally been in the state $\ell = 3$; any other OAM state would result in nonzero OAM [e.g., $(\ell = 2) + (\ell = -3) = (\ell = -1)$], which cannot be transmitted through a single-mode fibre.

We can also use this method for superpositions of OAM states. For example, if we would like to measure the superposition state $(|1\rangle + |2\rangle)/\sqrt{2}$, we apply the phase of the $(|-1\rangle + |-2\rangle)/\sqrt{2}$ state, which transforms any light in the original state into the Gaussian mode. Thus, we can make any projective measurement in any basis, allowing a complete analysis of an OAM state.

This conversion of phase was first accomplished with spiral phase plates [104] as glass produces a phase shift depending on its thickness; however, this requires physically moving plates in and out of a setup in order to change what OAM value is being measured. For faster switching between measurements, spatial light modulators (SLMs) and digital mirror devices (DMDs) are commonly used.

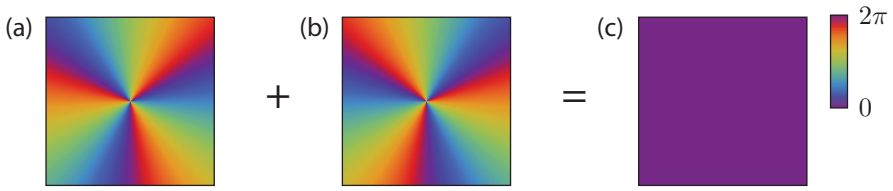

Figure 1.6: **Measurement of OAM.** (a) The phase profile of light with OAM $\ell = 3$. (b) The phase profile of light with OAM $\ell = -3$. (c) Adding these two phases together, we obtain OAM $\ell = 0$, which can be coupled into a single-mode fibre.

Spatial Light Modulators

An SLM is an array of liquid crystals that can be manipulated electronically so that each pixel evokes a different phase shift. The phase of each pixel can be changed at frame rates on the order of 10 to 100 Hz, allowing reasonably fast measurements that cannot be accomplished with glass optics.

As SLMs are not 100% efficient, we must place a diffractive phase grating on the SLM, in addition to the phase we would like to impart on the light, in order to shift the relevant light into the first diffractive order, as shown in Fig. 1.7(a). This prevents any overlap between light unaffected by the SLM and light with the desired phase.

A measurement of an OAM state then occurs as follows: Take the example of an incoming $\ell = 3$ beam. Projecting an $\ell = -3$ OAM phase (added to a diffraction grating) on the SLM, the light in the first diffracted order has OAM $\ell = 0$. A portion of this can then be coupled into a single-mode fibre, resulting in a successful detection as shown in Fig. 1.7(b). However, projecting an $\ell = -1$ OAM phase (added to a diffraction grating) on the SLM, the light in the first diffracted order has OAM $\ell = 2$. This cannot be coupled into a single-mode fibre, resulting in no detection as shown in Fig. 1.7(c). We can then conclude that the incoming light had at least some component of $\ell = 3$ and no component of $\ell = 1$.

1.3 Tomography

As the full state of a quantum system cannot be measured directly, we must make many projective measurements and reconstruct the state using the resultant information. Many of the states we will measure in this thesis are expected to be pure states; however, experimental noise adds mixed components into the state. Most of the states we examine are intended for subsequent use in future communication applications, and whether we like it or not, these applications take into account the

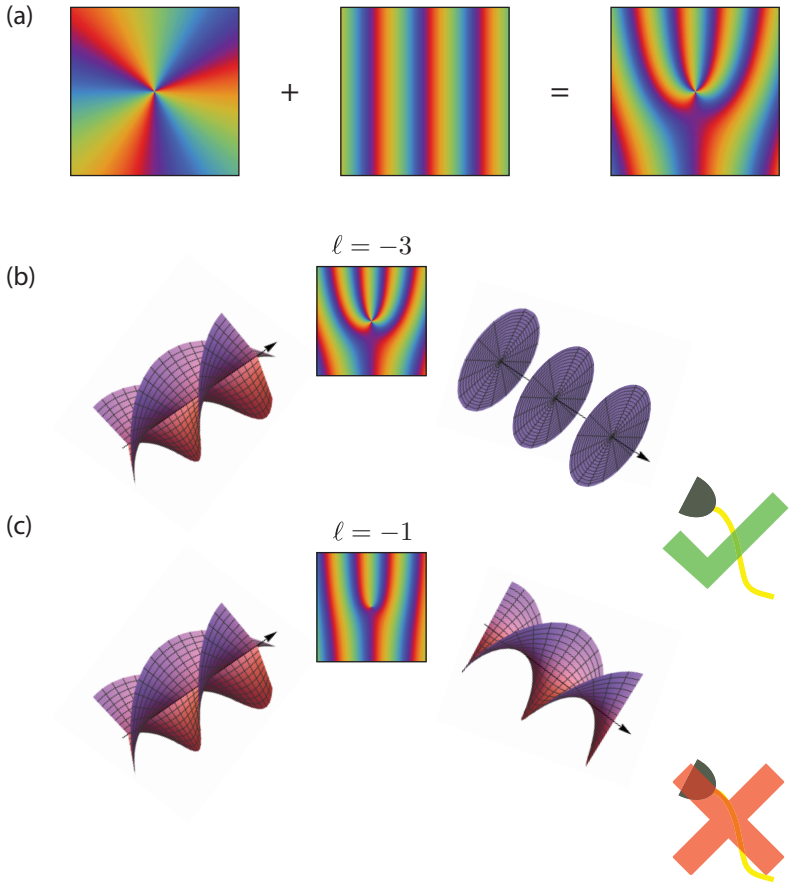

Figure 1.7: **Spatial light modulator.** (a) To separate the desired mode from the unaffected portion of the beam, we apply a phase grating to the OAM mode phase to create a forked grating pattern. (b) When the SLM displays $\ell = -3$ for an incoming $\ell = 3$ mode, we obtain $\ell = 0$, which can be coupled into a single-mode fibre and thus detected. (c) When the SLM displays $\ell = -1$ for an incoming $\ell = 3$ mode, we obtain $\ell = 2$, which cannot be coupled into a single-mode fibre and thus will not be detected.

full mixed state, noise and all. As a result, we choose to reconstruct the density matrix for all states in this thesis, rather than simply the pure state vector.

Take a general density matrix for a polarisation state

$$\rho = \begin{pmatrix} a & b+ic \\ b-ic & 1-a \end{pmatrix}, \tag{1.30}$$

where we have assumed we have a Hermitian density matrix with unit trace and $a, b, c \in \mathbb{R}$. We can make projective measurements on this state to obtain information. For example,

$$\begin{aligned}
\langle H|\rho|H\rangle &= \begin{pmatrix} 1 & 0 \end{pmatrix} \begin{pmatrix} a & b+ic \\ b-ic & 1-a \end{pmatrix} \begin{pmatrix} 1 \\ 0 \end{pmatrix} = a \\
\langle V|\rho|V\rangle &= \begin{pmatrix} 0 & 1 \end{pmatrix} \begin{pmatrix} a & b+ic \\ b-ic & 1-a \end{pmatrix} \begin{pmatrix} 0 \\ 1 \end{pmatrix} = 1-a \\
\langle D|\rho|D\rangle &= \frac{1}{\sqrt{2}} \begin{pmatrix} 1 & 1 \end{pmatrix} \begin{pmatrix} a & b+ic \\ b-ic & 1-a \end{pmatrix} \frac{1}{\sqrt{2}} \begin{pmatrix} 1 \\ 1 \end{pmatrix} = \frac{1+2b}{2} \\
\langle A|\rho|A\rangle &= \frac{1}{\sqrt{2}} \begin{pmatrix} 1 & -1 \end{pmatrix} \begin{pmatrix} a & b+ic \\ b-ic & 1-a \end{pmatrix} \frac{1}{\sqrt{2}} \begin{pmatrix} 1 \\ -1 \end{pmatrix} = \frac{1-2b}{2} \\
\langle R|\rho|R\rangle &= \frac{1}{\sqrt{2}} \begin{pmatrix} 1 & -i \end{pmatrix} \begin{pmatrix} a & b+ic \\ b-ic & 1-a \end{pmatrix} \frac{1}{\sqrt{2}} \begin{pmatrix} 1 \\ i \end{pmatrix} = \frac{1-2c}{2} \\
\langle L|\rho|L\rangle &= \frac{1}{\sqrt{2}} \begin{pmatrix} 1 & i \end{pmatrix} \begin{pmatrix} a & b+ic \\ b-ic & 1-a \end{pmatrix} \frac{1}{\sqrt{2}} \begin{pmatrix} 1 \\ -i \end{pmatrix} = \frac{1+2c}{2}.
\end{aligned}$$

It is tempting to simply invert these equations to obtain

$$a = \langle H|\rho|H\rangle = 1 - \langle V|\rho|V\rangle \tag{1.31}$$

$$b = \frac{2\langle D|\rho|D\rangle - 1}{2} = \frac{1 - 2\langle A|\rho|A\rangle}{2} \tag{1.32}$$

$$c = \frac{1 - 2\langle R|\rho|R\rangle}{2} = \frac{2\langle L|\rho|L\rangle - 1}{2}. \tag{1.33}$$

However, in practice the result of a projective measurement may not be precisely accurate as there is a variance associated with the measurement, and the two different options for calculating a, b, and c may give different results. Inverting the above equations with such measurements can cause the resulting density matrix not to represent a physical state; that is, the matrix will not necessarily have positive eigenvalues.

Taking the example of the density matrix for the diagonal polarisation state

$$\rho = \frac{1}{2} \begin{pmatrix} 1 & 1 \\ 1 & 1 \end{pmatrix}, \tag{1.34}$$

we find in theory that $\langle H|\rho|H\rangle = 1/2$, $\langle D|\rho|D\rangle = 1$, and $\langle R|\rho|R\rangle = 1/2$. These results by definition satisfy Eqs. (1.31-1.33) and return the original density matrix

ρ. However, if the measurements have minor fluctuations in them, we may obtain instead $\langle H|\rho|H\rangle = 0.5$, $\langle D|\rho|D\rangle = 1$, and $\langle R|\rho|R\rangle = 0.45$. Then Eqs. (1.31-1.33) return the calculated density matrix

$$\rho = \begin{pmatrix} 0.5 & 0.5 + 0.05i \\ 0.5 - 0.05i & 0.5 \end{pmatrix}, \tag{1.35}$$

whose eigenvalues are 1.002 and -0.002. This does not represent a physical state, and thus we know our estimate of the density matrix is incorrect.

To find a density matrix that does satisfy these conditions, we must reconstruct it in a different manner. Our task is to find the density matrix that is most likely to have produced the measurements.

1.3.1 Maximum Likelihood Estimation

The most common method, and the one we use in this thesis, for the reconstruction of a density matrix in quantum mechanics is maximum likelihood estimation [105]. We will describe the method in terms of a qubit state, though it applies equally to any state, from a single-qubit state to a multi-qudit state.

First we must define the density matrix in such a way that it must have unit trace and be both Hermitian and positive semidefinite: a physical matrix. A matrix of the form

$$\rho = \frac{T^\dagger T}{\mathrm{Tr}(T^\dagger T)} \tag{1.36}$$

satisfies these conditions for any matrix T. Our matrix T must have sufficient degrees of freedom to accurately specify ρ. As ρ is Hermitian, there are only d^2 degrees of freedom for a d-dimensional state. (In fact, there are d^2-1 degrees of freedom due to the unit trace, but as we can only measure photon counts rather than probabilities, we require d^2 degrees of freedom to normalise the counts to probailities.)

For simplicity, we choose our matrix T to be a lower triangular matrix with real diagonal entries. So for a qubit state ($d = 2$), we start with a matrix

$$T(\vec{t}) = \begin{pmatrix} t_1 & 0 \\ t_2 + it_3 & t_4 \end{pmatrix}, \tag{1.37}$$

where we have chosen elements $\vec{t} = \{t_1, t_2, t_3, t_4\}$.

We now consider a set of projective measurements $\{|\psi_i\rangle\}$ with outcomes $\{n_i\}$. The density matrix that produced these outcomes must come as close as possible to satisfying

$$n_i = N\langle\psi_i|\rho(\vec{t})|\psi_i\rangle \tag{1.38}$$

for all i, where N is a constant that converts probabilities into counts. Assuming that the noise on the measurements follows a Gaussian distribution, the probability of a matrix $\rho(\vec{t})$ producing the set of measurements $\{n_i\}$ is

$$P\big(\{n_i\}\big) = \frac{1}{C}\prod_i \exp\left[-\frac{\big(N\langle\psi_i|\rho(\vec{t})|\psi_i\rangle - n_i\big)^2}{2N\langle\psi_i|\rho(\vec{t})|\psi_i\rangle}\right]. \tag{1.39}$$

Maximising the above function is equivalent to minimising the likelihood function

$$\mathcal{L}(\vec{t}) = \sum_i \frac{\big(N\langle\psi_i|\rho(\vec{t})|\psi_i\rangle - n_i\big)^2}{2N\langle\psi_i|\rho(\vec{t})|\psi_i\rangle}. \tag{1.40}$$

Thus the density matrix $\rho(\vec{t})$ that minimises this expression is the most likely state to have produced the observed outcomes.

We must use a tomographically complete set of measurements, i.e., the measurements must span the state space we are measuring. A commonly chosen minimally complete set consists of measurements from different bases with minimal overlap; these bases are called mutually unbiased, and there are $d+1$ in a d-dimensional space. For a qubit state encoded in polarisation, an example of a tomographically complete measurement set is $\{|H\rangle, |V\rangle, |D\rangle, |R\rangle\}$, where we have included at least one measurement in each of the H/V, D/A, and R/L mutually unbiased bases, plus one additional measurement in order to normalise the counts into probabilities.

Note that in this method, unlike with direct equation inversion, we are able to use more than d^2 measurements to reconstruct the state. This provides us with more certainty of our resultant state as it minimises the effect of noise in the measurements. Thus it is common to use all states from all mutually unbiased bases, e.g., $\{|H\rangle, |V\rangle, |D\rangle, |A\rangle, |R\rangle, |L\rangle\}$.

1.3.2 Example Data

To illustrate the method, first consider the density matrix in Eq. (1.35) that we obtained using Eqs. (1.31 – 1.33). Recall the probabilities used were $\langle H|\rho|H\rangle = 0.5$, $\langle D|\rho|D\rangle = 1$, and $\langle R|\rho|R\rangle = 0.45$. Reconstructing the density matrix using the maximum likelihood method, we obtain

$$\rho_L = \begin{pmatrix} 0.5 & 0.497 + 0.051i \\ 0.497 - 0.051i & 0.5 \end{pmatrix}. \tag{1.41}$$

This matrix is only slightly different from our previous estimate in Eq. (1.35); however, it now has non-negative eigenvalues and can represent the actual state.

Second, we will use data from Chapter 4 of this thesis, which includes tomographically reconstructing qubit states in the orbital angular momentum basis. We

will examine the measurements on a photon expected to be in the OAM state $|-1\rangle$. The background-subtracted count rates are shown in Table 1.1, where the uncertainties represent the standard deviation of a Poisson distribution centred at the value of the corresponding count rate.

We convert these to probabilities by dividing each count rate by the sum of counts in its basis. For example, the state $|-1\rangle$ has a count rate of 90 Hz, and its orthogonal pair $|1\rangle$ has a count rate of 16 Hz; thus we conclude that the photon has an 85% chance of projecting into the state $|-1\rangle$ and a 15% chance of projecting into the state $|1\rangle$. The probabilities are also shown in Table 1.1.

State	Count rate (Hz)	Probability
$\|-1\rangle$	90 ± 9	0.85 ± 0.08
$\|1\rangle$	16 ± 4	0.15 ± 0.04
$\big(\|-1\rangle + \|1\rangle\big)/\sqrt{2}$	49 ± 7	0.62 ± 0.09
$\big(\|-1\rangle - \|1\rangle\big)/\sqrt{2}$	30 ± 5	0.38 ± 0.06
$\big(\|-1\rangle + i\|1\rangle\big)/\sqrt{2}$	43 ± 7	0.64 ± 0.10
$\big(\|-1\rangle - i\|1\rangle\big)/\sqrt{2}$	24 ± 5	0.36 ± 0.07

Table 1.1: **Example tomography data.** The background-subtracted count rates and resultant probabilities for six measurements on a photon expected to be in the OAM state $|-1\rangle$.

The minimisation procedure can be done analytically; however, we insert the measurements and outcomes into Eq. (1.40) and use the Mathematica function `FindMinimum` to find the most likely density matrix

$$\rho_L = \begin{pmatrix} 0.85 & 0.12 - 0.14i \\ 0.12 + 0.14i & 0.15 \end{pmatrix}. \tag{1.42}$$

1.3.3 Fidelity

To determine how close a state ρ is to the expected state σ, we can calculate the fidelity

$$F = \left[\mathrm{Tr}\left(\sqrt{\sqrt{\rho}\sigma\sqrt{\rho}}\right)\right]^2. \tag{1.43}$$

The fidelity can range between zero and unity. For two identical states, the fidelity is unity; for two completely dissimilar states, the fidelity is zero.

For example, the state reconstructed in the previous section is expected to be

$|-1\rangle$. We can determine the fidelity between $\rho = \rho_L$ and $\sigma = |-1\rangle\langle -1|$:

$$\begin{aligned} F &= \left[\mathrm{Tr}\left(\sqrt{\sqrt{\rho_L}|-1\rangle\langle -1|\sqrt{\rho_L}}\right)\right]^2 \\ &= 0.85. \end{aligned} \tag{1.44}$$

This indicates that our reconstructed state is very similar to $|-1\rangle$, though perhaps not quite as accurate as we would like.

To obtain the standard deviation of the fidelity, we assume each count rate represents the mean value of a Poisson distribution. We then simulate many different sets of count rates based on these distributions, and for each set we reconstruct the associated density matrix. We calculate the fidelity of each of these density matrices, and we take the standard deviation of these to be the standard deviation on our real fidelity. In this case, again using the data from Table 1.1, we obtain a standard deviation of 0.03, making our estimate of the fidelity fairly accurate at 0.85 ± 0.03.

Fidelity with a Pure State

It is also worth noting that when one of the states is pure, the fidelity reduces to a simpler expression. Consider that the density matrix of a pure state is simply the outer product of its state vector $\rho = |\psi\rangle\langle\psi|$. It is therefore the case that $\rho^2 = |\psi\rangle\langle\psi||\psi\rangle\langle\psi| = |\psi\rangle\langle\psi| = \rho$. It follows that $\sqrt{\rho} = \rho = |\psi\rangle\langle\psi|$, meaning that the expression for fidelity can be simplified:

$$\begin{aligned} F &= \left[\mathrm{Tr}\left(\sqrt{\sqrt{\rho}\sigma\sqrt{\rho}}\right)\right]^2 \\ &= \left[\mathrm{Tr}\left(\sqrt{|\psi\rangle\langle\psi|\sigma|\psi\rangle\langle\psi|}\right)\right]^2 \\ &= \left[\sqrt{\langle\psi|\sigma|\psi\rangle}\mathrm{Tr}\left(\sqrt{|\psi\rangle\langle\psi|}\right)\right]^2 \\ &= \langle\psi|\sigma|\psi\rangle\mathrm{Tr}\big(\rho\big)^2 \\ &= \langle\psi|\sigma|\psi\rangle \\ &= \mathrm{Tr}(\rho\sigma). \end{aligned} \tag{1.45}$$

Let us examine the fidelity of the states

$$\rho = \begin{pmatrix} a & b+ic \\ b-ic & d \end{pmatrix}; \qquad \sigma = \begin{pmatrix} \alpha & \beta+i\gamma \\ \beta-i\gamma & \delta \end{pmatrix}, \tag{1.46}$$

where one of them, e.g., ρ, is a pure state. The fidelity is then

$$F = a\alpha + 2b\beta + 2c\gamma + d\delta. \tag{1.47}$$

It is clear that if the off-diagonal element of one matrix is zero, i.e., $b = c = 0$, then the fidelity reduces to a function of only the diagonal elements $F = a\alpha + d\delta$. It is straightforward to show a similar result in higher-dimensional states as well: if one of the off-diagonal elements of a pure state density matrix is zero, then the corresponding element in the other matrix, whether or not it is itself a pure state, will not contribute to the fidelity calculation. This becomes useful in Chapter 3 when we would like to determine the fidelity of a high-dimensional state without measuring every element due to time constraints.

1.4 Entanglement

Entanglement is a uniquely quantum phenomenon first addressed by Einstein, Podolsky, and Rosen in their seminal paper in 1935 [1] and further explored by Schrodinger [106] and Bell [2]. It is certainly unlike any correlation seen in classical physics and is a very powerful resource for current and future applications of quantum technology.

Two entangled particles share correlations no matter how far apart the particles are; however, this is not specific to quantum entanglement. A common (and inaccurate) analogy for entanglement involves a pair of coins adding to 15p – one is a 10p coin while the other is a 5p coin. One of the coins at random is placed in envelope A and the other coin is placed in envelope B, and the two envelopes are given to two different people and sent to opposite sides of the world. If person A opens their envelope and finds a 5p coin, they know that person B has a 10p coin, and vice versa. The correlation between the contents of the two envelopes holds regardless of their location.

The issue with the above analogy is in the determinism of the envelopes' contents. Prior to sending the envelopes to different locations, their contents are already decided; it's not possible to place the 5p coin in envelope A and then open it later to find the 10p coin. Conversely, the state of entangled particles is not deterministic; until a measurement is made, the state of the particle is a superposition of all possible states. Rather than one measurement revealing what the other particle's state was all along, in the quantum case one measurement sets the result of the second measurement.

It is this superposition element of entanglement that sets it off from classical correlations. To understand this more clearly in terms of quantum particles, let us consider the polarisation of photons. If we prepare a classically correlated state of two photons, each horizontally polarised, obviously a measurement in the H/V basis will result in 100% probability of obtaining the state $|H\rangle$ in both photons and zero probability of obtaining $|H\rangle$ in one photon and $|V\rangle$ in the other. However, a measurement in another basis, e.g., the D/A basis, is not so straightforward.

Projecting both photons into diagonal polarisation, we obtain

$$\begin{aligned}\left|\langle D|_{\mathrm{A}}\langle D|_{\mathrm{B}}|\psi\rangle_{\mathrm{AB}}\right|^2 &= \left|\langle D|_{\mathrm{A}}\langle D|_{\mathrm{B}}|H\rangle_{\mathrm{A}}|H\rangle_{\mathrm{B}}\right|^2 \\ &= \left|\frac{1}{\sqrt{2}}\big(\langle H|_{\mathrm{A}}+\langle V|_{\mathrm{A}}\big)\frac{1}{\sqrt{2}}\big(\langle H|_{\mathrm{B}}+\langle V|_{\mathrm{B}}\big)|H\rangle_{\mathrm{A}}|H\rangle_{\mathrm{B}}\right|^2 \\ &= \frac{1}{4}. \end{aligned} \tag{1.48}$$

Similarly, projecting photon A into diagonal polarisation and photon B into anti-diagonal polarisation, we obtain

$$\begin{aligned}\left|\langle D|_{\mathrm{A}}\langle A|_{\mathrm{B}}|\psi\rangle_{\mathrm{AB}}\right|^2 &= \left|\langle D|_{\mathrm{A}}\langle A|_{\mathrm{B}}|H\rangle_{\mathrm{A}}|H\rangle_{\mathrm{B}}\right|^2 \\ &= \left|\frac{1}{\sqrt{2}}\big(\langle H|_{\mathrm{A}}+\langle V|_{\mathrm{A}}\big)\frac{1}{\sqrt{2}}\big(\langle H|_{\mathrm{B}}-\langle V|_{\mathrm{B}}\big)|H\rangle_{\mathrm{A}}|H\rangle_{\mathrm{B}}\right|^2 \\ &= \frac{1}{4}. \end{aligned} \tag{1.49}$$

It is straightforward to calculate the probability to project into $|A\rangle_{\mathrm{A}}|A\rangle_{\mathrm{B}}$ and $|A\rangle_{\mathrm{A}}|D\rangle_{\mathrm{B}}$, which are also both 1/4. Thus there is an equal probability of projecting both photons into the same polarisation state as into opposite polarisation states.

We can instead prepare an entangled state where either both photons are horizontally polarised or both are vertically polarised, $\frac{1}{\sqrt{2}}\big(|H\rangle_{\mathrm{A}}|H\rangle_{\mathrm{B}}+|V\rangle_{\mathrm{A}}|V\rangle_{\mathrm{B}}\big)$. Obviously a measurement in the H/V basis will result in 100% probability of obtaining both photons in the same state (50% probability of horizontal polarisation and 50% probability of vertical polarisation) and zero probability of obtaining the photons in opposite polarisation states. However, projecting both photons into diagonal polarisation, we obtain

$$\begin{aligned}\left|\langle D|_{\mathrm{A}}\langle D|_{\mathrm{B}}|\psi\rangle_{\mathrm{AB}}\right|^2 &= \left|\langle D|_{\mathrm{A}}\langle D|_{\mathrm{B}}\frac{1}{\sqrt{2}}\big(|H\rangle_{\mathrm{A}}|H\rangle_{\mathrm{B}}+|V\rangle_{\mathrm{A}}|V\rangle_{\mathrm{B}}\big)\right|^2 \\ &= \left|\frac{1}{2\sqrt{2}}\big(\langle H|_{\mathrm{A}}+\langle V|_{\mathrm{A}}\big)\big(\langle H|_{\mathrm{B}}+\langle V|_{\mathrm{B}}\big)\big(|H\rangle_{\mathrm{A}}|H\rangle_{\mathrm{B}}+|V\rangle_{\mathrm{A}}|V\rangle_{\mathrm{B}}\big)\right|^2 \\ &= \frac{1}{2\sqrt{2}}(1+1) \\ &= \frac{1}{2}. \end{aligned} \tag{1.50}$$

Conversely, projecting photon A into diagonal polarisation and photon B into anti-diagonal polarisation, we obtain

$$\begin{aligned}\left|\langle D|_{\mathrm{A}}\langle A|_{\mathrm{B}}|\psi\rangle_{\mathrm{AB}}\right|^2 &= \left|\langle D|_{\mathrm{A}}\langle A|_{\mathrm{B}}\frac{1}{\sqrt{2}}\big(|H\rangle_{\mathrm{A}}|H\rangle_{\mathrm{B}}+|V\rangle_{\mathrm{A}}|V\rangle_{\mathrm{B}}\big)\right|^2 \\ &= \left|\frac{1}{2\sqrt{2}}\big(\langle H|_{\mathrm{A}}+\langle V|_{\mathrm{A}}\big)\big(\langle H|_{\mathrm{B}}-\langle V|_{\mathrm{B}}\big)\big(|H\rangle_{\mathrm{A}}|H\rangle_{\mathrm{B}}+|V\rangle_{\mathrm{A}}|V\rangle_{\mathrm{B}}\big)\right|^2 \\ &= \frac{1}{2\sqrt{2}}(1-1) \\ &= 0. \end{aligned} \tag{1.51}$$

It is straightforward to calculate the probability to project into $|A\rangle_{\mathrm{A}}|A\rangle_{\mathrm{B}}$ and $|A\rangle_{\mathrm{A}}|D\rangle_{\mathrm{B}}$, which are 1/2 and zero, respectively. Thus with this entangled state, the photons can only project into same-polarisation states and not into opposite-polarisation states in the D/A basis. This effect also occurs in any other polarisation basis; this correlation in a basis other than the one we intended to prepare (H/V) arises from the superposition inherent in entanglement.

In this brief example, we are able to see the defining feature of quantum entanglement: the existence of correlations in all bases. This is only possible in a quantum state in which the outcome is not set until measurement, and not in a classical state in which the outcome is set when the state is prepared. With this somewhat intuitive understanding of entanglement, we can now discuss the precise mathematical definition of entanglement.

1.4.1 Mathematical Description of Entanglement

The rigorous definition of entanglement involves the separability of a state, or more precisely the lack thereof. If the combined state ρ of two particles A and B can be written as the weighted sum of products of two single-particle states

$$\rho = \sum_i p_i \rho_i^{\mathrm{A}} \otimes \rho_i^{\mathrm{B}} \tag{1.52}$$

then the state is separable. This is because the above state can be produced without any interaction between the two particles; instead, two parties A and B can agree to generate the single-particle states ρ_i^{A} and ρ_i^{B}, respectively, with probability p_i as determined by, for example, a random-number generator. The states of the two particles are then correlated, but they are not entangled as the states can be produced independently of one another. Thus, if the combined state of two particles cannot be written in this way, then the state is entangled [107].

The above criterion can be simplified for the case of pure states. In this case, the combined pure state $|\psi\rangle$ is separable if it can be written as the product of two pure states

$$|\psi\rangle = |\psi_A\rangle \otimes |\psi_B\rangle. \tag{1.53}$$

Otherwise, it is entangled.

1.4.2 Bell States

Of particular interest is a class of entangled states called Bell states, so named due to their use in Bell's theorem [2]. The Bell states are four maximally entangled

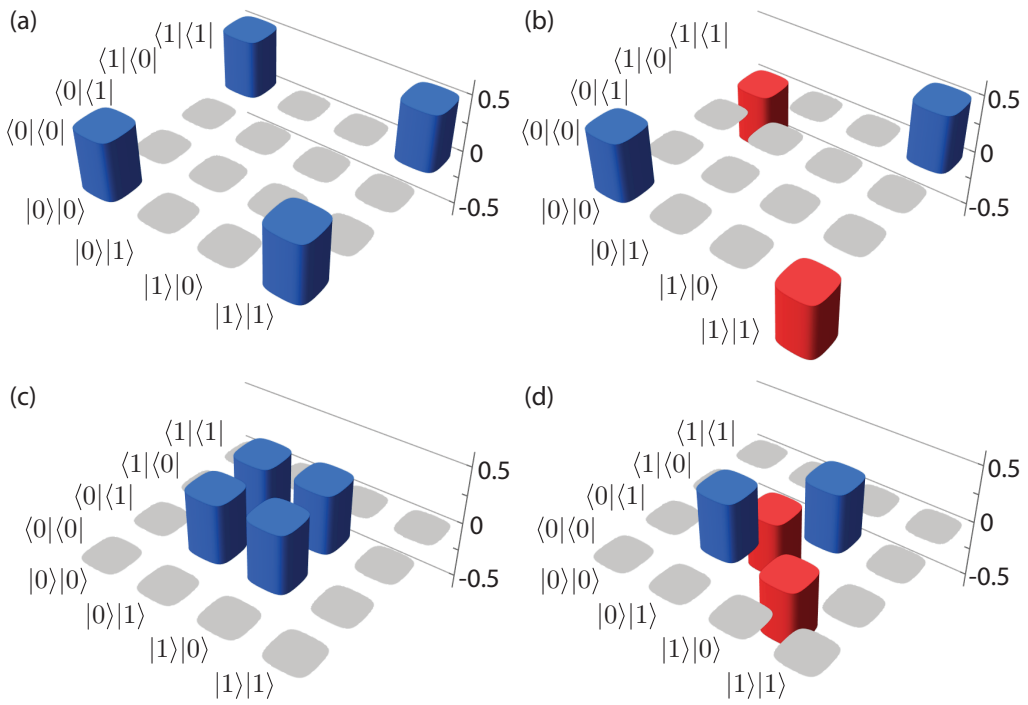

Figure 1.8: **Density matrices of Bell states.** The real parts of the four Bell states (a) $|\Phi^+\rangle$, (b) $|\Phi^-\rangle$, (c) $|\Psi^+\rangle$, and (d) $|\Psi^-\rangle$. Blue bars indicate positive values; red bars indicate negative values; and grey indicates the element is zero. The imaginary parts are not shown as they are all zero.

two-qubit states as follows:

$$|\Phi^+\rangle = \frac{1}{\sqrt{2}}\left(|0\rangle_A|0\rangle_B + |1\rangle_A|1\rangle_B\right) \tag{1.54}$$

$$|\Phi^-\rangle = \frac{1}{\sqrt{2}}\left(|0\rangle_A|0\rangle_B - |1\rangle_A|1\rangle_B\right) \tag{1.55}$$

$$|\Psi^+\rangle = \frac{1}{\sqrt{2}}\left(|0\rangle_A|1\rangle_B + |1\rangle_A|0\rangle_B\right) \tag{1.56}$$

$$|\Psi^-\rangle = \frac{1}{\sqrt{2}}\left(|0\rangle_A|1\rangle_B - |1\rangle_A|0\rangle_B\right). \tag{1.57}$$

The $|\Phi^\pm\rangle$ states are correlated in that both photons will be in the same basis state, while the $|\Psi^\pm\rangle$ states are anti-correlated in that the photons will be in opposite basis states. Taken together, these four states form a complete basis for all two-photon states. In Fig. 1.8, we show the density matrices of the four Bell states.

Symmetry of Bell States

The symmetry of the Bell states, i.e., the behaviour of the Bell states when the particles are exchanged, plays a key role in this thesis. This is because a measurement that we will use in Chapters 2–5 relies on the distinction between symmetric and anti-symmetric Bell states. Thus a brief but important explanation of this concept is necessary.

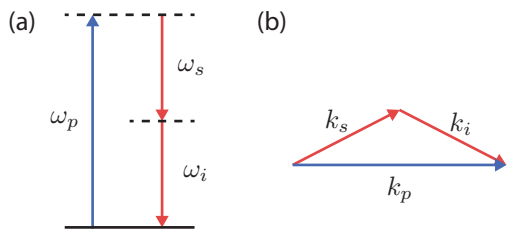

Figure 1.9: **Conservation rules.** (a) Due to conservation of energy, the frequencies of the signal and idler photons must sum to the frequency of the pump photon. (b) Due to conservation of momentum, the momenta of the signal and idler photons must sum to the momentum of the pump photon.

The first three Bell states are called symmetric Bell states as the state remains the same under exchange of particles. For example, exchanging the particles in $|\Psi^+\rangle$ we obtain

$$\begin{aligned} |\Psi^+\rangle &= \frac{1}{\sqrt{2}}\big(|0\rangle_\mathrm{A}|1\rangle_\mathrm{B} + |1\rangle_\mathrm{A}|0\rangle_\mathrm{B}\big) \\ &\to \frac{1}{\sqrt{2}}\big(|0\rangle_\mathrm{B}|1\rangle_\mathrm{A} + |1\rangle_\mathrm{B}|0\rangle_\mathrm{A}\big) \\ &= \frac{1}{\sqrt{2}}\big(|0\rangle_\mathrm{A}|1\rangle_\mathrm{B} + |1\rangle_\mathrm{A}|0\rangle_\mathrm{B}\big) \\ &= |\Psi^+\rangle \end{aligned} \tag{1.58}$$

and the state remains unchanged. The $|\Phi^\pm\rangle$ states behave the same way.

Conversely, the fourth state $|\Psi^-\rangle$ is called the anti-symmetric Bell state as exchanging the particles produces

$$\begin{aligned} |\Psi^-\rangle_\mathrm{AB} &= \frac{1}{\sqrt{2}}\big(|0\rangle_\mathrm{A}|1\rangle_\mathrm{B} - |1\rangle_\mathrm{A}|0\rangle_\mathrm{B}\big) \\ &\to \frac{1}{\sqrt{2}}\big(|0\rangle_\mathrm{B}|1\rangle_\mathrm{A} - |1\rangle_\mathrm{B}|0\rangle_\mathrm{A}\big) \\ &= |\Psi^-\rangle_\mathrm{BA} \\ &= -|\Psi^-\rangle_\mathrm{AB}, \end{aligned} \tag{1.59}$$

which is the negative of the original state.

1.4.3 Producing Entanglement

In optics, entanglement is often produced experimentally using spontaneous parametric downconversion (SPDC). This is a χ^2 nonlinear process in which an incident photon with energy $\hbar\omega$ excites an atom in a nonlinear crystal; the atom then decays, emitting two photons (referred to as the signal and the idler), as shown in

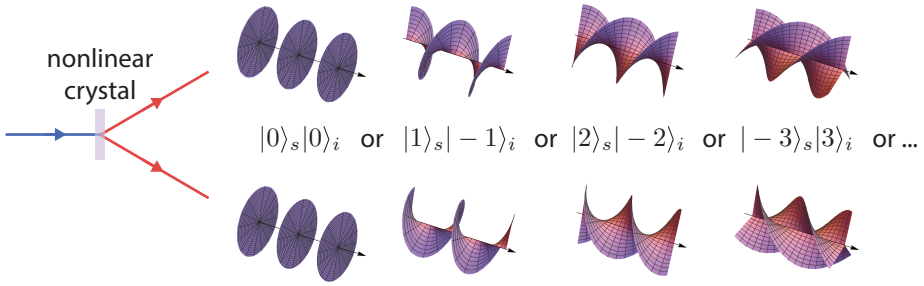

Figure 1.10: **OAM entanglement.** Light at a short wavelength (e.g., 405 nm) in the Gaussian mode strikes a nonlinear crystal and undergoes SPDC to two photons at twice the wavelength (e.g., 810 nm). Due to conservation of angular momentum, the photons are in a superposition of all possible OAM states that sum to zero.

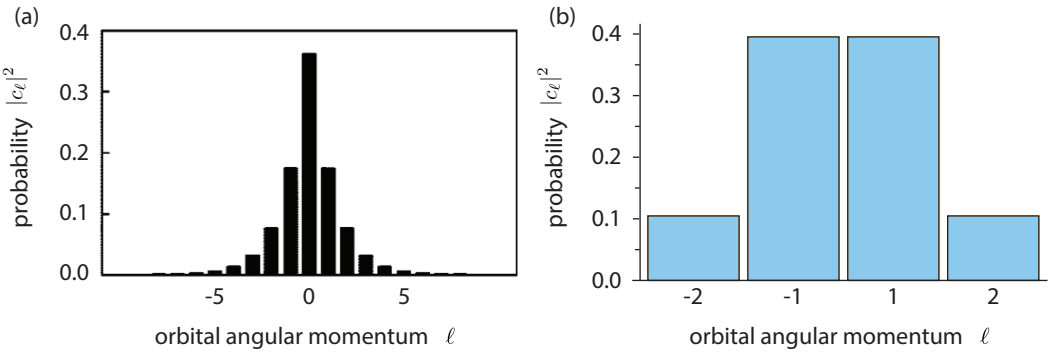

Figure 1.11: **OAM distribution.** (a) A typical OAM distribution, taken from Ref. [108]. (b) The OAM distribution estimated in Chapter 3.

Fig. 1.9. The energy conservation results in the wavelengths of the pump, signal, and idler photons satisfying the equation $1/\lambda_p = 1/\lambda_s + 1/\lambda_i$. The exact relationship between the three is determined by the phase-matching conditions; it is common to use degenerate phase-matching to obtain $\lambda_s = \lambda_i$.

Similarly, conservation of momentum results in entanglement in the position and linear momentum, as well as in the orbital angular momentum degree of freedom [31, 86]. The pump beam is usually a Gaussian mode, i.e., $\ell = 0$, meaning that the signal and idler must have equal and opposite OAM such that $\ell_s = -\ell_i$, as shown in Fig. 1.10. In fact, the photons are in a superposition of all OAMs that satisfy this condition, resulting in entanglement of the form

$$|\Psi\rangle = \sum_{\ell} c_\ell |\ell\rangle_s |-\ell\rangle_i, \tag{1.60}$$

where $|c_\ell|^2$ is the probability of finding the signal photon with OAM $\ell\hbar$ and the idler photon with OAM $-\ell\hbar$.

While in theory it is possible to have entanglement in infinitely many OAM values, in practice there is a limit to the number of entangled modes available. The probability $|c_\ell|^2$ typically is a non-uniform function of ℓ, the shape of which we refer to as the OAM distribution. The OAM distribution is affected by a wide variety of parameters, including beam waist of the pump and thickness of the nonlinear crystal [93, 108]. A typical OAM distribution is shown in Fig. 1.11(a), while an estimated OAM distribution for the system used in Chapters 3–5 is shown in Fig. 1.11(b). It is common to have $c_\ell \approx c_{-\ell}$; we assume this condition throughout this thesis as it makes calculations more straightforward.

1.4.4 Remote State Preparation

In Chapter 4 of this thesis, we must prepare a single-photon state for teleportation, which will be discussed later. It is possible to use a weak coherent state for this purpose, i.e., attenuate the laser to an intensity of very few photons per pulse; however, to ensure the presence of one (and only one) photon in the desired state, we choose instead to use remote state preparation [109].

Remote state preparation relies on entanglement as its key ingredient. We begin with a pair of photons entangled in the state of Eq. (1.60). As we know the form of the entanglement between the signal and idler photons, we are able to predict what a measurement on the idler photon will do to the signal photon.

We project the idler photon into the state $|\psi\rangle = \sum_\ell a_\ell |\ell\rangle$ using an SLM and

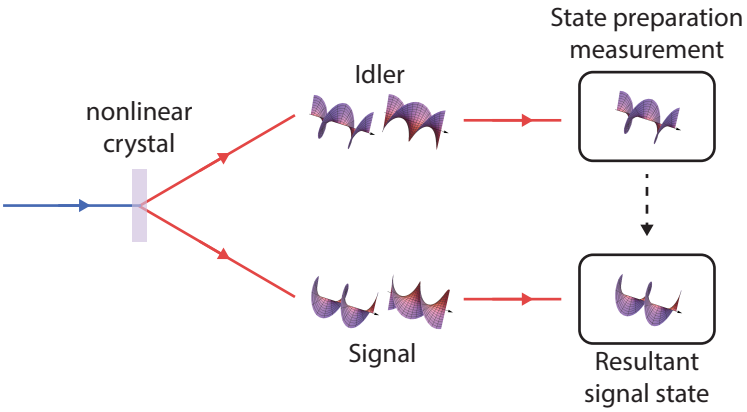

Figure 1.12: **Remote state preparation.** By performing a measurement of, e.g., $\ell = 1$ in one photon, we project its entangled pair into $\ell = -1$.

single-mode fibre, producing

$$\begin{aligned}\langle\psi|\Psi\rangle &= \sum_{\ell} a_\ell^* \langle \ell|_i \sum_k c_k |k\rangle_s |-k\rangle_i \\ &= \sum_{\ell} a_\ell^* c_{-\ell} |-\ell\rangle_s. \end{aligned} \tag{1.61}$$

Under the assumption of a uniform OAM distribution (i.e., $|c_\ell|^2 = 1/d$ for all ℓ in the d-dimensional state space), we obtain the state $\sum_\ell a_\ell^* |-\ell\rangle_s$ in the signal photon. This process is shown in Fig. 1.12.

In practice, the OAM distribution is not likely to be uniform, meaning that the state produced in the signal photon may not be exactly what is desired. This can be remedied by adjusting the OAM distribution at detection using entanglement concentration [110]. For example, imagine we would like a single photon in the state $\big(|1\rangle - i|2\rangle\big)/\sqrt{2}$. If we project the idler photon into the state $\big(|-1\rangle + i|-2\rangle\big)/\sqrt{2}$, we obtain in the signal photon the state $\big(c_1|1\rangle - ic_2|2\rangle\big)/\sqrt{2}$. If the OAM distribution is not uniform, i.e., $c_1 \neq c_2$, then this is not quite the state we are interested in. To solve this, we can measure c_1 and c_2 in advance and project the idler photon into an adjusted state $\big(|-1\rangle/c_1^* + i|-2\rangle/c_2^*\big)/\sqrt{2}$, which will successfully produce the state we desire.

1.4.5 Concurrence

When we reconstruct entangled states, we are often interested in their degree of entanglement. To determine this, we can calculate the concurrence of the state, as long as the state consists of two qubits. The concurrence of a density matrix ρ is calculated by first obtaining a matrix

$$R = \sqrt{\sqrt{\rho}\,\widetilde{\rho}\,\sqrt{\rho}}\,, \tag{1.62}$$

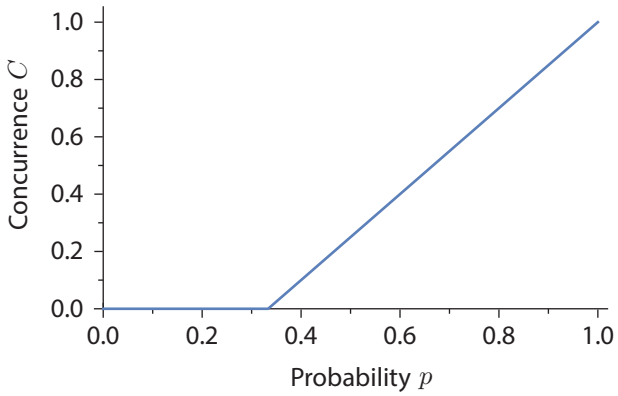

Figure 1.13: **Concurrence vs. probability.** The concurrence of a Werner state based on the probability of observing the maximally entangled state $|\Psi^-\rangle$.

where $\widetilde{\rho} = (\sigma_y \otimes \sigma_y)\rho^*(\sigma_y \otimes \sigma_y)$. Here σ_y represents the Pauli spin matrix and ρ^* represents the complex conjugate (not the conjugate transpose) of ρ. The eigenvalues of the matrix R are denoted $\lambda_1, \lambda_2, \lambda_3, \lambda_4$ in decreasing order. Then the concurrence of ρ is

$$C(\rho) = \max(0, \lambda_1 - \lambda_2 - \lambda_3 - \lambda_4). \tag{1.63}$$

Nonzero concurrence indicates the state is entangled. Unit concurrence indicates a maximally entangled state.

For example, the concurrence of the identity matrix $\mathbb{1}$ is zero; there is no entanglement present as it is a completely mixed state. Conversely, the concurrence of the $|\Psi^-\rangle$ Bell state is unity as it is a maximally entangled state.

We can also examine a class of states called Werner states [111]. A Werner state is a linear combination of a maximally mixed state and a maximally entangled state:

$$\rho_W = p|\Psi^-\rangle\langle\Psi^-| + (1-p)\frac{\mathbb{1}}{4}, \tag{1.64}$$

where p is the probability of observing the entangled state $|\Psi^-\rangle$. In Fig. 1.13, we show the concurrence of the Werner state as a function of p. The concurrence is zero when $p < 1/3$; this is because below $1/3$, the density matrix is still separable as the mixed portion overwhelms the entangled portion.

1.5 Hong-Ou-Mandel Interference

One of the most intriguing phenomena in quantum mechanics is Hong-Ou-Mandel (HOM) interference, wherein two identical photons incident on two different input ports of a beamsplitter will always exit at the same output port. This unintuitive consequence of quantum probability amplitudes is a very useful tool for a variety of applications ranging from characterising single-photon sources to entangling photon pairs that have not interacted.

HOM interference is an integral part of this thesis, and as such we will discuss it at length. In this section we will describe the mathematics of how HOM interference occurs, and then we will discuss relevant applications.

1.5.1 Mathematical Description

Consider a 50:50 non-polarising beamsplitter with two input ports a_1 and a_2 and two output ports a_3 and a_4, as shown in Fig. 1.14. The unitary transformation of the beamsplitter is given by

$$\begin{pmatrix} a_1 \\ a_2 \end{pmatrix} = \frac{1}{\sqrt{2}} \begin{pmatrix} 1 & 1 \\ 1 & -1 \end{pmatrix} \begin{pmatrix} a_3 \\ a_4 \end{pmatrix}. \tag{1.65}$$

The unintuitive order of this equation, i.e., obtaining input modes from output modes, is due to the way we will use the transformation momentarily. We will start out with an expression that is represented with input modes and will replace it with the corresponding expression that uses output modes; this makes the mathematics easier than applying the matrix transformation to the initial expression.

A pair of single photons, each incident on one input port, can be described by the state

$$|\psi\rangle = |1\rangle_{a_1}|1\rangle_{a_2} = a_1^\dagger a_2^\dagger |0\rangle_{a_1}|0\rangle_{a_2}, \tag{1.66}$$

where $|n\rangle_{a_i}$ refers to the number of photons in mode a_i and $a_i^\dagger$ is the creation operator for mode a_i.

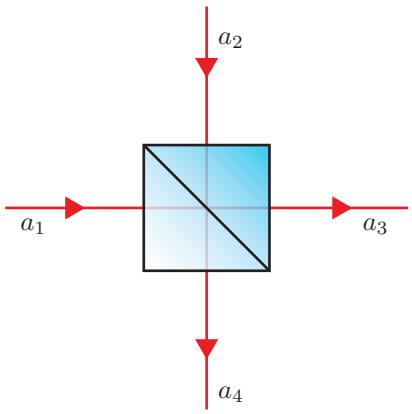

Figure 1.14: **Beamsplitter modes.**

Applying the beamsplitter transformation, we obtain

$$\begin{aligned} |\psi\rangle &\to \frac{1}{\sqrt{2}}\left(a_3^\dagger + a_4^\dagger\right)\frac{1}{\sqrt{2}}\left(a_3^\dagger - a_4^\dagger\right)|0\rangle_{a_3}|0\rangle_{a_4} \\ &= \frac{1}{2}\left(a_3^{\dagger 2} - a_3^\dagger a_4^\dagger + a_4^\dagger a_3^\dagger - a_4^{\dagger 2}\right)|0\rangle_{a_3}|0\rangle_{a_4}. \end{aligned} \tag{1.67}$$

As creation operators of different modes commute, the two cross-terms cancel out, leaving

$$\begin{aligned}|\psi\rangle &= \frac{1}{2}\big(a_3^{\dagger 2} - a_4^{\dagger 2}\big)|0\rangle_{a_3}|0\rangle_{a_4} \\ &= \frac{1}{\sqrt{2}}\big(|2\rangle_{a_3}|0\rangle_{a_4} - |0\rangle_{a_3}|2\rangle_{a_4}\big).\end{aligned} \tag{1.68}$$

Thus the two photons always exit the beamsplitter at the same port; this is sometimes referred to as photon bunching.

1.5.2 Bell State Measurements

We can use the principle of photon bunching to distinguish between the four Bell states. Take for example the anti-correlated Bell states $|\Psi^{\pm}\rangle$ with each photon incident on a different input of a non-polarising beamsplitter. Using the creation operators for the beamsplitter input modes, we can write the states as

$$\begin{aligned}|\Psi^{\pm}\rangle &= \frac{1}{\sqrt{2}}\big(|H\rangle_{a_1}|V\rangle_{a_2} \pm |V\rangle_{a_1}|H\rangle_{a_2}\big) \\ &= \frac{1}{\sqrt{2}}\big(a_{1H}^{\dagger}a_{2V}^{\dagger} \pm a_{1V}^{\dagger}a_{2H}^{\dagger}\big)|0\rangle_{a_1}|0\rangle_{a_2},\end{aligned} \tag{1.69}$$

where $a_{iH}^{\dagger}$ ($a_{iV}^{\dagger}$) is the creation operator for a photon with horizontal (vertical) polarisation in mode a_i.

Applying the beamsplitter operation, we obtain

$$\begin{aligned}|\Psi^{\pm}\rangle \rightarrow \frac{1}{\sqrt{2}}\Bigg[&\frac{1}{\sqrt{2}}\big(a_{3H}^{\dagger} + a_{4H}^{\dagger}\big)\frac{1}{\sqrt{2}}\big(a_{3V}^{\dagger} - a_{4V}^{\dagger}\big) \\ &\pm \frac{1}{\sqrt{2}}\big(a_{3V}^{\dagger} + a_{4V}^{\dagger}\big)\frac{1}{\sqrt{2}}\big(a_{3H}^{\dagger} - a_{4H}^{\dagger}\big)\Bigg]|0\rangle_{a_3}|0\rangle_{a_4} \\ = \frac{1}{2\sqrt{2}}\Bigg[&\big(a_{3H}^{\dagger}a_{3V}^{\dagger} - a_{3H}^{\dagger}a_{4V}^{\dagger} + a_{4H}^{\dagger}a_{3V}^{\dagger} - a_{4H}^{\dagger}a_{4V}^{\dagger}\big) \\ &\pm \big(a_{3V}^{\dagger}a_{3H}^{\dagger} - a_{3V}^{\dagger}a_{4H}^{\dagger} + a_{4V}^{\dagger}a_{3H}^{\dagger} - a_{4V}^{\dagger}a_{4H}^{\dagger}\big)\Bigg]|0\rangle_{a_3}|0\rangle_{a_4} \\ = &\begin{cases}\frac{1}{2\sqrt{2}}\Big(2a_{3H}^{\dagger}a_{3V}^{\dagger} - 2a_{4H}^{\dagger}a_{4V}^{\dagger}\Big)|0\rangle_{a_3}|0\rangle_{a_4}, & \text{for } |\Psi^{+}\rangle \\ \frac{1}{2\sqrt{2}}\Big(-2a_{3H}^{\dagger}a_{4V}^{\dagger} + 2a_{4H}^{\dagger}a_{3V}^{\dagger}\Big)|0\rangle_{a_3}|0\rangle_{a_4}, & \text{for } |\Psi^{-}\rangle\end{cases} \\ = &\begin{cases}\frac{1}{\sqrt{2}}\Big(|H\rangle_{a_3}|V\rangle_{a_3}|0\rangle_{a_4} - |0\rangle_{a_3}|H\rangle_{a_4}|V\rangle_{a_4}\Big), & \text{for } |\Psi^{+}\rangle \\ \frac{1}{\sqrt{2}}\Big(-|H\rangle_{a_3}|V\rangle_{a_4} + |V\rangle_{a_3}|H\rangle_{a_4}\Big) = -|\Psi^{-}\rangle, & \text{for } |\Psi^{-}\rangle.\end{cases}\end{aligned} \tag{1.70}$$

Other than a global phase, the $|\Psi^{-}\rangle$ state remains unaltered – one photon exits in mode a_3, the other exits in mode a_4. This is referred to as anti-bunching. Conversely,

the photons in the state $|\Psi^+\rangle$ bunch, exiting the beamsplitter at the same port with opposite polarisations.

Now take the correlated Bell states $|\Phi^\pm\rangle$ in the same scenario. Using the creation operators, we can write the states as

$$\begin{aligned}|\Phi^\pm\rangle &= \frac{1}{\sqrt{2}}\big(|H\rangle_{a_1}|H\rangle_{a_2} \pm |V\rangle_{a_1}|V\rangle_{a_2}\big) \\ &= \frac{1}{\sqrt{2}}\big(a^\dagger_{1H}a^\dagger_{2H} \pm a^\dagger_{1V}a^\dagger_{2V}\big)|0\rangle_{a_1}|0\rangle_{a_2}. \end{aligned} \tag{1.71}$$

Applying the beamsplitter operation, we obtain

$$\begin{aligned}|\Phi^\pm\rangle \rightarrow \frac{1}{\sqrt{2}}\Bigg[&\frac{1}{\sqrt{2}}\big(a^\dagger_{3H} + a^\dagger_{4H}\big)\frac{1}{\sqrt{2}}\big(a^\dagger_{3H} - a^\dagger_{4H}\big) \\ &\pm \frac{1}{\sqrt{2}}\big(a^\dagger_{3V} + a^\dagger_{4V}\big)\frac{1}{\sqrt{2}}\big(a^\dagger_{3V} - a^\dagger_{4V}\big)\Bigg]|0\rangle_{a_3}|0\rangle_{a_4} \\ = \frac{1}{2\sqrt{2}}\Big[&\big({a^\dagger_{3H}}^2 - a^\dagger_{3H}a^\dagger_{4H} + a^\dagger_{4H}a^\dagger_{3H} - {a^\dagger_{4H}}^2\big) \\ &\pm \big({a^\dagger_{3V}}^2 - a^\dagger_{3V}a^\dagger_{4V} + a^\dagger_{4V}a^\dagger_{3V} - {a^\dagger_{4V}}^2\big)\Big]|0\rangle_{a_3}|0\rangle_{a_4} \\ = \frac{1}{2\sqrt{2}}\Big[&\big({a^\dagger_{3H}}^2 - {a^\dagger_{4H}}^2\big) \pm \big({a^\dagger_{3V}}^2 - {a^\dagger_{4V}}^2\big)|0\rangle_{a_3}|0\rangle_{a_4}\Big] \\ = \frac{1}{2}\Big[&\big(|H\rangle_{a_3}|H\rangle_{a_3}|0\rangle_{a_4} - |0\rangle_{a_3}|H\rangle_{a_4}|H\rangle_{a_4}\big) \pm \big(|V\rangle_{a_3}|V\rangle_{a_3}|0\rangle_{a_4} - |0\rangle_{a_3}|V\rangle_{a_4}|V\rangle_{a_4}\big)\Big] \\ = \frac{1}{2}\Big[&\big(|H\rangle_{a_3}|H\rangle_{a_3} \pm |V\rangle_{a_3}|V\rangle_{a_3}\big)|0\rangle_{a_4} - |0\rangle_{a_3}\big(|H\rangle_{a_4}|H\rangle_{a_4} \pm |V\rangle_{a_4}|V\rangle_{a_4}\big)\Big], \end{aligned} \tag{1.72}$$

Here the photons have bunched – both photons always exit in the same output mode, with identical polarisation. Fig. 1.15 shows the possible results when a Bell state is incident on a beamsplitter.

Considering these results, we are able to distinguish between two of the four Bell states. If we observe one photon in each output mode, then we can conclude the photons successfully projected into the $|\Psi^-\rangle$ state; this is the easiest state to distinguish. If we insert a polarising beamsplitter into each of the output modes, and we observe one photon of each polarisation in a single output mode, we can conclude the photons successfully projected into the $|\Psi^+\rangle$ state.

An example setup is shown in Fig. 1.16. The light blue beamsplitter represents a 50:50 non-polarising beamsplitter, while the dark blue beamsplitters represent polarising beamsplitters. If either detector D_{1H} or detector D_{1V} fires at the same time as either detector D_{2H} or detector D_{2V}, then the photons projected into the $|\Psi^-\rangle$ state. If both detectors D_{1H} and D_{1V} fire at the same time, or if both detectors D_{2H} and D_{2V} fire at the same time, then we know that the photons projected into the $|\Psi^+\rangle$ state.

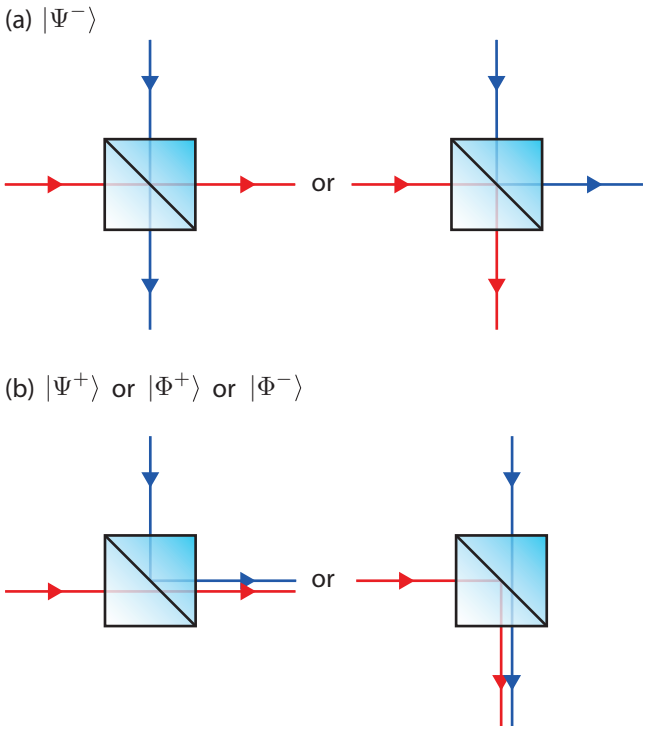

Figure 1.15: **Bell state behaviour at a beamsplitter.** (a) The state $|\Psi^-\rangle$ incident on a beamsplitter will always anti-bunch. (b) The remaining three Bell states will always bunch.

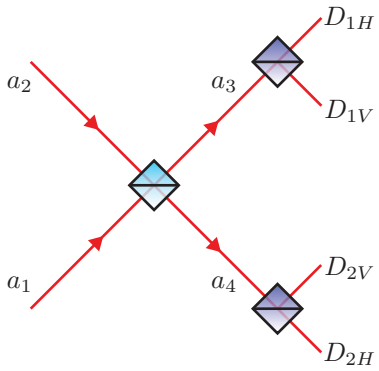

Figure 1.16: **Bell state measurement.** The $|\Psi^-\rangle$ state produces a coincidence between one of the detectors 1 and one of the detectors 2. The $|\Psi^+\rangle$ state produces a coincidence between either both detectors 1 or both detectors 2. The $|\Phi^\pm\rangle$ states produce a double count in any of the four detectors, making accurate detection difficult.

Figure 1.17: **Quantum vs. regular teleportation.** Source: xkcd.com/465.

The final two Bell states $|\Phi^{\pm}\rangle$ are more difficult to distinguish as the two photons have the same polarisation in the same output mode. In theory, a 50:50 beamsplitter in each of the four polarisation outputs could detect the existence of two photons of the same polarisation in the same mode; however, this is a probabilistic measurement and thus not very practical. Additionally, this would only indicate that the photons projected into either $|\Phi^{+}\rangle$ or $|\Phi^{-}\rangle$; we would still be unable to distinguish between the two. In fact, it is impossible to distinguish between all four Bell states using only linear optics [46]. Nonetheless, the ability to distinguish even two of the four Bell states is core to one of the most interesting applications of quantum mechanics: quantum teleportation.

1.5.3 Quantum Teleportation

Quantum teleportation is often optimistically misunderstood by the general public; see Fig. 1.17. The term conjures up images of Star Trek's transporter technology, which allows characters in the fictional universe to disappear in one location and reappear instantly in another. Certainly this technology would be welcome; we would never have to deal with traffic again! However, there are physical limitations that do not allow this technology to exist. What we do have is quantum teleportation, the results of which are similar to fictional transporter technology, but on a much smaller (and less deterministic) scale.

Quantum teleportation is not a method to transport people from one location to another. Rather, it is a means of replicating the state of a particle to another, possibly distant, particle. The key is that the second particle must already exist and must be entangled with an ancillary particle; the information is merely transferred to the second particle via this entanglement. We will examine exactly how this happens.

Bob has a quantum state $\alpha|H\rangle_{\mathrm{B}} + \beta|V\rangle_{\mathrm{B}}$ that he would like Delilah to have; see Fig. 1.18. He also has a pair of entangled photons in the state $|\Psi^{+}\rangle_{\mathrm{DC}}$ to facilitate this. He sends photon D to Delilah, keeping its entangled pair C. He then performs a Bell state measurement on the two photons he retains: B and C. These two photons

are not entangled before the measurement; they will project into one of the four Bell states with equal probability, entangling them. When Bob obtains the result of this measurement, he sends the outcome to Delilah classically. She then performs a unitary operation on her photon depending on the measurement outcome in order to obtain the desired state in her photon D.

To understand the mathematics of teleportation, we will consider the 25% chance of projection into $|\Psi^-\rangle$ as this is the most easily distinguished scenario due to its anti-bunching effect. The three photons start out in the combined state

$$\begin{aligned}|\psi\rangle &= \big(\alpha|H\rangle_\mathrm{B} + \beta|V\rangle_\mathrm{B}\big) \otimes |\Psi^+\rangle_\mathrm{DC} \\ &= \big(\alpha|H\rangle_\mathrm{B} + \beta|V\rangle_\mathrm{B}\big) \otimes \frac{1}{\sqrt{2}}\big(|H\rangle_\mathrm{D}|V\rangle_\mathrm{C} + |V\rangle_\mathrm{D}|H\rangle_\mathrm{C}\big) \\ &= \frac{1}{\sqrt{2}}\Big[\big(\alpha|H\rangle_\mathrm{B}|V\rangle_\mathrm{C} + \beta|V\rangle_\mathrm{B}|V\rangle_\mathrm{C}\big)|H\rangle_\mathrm{D} + \big(\alpha|H\rangle_\mathrm{B}|H\rangle_\mathrm{C} + \beta|V\rangle_\mathrm{B}|H\rangle_\mathrm{C}\big)|V\rangle_\mathrm{D}\Big].\end{aligned} \tag{1.73}$$

Applying the Bell state measurement and post-selecting for the $|\Psi^-\rangle$ state, we obtain

$$\begin{aligned}\langle\Psi^-|_\mathrm{BC}|\psi\rangle = \frac{1}{\sqrt{2}}\Big[\langle H|_\mathrm{B}\langle V|_\mathrm{C} - \langle V|_\mathrm{B}\langle H|_\mathrm{C}\Big] \times \\ \frac{1}{\sqrt{2}}\Big[\big(\alpha|H\rangle_\mathrm{B}|V\rangle_\mathrm{C} + \beta|V\rangle_\mathrm{B}|V\rangle_\mathrm{C}\big)|H\rangle_\mathrm{D} + \big(\alpha|H\rangle_\mathrm{B}|H\rangle_\mathrm{C} + \beta|V\rangle_\mathrm{B}|H\rangle_\mathrm{C}\big)|V\rangle_\mathrm{D}\Big] \\ = \frac{1}{2}\big(\alpha|H\rangle_\mathrm{D} - \beta|V\rangle_\mathrm{D}\big).\end{aligned} \tag{1.74}$$

The initial state of Bob's photon has now been transferred to Delilah's photon, with two minor differences. Firstly, the phase between the horizontal and vertical components is negative; this can be remedied with the simple unitary operation

$$U(\Psi^-) = \begin{pmatrix} 1 & 0 \\ 0 & -1 \end{pmatrix}, \tag{1.75}$$

which can be realised experimentally with a half-wave plate.

Secondly, there is an additional factor of 1/2 in front of the state, indicating that this particular outcome occurs with 25% probability. Each of the other three Bell states make up the other 75% probability; each outcome will result in a slightly different state in Delilah's photon:

$$\langle\Psi^+|_\mathrm{BC}|\psi\rangle = \frac{1}{2}\big(\alpha|H\rangle_\mathrm{D} + \beta|V\rangle_\mathrm{D}\big) \tag{1.76}$$

$$\langle\Phi^+|_\mathrm{BC}|\psi\rangle = \frac{1}{2}\big(\beta|H\rangle_\mathrm{D} + \alpha|V\rangle_\mathrm{D}\big) \tag{1.77}$$

$$\langle\Phi^-|_\mathrm{BC}|\psi\rangle = \frac{1}{2}\big(\beta|H\rangle_\mathrm{D} - \alpha|V\rangle_\mathrm{D}\big), \tag{1.78}$$

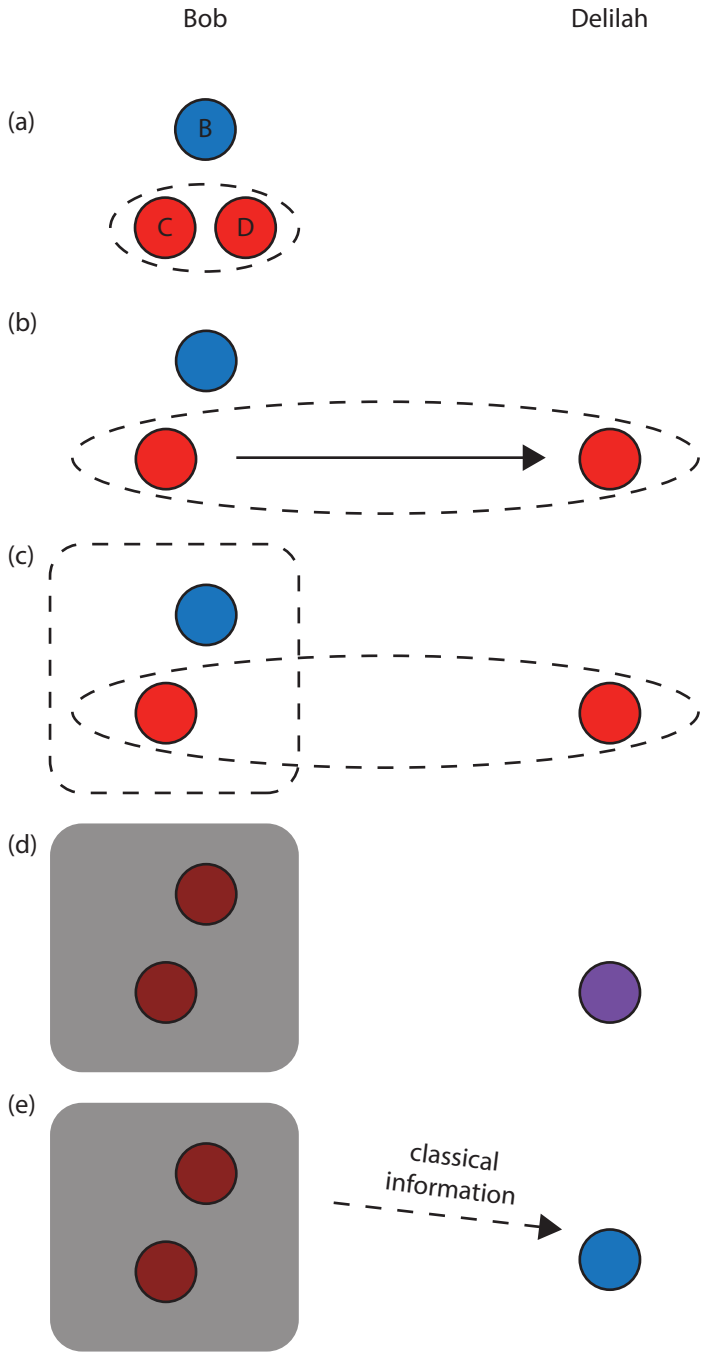

Figure 1.18: **Teleportation.** (a) Bob begins with the state he wants to teleport on photon B (blue) and a pair of entangled photons C and D (red). (b) He sends photon D to Delilah; photons C and D retain their entanglement during this process. (c) Bob performs a Bell state measurement on his remaining photons B and C. (d) The Bell state measurement collapses the entanglement between particles C and D while simultaneously entangling photons B and C, destroying the state of photon B. (e) Bob transmits classical information to Delilah about his Bell measurement, allowing her to transfer the state from photon B to photon D. The state has been teleported.

which can be transformed to the desired state using different unitaries:

$$U(\Psi^+) = \begin{pmatrix} 1 & 0 \\ 0 & 1 \end{pmatrix} \tag{1.79}$$

$$U(\Phi^+) = \begin{pmatrix} 0 & 1 \\ 1 & 0 \end{pmatrix} \tag{1.80}$$

$$U(\Phi^-) = \begin{pmatrix} 0 & 1 \\ -1 & 0 \end{pmatrix}. \tag{1.81}$$

Thus, if we could distinguish between all four Bell states, we could perform completely deterministic teleportation. However, as it is, we can realistically only distinguish two Bell states with linear optics. Since the $|\Psi^-\rangle$ state is the easiest to distinguish, many experimental implementations use only that and thus function at maximum 25% efficiency.

1.5.4 Entanglement Swapping

An interesting consequence of quantum teleportation is entanglement swapping. By teleporting the state of a photon that is entangled with another, we can create entanglement between two photons that have not interacted.

Alice holds a pair of entangled photons in the state $|\Psi^+\rangle_{\mathrm{AB}}$, and Delilah holds a pair of entangled photons in the state $|\Psi^+\rangle_{\mathrm{CD}}$; see Fig. 1.19. Alice and Delilah would like to share a pair of entangled photons, so they send photons B and C to a third party. A Bell state measurement is then performed on photons B and C. Postselecting on the $|\Psi^-\rangle_{\mathrm{BC}}$ state, we obtain

$$\begin{aligned}
\langle\Psi^-|_{\mathrm{BC}}|\Psi^+\rangle_{\mathrm{AB}} \otimes |\Psi^+\rangle_{\mathrm{CD}} = &\left[\frac{1}{\sqrt{2}}\Big(\langle H|_{\mathrm{B}}\langle V|_{\mathrm{C}} - \langle V|_{\mathrm{B}}\langle H|_{\mathrm{C}}\Big)\right]\times \\
&\left[\frac{1}{\sqrt{2}}\Big(|H\rangle_{\mathrm{A}}|V\rangle_{\mathrm{B}} + |V\rangle_{\mathrm{A}}|H\rangle_{\mathrm{B}}\Big) \otimes \frac{1}{\sqrt{2}}\Big(|H\rangle_{\mathrm{C}}|V\rangle_{\mathrm{D}} + |V\rangle_{\mathrm{C}}|H\rangle_{\mathrm{D}}\Big)\right] \\
&= \frac{1}{2\sqrt{2}}\Big(|V\rangle_{\mathrm{A}}|H\rangle_{\mathrm{D}} - |H\rangle_{\mathrm{A}}|V\rangle_{\mathrm{D}}\Big) \\
&= -\frac{1}{2}|\Psi^-\rangle_{\mathrm{AD}}.
\end{aligned} \tag{1.82}$$

Photons A and D are now entangled, even though only photons B and C interacted. We can recover the original entangled state $|\Psi^+\rangle_{\mathrm{AD}}$ by performing a unitary transformation on one of the photons based on the classical information received from the Bell measurement. In this case, we perform on photon D the local unitary operation

$$U(\Psi^-) = \begin{pmatrix} 1 & 0 \\ 0 & -1 \end{pmatrix}. \tag{1.83}$$

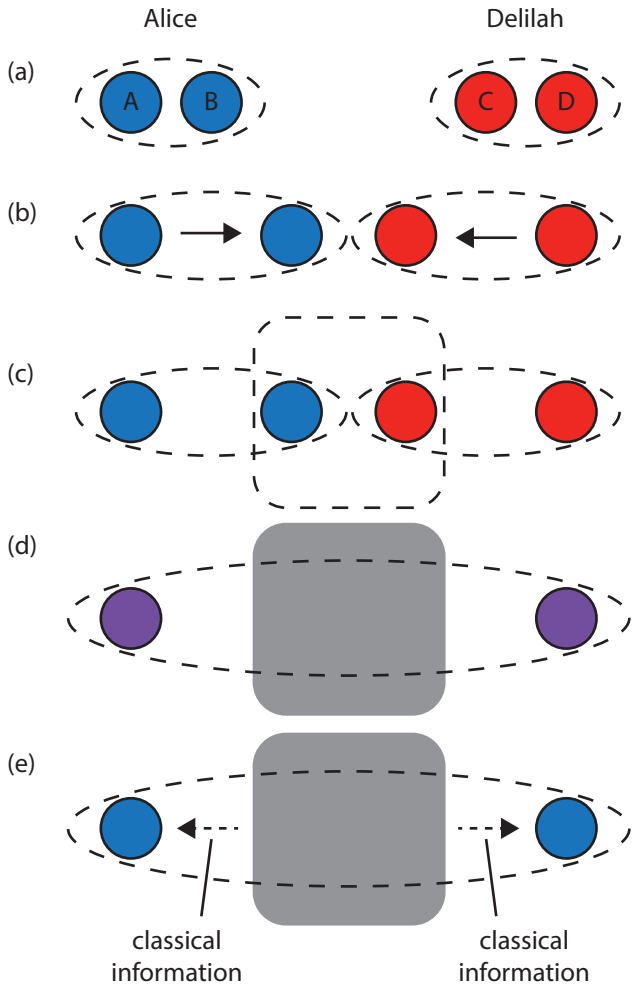

Figure 1.19: **Entanglement swapping.** (a) Alice and Delilah each begin with an entangled pair of photons, A and B (blue) and C and D (red), respectively. (b) Each of them send one of their photons to a third party; the two photon pairs retain their individual entanglement during this process. (c) The third party performs a Bell state measurement on photons B and C. (d) The Bell state measurement collapses the entanglement between particles A and B and between C and D, while simultaneously entangling photons B and C and therefore photons A and D. (e) The third party transmits classical information to Delilah about the Bell measurement, allowing her to perform a local operation to recover the desired entangled state. The entanglement has successfully been swapped from photons A and B to photons A and D.

Note again that the extra factor of $-1/2$ indicates a 25% chance of projecting into $|\Psi^-\rangle_{\mathrm{BC}}$. The other 75% of the time, we project onto a different Bell state, with different outcomes:

$$\langle\Psi^+|_{\mathrm{BC}}|\Psi^+\rangle_{\mathrm{AB}} \otimes |\Psi^+\rangle_{\mathrm{CD}} = \frac{1}{2}|\Psi^+\rangle_{\mathrm{AD}} \tag{1.84}$$

$$\langle\Phi^+|_{\mathrm{BC}}|\Psi^+\rangle_{\mathrm{AB}} \otimes |\Psi^+\rangle_{\mathrm{CD}} = \frac{1}{2}|\Phi^+\rangle_{\mathrm{AD}} \tag{1.85}$$

$$\langle\Phi^-|_{\mathrm{BC}}|\Psi^+\rangle_{\mathrm{AB}} \otimes |\Psi^+\rangle_{\mathrm{CD}} = -\frac{1}{2}|\Phi^-\rangle_{\mathrm{AD}}. \tag{1.86}$$

These can be returned to the original state using local unitaries in photon D:

$$U(\Psi^+) = \begin{pmatrix} 1 & 0 \\ 0 & 1 \end{pmatrix} \tag{1.87}$$

$$U(\Phi^+) = \begin{pmatrix} 0 & 1 \\ 1 & 0 \end{pmatrix} \tag{1.88}$$

$$U(\Phi^-) = \begin{pmatrix} 0 & 1 \\ -1 & 0 \end{pmatrix}. \tag{1.89}$$

Chapter 2

Engineering Two-Photon High-Dimensional States through Quantum Interference

2.1 Notes and Acknowledgements

In this chapter, we describe a filter for two-dimensional anti-symmetric states in the orbital angular momentum of light. This filter consists of a beamsplitter to implement Hong-Ou-Mandel interference and two mirrors to compensate for reflections within the beamsplitter. The work in this chapter forms the basis of the quantum interference in chapters 3, 4, and 5.

This work formed part of a collaboration with colleagues from South Africa. A version of it has been published in Science Advances [112]:

Y. Zhang, F.S. Roux, T. Konrad, M. Agnew, J. Leach, A. Forbes, *Engineering two-photon high-dimensional states through quantum interference*, Science Advances **2**, e1501165 (2016).

Contributions to this chapter are as follows:

AF, JL, FSR, and TK conceived the research. YZ performed the experiment. YZ, FSR, TK, and MA developed the theory. YZ, MA, and JL conducted the analyses, and MA performed the state tomography. All authors contributed to the writing of the published manuscript, but the text in this thesis was written exclusively by MA.

2.2 Overview

Hong-Ou-Mandel (HOM) interference is a fundamental component in many quantum information protocols and one of the defining features of quantum science. Traditional HOM measurements are implemented in two-dimensional Hilbert spaces and are used to filter antisymmetric components from a photonic input state. Here, we extend the concept of HOM interference to photons entangled in high dimensions, implementing a HOM measurement for orbital angular momentum (OAM) states. In this manner, we are able to filter the antisymmetric components from a high-dimensional entangled field. We use Dove prisms to control the precise form of the high-dimensional two-photon state and reveal state-specific constructive and destructive quantum interference. This work paves the way for high-dimensional processing of multi-photon quantum states, for example, in teleportation beyond qubits.

2.3 Background

Hong-Ou-Mandel (HOM) interference, the bunching of two indistinguishable photons [63], is an integral part of many quantum information protocols, such as linear-optical quantum computing [113], quantum cloning [114, 115], and characterisation of single-photon sources [69]. In particular, HOM interference can act as a filter for anti-symmetric states; symmetric states bunch, while anti-symmetric states anti-bunch, meaning postselection on coincidence events allows through only the anti-symmetric states. This makes HOM interference essential in quantum teleportation [51, 52] and entanglement swapping [25] as both rely on distinguishing entangled states.

HOM interference has been observed in polarisation [116], path length [117], radial modes [118], and spatial modes [88, 89, 119–121]; it has also been observed to be affected by spectral filtering [122], and it persists even with photons from independent sources [123]. However, most of these implementations have been in two-dimensional systems, despite the strength of spatial modes being in their scalability to high dimensions. High-dimensional quantum systems are increasingly becoming a viable option for enhancing current quantum technology. For example, compared to two-dimensional systems, high-dimensional states result in stronger security and higher transmission rates in communication protocols [124]. A number of high-dimensional degrees of freedom have been investigated, such as time-energy [125], path [126], spatial modes [31, 92, 127], and combinations thereof [128, 129].

In particular, the orbital angular momentum (OAM) of light [31, 64, 82, 98, 130] is a promising degree of freedom for protocols such as high-dimensional quantum

teleportation [131, 132]. Indeed, teleportation has been demonstrated with photons hyper-entangled in both polarisation and two-level OAM states [53,54], though high-dimensional OAM teleportation has not yet been demonstrated. As quantum communication relies on teleportation to enable quantum repeaters [133] to extend the range to useful distances, high-dimensional teleportation is a prerequisite for implementing long-distance high-dimensional quantum communication.

In this work, we investigate HOM interference in photons entangled in more than two spatial modes by performing a HOM measurement on high-dimensional OAM states. We demonstrate that the two-dimensional symmetric states are filtered out of the high-dimensional state, while the two-dimensional anti-symmetric states remain. Thus HOM interference can be used to engineer quantum states in high dimensions: we select transmitted subspaces by rotating Dove prisms to change which subspaces are symmetric and which are anti-symmetric.

2.4 Anti-Symmetric State Filter

In this work, we examine how Hong-Ou-Mandel interference acts on high-dimensional states. In particular, we use a pair of photons entangled in their orbital angular momentum; the general state of a pair of photons in a high-dimensional OAM space can be described as a linear superposition of all possible OAM Bell states

$$\sum_{\ell,k>\ell}\Big[\alpha_{\ell k}|\Phi^{+}_{\ell k}\rangle+\beta_{\ell k}|\Phi^{-}_{\ell k}\rangle+\gamma_{\ell k}|\Psi^{+}_{\ell k}\rangle+\eta_{\ell k}|\Psi^{-}_{\ell k}\rangle\Big], \tag{2.1}$$

where ℓ and k can in principle be any integer value. Here the basis states are

$$|\Phi^{\pm}_{\ell k}\rangle=\frac{1}{\sqrt{2}}\big(|\ell\rangle_1|\ell\rangle_2\pm|k\rangle_1|k\rangle_2\big) \tag{2.2}$$

$$|\Psi^{\pm}_{\ell k}\rangle=\frac{1}{\sqrt{2}}\big(|\ell\rangle_1|k\rangle_2\pm|k\rangle_1|\ell\rangle_2\big), \tag{2.3}$$

where $|\ell\rangle_i$ represents a photon of OAM $\ell\hbar$ in mode a_i. Thus to determine how Hong-Ou-Mandel interference affects high-dimensionally entangled states, we need only examine how each of the four basis states for each subspace, $|\Phi^{\pm}_{\ell k}\rangle$ and $|\Psi^{\pm}_{\ell k}\rangle$, behave under Hong-Ou-Mandel interference.

Typically, HOM interference is achieved using a beamsplitter; however, spatial states present a special case wherein reflection causes a change in the state. For example, OAM state $|\ell\rangle$, when reflected once, reverses its sign to become OAM state $|-\ell\rangle$. As the modes in a beamsplitter experience different reflections depending on whether they are transmitted or reflected as seen in Fig. 2.1(a), spatial modes are not preserved through a beamsplitter and thus do not experience the appropriate

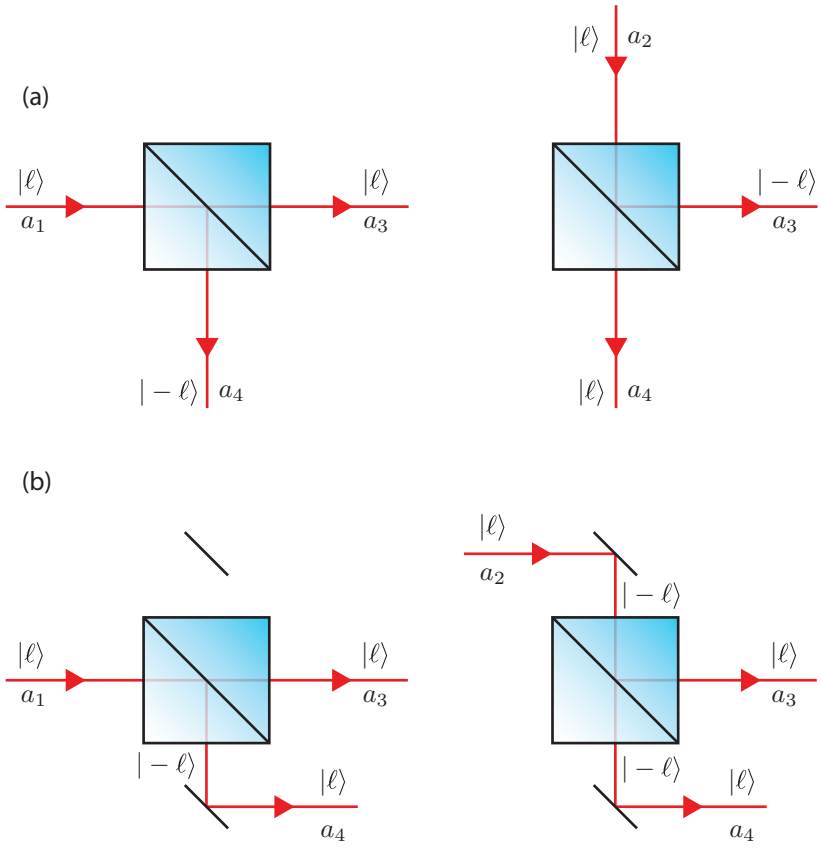

Figure 2.1: **Behaviour of orbital angular momentum in a beamsplitter.** (a) The two output ports of a beamsplitter experience different numbers of reflections, resulting in inconsistent output states. For example, $|\ell\rangle$ entering in mode a_1 exits correctly as $|\ell\rangle$ in mode a_3 but incorrectly as $|-\ell\rangle$ in mode a_4 due to the extra reflection. (b) Placing a mirror before and after the beamsplitter in one mode equalises the number of reflections, and modes a_3 and a_4 now have the correct OAM mode.

interference. As a result, we must add a mirror in one input mode and its corresponding output mode in order to ensure the incoming OAM will be the same as the outgoing OAM, as shown in Fig. 2.1(b).

The unitary operation of this mirror-beamsplitter-mirror combination is described by

$$\begin{pmatrix} \ell_1^\dagger \\ \ell_2^\dagger \end{pmatrix} = \frac{1}{\sqrt{2}} \begin{pmatrix} 1 & 1 \\ 1 & -1 \end{pmatrix} \begin{pmatrix} \ell_3^\dagger \\ \ell_4^\dagger \end{pmatrix}, \tag{2.4}$$

where $\ell_i^\dagger$ is the creation operator for a photon with OAM $\ell\hbar$ in mode a_i.

Take for example the anti-correlated states, which can be written as

$$|\Psi_{\ell k}^{\pm}\rangle = \frac{1}{\sqrt{2}}\big(\ell_1^\dagger k_2^\dagger \pm k_1^\dagger \ell_2^\dagger\big)|\emptyset\rangle_1|\emptyset\rangle_2, \tag{2.5}$$

where we use $|\emptyset\rangle_i$ to denote zero photons in mode a_i to avoid confusion with the OAM state $|0\rangle$.

Applying the unitary to this state, we obtain

$$\begin{aligned}
|\Psi_{\ell k}^{\pm}\rangle \to \frac{1}{\sqrt{2}}\Bigg[& \frac{1}{\sqrt{2}}\big(\ell_3^\dagger + \ell_4^\dagger\big)\frac{1}{\sqrt{2}}\big(k_3^\dagger - k_4^\dagger\big) \\
& \qquad \pm \frac{1}{\sqrt{2}}\big(k_3^\dagger + k_4^\dagger\big)\frac{1}{\sqrt{2}}\big(\ell_3^\dagger - \ell_4^\dagger\big)\Bigg]|\emptyset\rangle_3|\emptyset\rangle_4 \\
= \frac{1}{2\sqrt{2}}\Bigg[& \big(\ell_3^\dagger k_3^\dagger - \ell_3^\dagger k_4^\dagger + \ell_4^\dagger k_3^\dagger - \ell_4^\dagger k_4^\dagger\big) \\
& \qquad \pm \big(k_3^\dagger \ell_3^\dagger - k_3^\dagger \ell_4^\dagger + k_4^\dagger \ell_3^\dagger - k_4^\dagger \ell_4^\dagger\big)\Bigg]|\emptyset\rangle_3|\emptyset\rangle_4 \\
= & \begin{cases} \frac{1}{2\sqrt{2}}\Big(2\ell_3^\dagger k_3^\dagger - 2\ell_4^\dagger k_4^\dagger\Big)|\emptyset\rangle_3|\emptyset\rangle_4, & \text{for } |\Psi_{\ell k}^{+}\rangle \\ \frac{1}{2\sqrt{2}}\Big(-2\ell_3^\dagger k_4^\dagger + 2\ell_4^\dagger k_3^\dagger\Big)|\emptyset\rangle_3|\emptyset\rangle_4, & \text{for } |\Psi_{\ell k}^{-}\rangle \end{cases} \\
= & \begin{cases} \frac{1}{\sqrt{2}}\Big(|\ell\rangle_3|k\rangle_3|\emptyset\rangle_4 - |\emptyset\rangle_3|\ell\rangle_4|k\rangle_4\Big), & \text{for } |\Psi_{\ell k}^{+}\rangle \\ \frac{1}{\sqrt{2}}\Big(-|\ell\rangle_3|k\rangle_4 + |k\rangle_3|\ell\rangle_4\Big) = -|\Psi_{\ell k}^{-}\rangle, & \text{for } |\Psi_{\ell k}^{-}\rangle. \end{cases}
\end{aligned} \tag{2.6}$$

We see that for the $|\Psi_{\ell k}^{+}\rangle$ input state, we observe either both photons in mode a_3 and zero photons in mode a_4, or zero photons in mode a_3 and both photons in mode a_4. Conversely, for the $|\Psi_{\ell k}^{-}\rangle$ input state, we observe one photon in each output mode. Thus, $|\Psi_{\ell k}^{+}\rangle$ bunches, while $|\Psi_{\ell k}^{-}\rangle$ anti-bunches.

Similarly, the correlated states can be written as

$$|\Phi_{\ell k}^{\pm}\rangle = \frac{1}{\sqrt{2}}\big(\ell_1^\dagger \ell_2^\dagger \pm k_1^\dagger k_2^\dagger\big)|\emptyset\rangle_1|\emptyset\rangle_2. \tag{2.7}$$

Applying the unitary, we obtain

$$
\begin{aligned}
|\Phi^{\pm}_{\ell k}\rangle \rightarrow \frac{1}{\sqrt{2}}\Bigg[&\frac{1}{\sqrt{2}}\big(\ell_3^\dagger + \ell_4^\dagger\big)\frac{1}{\sqrt{2}}\big(\ell_3^\dagger - \ell_4^\dagger\big) \\
&\qquad \pm \frac{1}{\sqrt{2}}\big(k_3^\dagger + k_4^\dagger\big)\frac{1}{\sqrt{2}}\big(k_3^\dagger - k_4^\dagger\big)\Bigg]|\emptyset\rangle_3|\emptyset\rangle_4 \\
= \frac{1}{2\sqrt{2}}\Big[&\big(\ell_3^{\dagger 2} - \ell_3^\dagger\ell_4^\dagger + \ell_4^\dagger\ell_3^\dagger - \ell_4^{\dagger 2}\big) \\
&\qquad \pm \big(k_3^{\dagger 2} - k_3^\dagger k_4^\dagger + k_4^\dagger k_3^\dagger - k_4^{\dagger 2}\big)\Big]|\emptyset\rangle_3|\emptyset\rangle_4 \\
= \frac{1}{2\sqrt{2}}\Big[&\big(\ell_3^{\dagger 2} - \ell_4^{\dagger 2}\big) \pm \big(k_3^{\dagger 2} - k_4^{\dagger 2}\big)|\emptyset\rangle_3|\emptyset\rangle_4\Big] \\
= \frac{1}{2}\Big[&\big(|\ell\rangle_3|\ell\rangle_3|\emptyset\rangle_4 - |\emptyset\rangle_3|\ell\rangle_4|\ell\rangle_4\big) \pm \big(|k\rangle_3|k\rangle_3|\emptyset\rangle_4 - |\emptyset\rangle_3|k\rangle_4|k\rangle_4\big)\Big] \\
= \frac{1}{2}\Big[&\big(|\ell\rangle_3|\ell\rangle_3 \pm |k\rangle_3|k\rangle_3\big)|\emptyset\rangle_4 - |\emptyset\rangle_3\big(|\ell\rangle_4|\ell\rangle_4 \pm |k\rangle_4|k\rangle_4\big)\Big]. \qquad (2.8)
\end{aligned}
$$

For both input states, we observe either both photons in mode a_3 and zero photons in mode a_4, or zero photons in mode a_3 and both photons in mode a_4. Thus, the $|\Phi^{\pm}_{\ell k}\rangle$ states both bunch.

As only the anti-symmetric state $|\Psi^{-}_{\ell k}\rangle$ anti-bunches through this mirror-beamsplitter-mirror combination, we refer to it as an anti-symmetric state filter; by post-selecting on coincidences in the output ports, we can use this system to filter out symmetric states so that only anti-symmetric states remain.

2.5 State Preparation

Our goal in this experiment is to observe Hong-Ou-Mandel interference for several different OAM values at the same time, with input states that we can control so that they either bunch or anti-bunch. To this end, we begin with a pair of photons entangled in their orbital angular momentum in the state

$$|\psi\rangle_{\mathrm{AB}} = \sum_{\ell} c_\ell |\ell\rangle_{\mathrm{A}}|-\ell\rangle_{\mathrm{B}}, \qquad (2.9)$$

where $|c_\ell|^2$ indicates the probability of photon A having OAM $\ell\hbar$ and photon B having OAM $-\ell\hbar$. This state can be rewritten as

$$
\begin{aligned}
|\psi\rangle_{\mathrm{AB}} &= \sum_{\ell>0} c_\ell\big(|\ell\rangle_{\mathrm{A}}|-\ell\rangle_{\mathrm{B}} + |-\ell\rangle_{\mathrm{A}}|\ell\rangle_{\mathrm{B}}\big) + c_0|0\rangle_{\mathrm{A}}|0\rangle_{\mathrm{B}} \qquad (2.10)\\
&= \sum_{\ell>0} c_\ell\sqrt{2}|\Psi^{+}_{\ell-\ell}\rangle_{\mathrm{AB}} + c_0|0\rangle_{\mathrm{A}}|0\rangle_{\mathrm{B}}, \qquad (2.11)
\end{aligned}
$$

assuming $c_\ell = c_{-\ell}$. No matter what OAM value the photons take in this scenario, they will bunch through our anti-symmetric state filter, as they will either be indistinguishable (for $\ell = 0$) or in the combined state $|\Psi^{+}_{\ell-\ell}\rangle$. In order to create a state

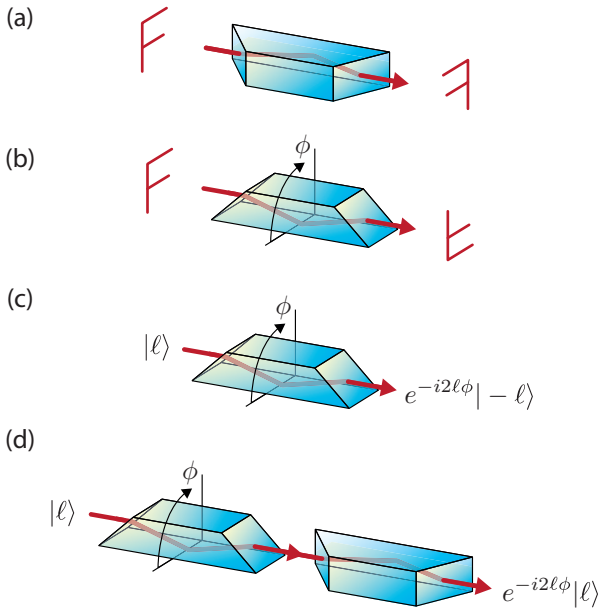

Figure 2.2: **Dove prism.** (a) A single Dove prism placed on its side produces a reflected image of the input. (b) If the Dove prism is rotated by an angle ϕ, the reflected image is also rotated by 2ϕ. (c) If an OAM state $|\ell\rangle$ is incident on a Dove prism at angle ϕ with respect to the horizontal, the output state becomes $e^{-i2\ell\phi}|-\ell\rangle$. (d) Adding a second Dove prism at $\phi = 0$, we produce instead the state $e^{-i2\ell\phi}|\ell\rangle$.

that includes both symmetric and anti-symmetric components, we use Dove prisms to manipulate the OAM state of the photons. (Hereafter we ignore the $\ell = 0$ term as we are only interested in two-dimensional entangled subspaces.)

As shown in Fig. 2.2(a), light passing through a Dove prism undergoes an internal reflection on the largest surface, which reverses the image of the outgoing light. Additionally, if the prism is rotated by an angle ϕ with respect to the horizontal, the outgoing image is rotated by an angle 2ϕ. For OAM, this means that light initially in the state $|\ell\rangle$ will exit the Dove prism in the state $e^{-i2\ell\phi}|-\ell\rangle$ [134]. A second Dove prism reverses the OAM again, so that light passing through two Dove prisms rotated by ϕ with respect to each other will exit in the state $e^{-i2\ell\phi}|\ell\rangle$.

We place two Dove prisms as in Fig. 2.2(d) in arm B of our system. Applying the appropriate transformation to state (2.10), we obtain the state

$$\begin{aligned}
|\psi\rangle_{\mathrm{AB}} \xrightarrow{\text{Dove}} & \sum_{\ell>0} c_\ell \big(|\ell\rangle_{\mathrm{A}} e^{i2\ell\phi}|-\ell\rangle_{\mathrm{B}} + |-\ell\rangle_{\mathrm{A}} e^{-i2\ell\phi}|\ell\rangle_{\mathrm{B}}\big) \\
&= \sum_{\ell>0} c_\ell \Big[|\ell\rangle_{\mathrm{A}}|-\ell\rangle_{\mathrm{B}}\big(\cos(2\ell\phi) + i\sin(2\ell\phi)\big) \\
&\qquad\qquad + |-\ell\rangle_{\mathrm{A}}|\ell\rangle_{\mathrm{B}}\big(\cos(2\ell\phi) - i\sin(2\ell\phi)\big)\Big] \\
&= \sum_{\ell>0} c_\ell \sqrt{2}\Big[\cos(2\ell\phi)|\Psi^+_{\ell-\ell}\rangle_{\mathrm{AB}} + i\sin(2\ell\phi)|\Psi^-_{\ell-\ell}\rangle_{\mathrm{AB}}\Big]. \qquad (2.12)
\end{aligned}$$

Note here we have removed the $\ell = 0$ term as it remains unchanged by the Dove prism transformation and will therefore always bunch, making it inconsequential to this experiment.

Thus with an appropriate choice of ϕ, we can obtain a symmetric state, an anti-symmetric state, or a superposition of both. We can denote a single two-dimensional subspace with OAM values $\pm\ell$ as

$$|\Psi_\ell\rangle_{\mathrm{AB}} = \cos(2\ell\phi)|\Psi^+_{\ell-\ell}\rangle_{\mathrm{AB}} + i\sin(2\ell\phi)|\Psi^-_{\ell-\ell}\rangle_{\mathrm{AB}}. \tag{2.13}$$

For example, placing the Dove prism at an angle $\phi = \pi/4$, we obtain for the $\ell = \pm 1$ subspace

$$|\Psi_1\rangle_{\mathrm{AB}} = i|\Psi^-_{1-1}\rangle_{\mathrm{AB}}, \tag{2.14}$$

a purely anti-symmetric state. Conversely, for the $\ell = \pm 2$ subspace and with the Dove prism at the same angle, we obtain

$$|\Psi_2\rangle_{\mathrm{AB}} = -|\Psi^+_{2-2}\rangle_{\mathrm{AB}}, \tag{2.15}$$

a purely symmetric state.

Removing one of the Dove prisms, we can also obtain an entirely symmetric state. In this case, we obtain the state

$$\begin{aligned}
|\psi\rangle_{\mathrm{AB}} \xrightarrow{\text{Dove}} &\sum_{\ell>0} c_\ell\big(|\ell\rangle_{\mathrm{A}} e^{i2\ell\phi}|\ell\rangle_{\mathrm{B}} + |-\ell\rangle_{\mathrm{A}} e^{-i2\ell\phi}|-\ell\rangle_{\mathrm{B}}\big) \\
&= \sum_{\ell>0} c_\ell\Big[|\ell\rangle_{\mathrm{A}}|\ell\rangle_{\mathrm{B}}\big(\cos(2\ell\phi) + i\sin(2\ell\phi)\big) \\
&\qquad\qquad + |-\ell\rangle_{\mathrm{A}}|-\ell\rangle_{\mathrm{B}}\big(\cos(2\ell\phi) - i\sin(2\ell\phi)\big)\Big] \\
&= \sum_{\ell>0} c_\ell\sqrt{2}\Big[\cos(2\ell\phi)|\Phi^+_{\ell-\ell}\rangle_{\mathrm{AB}} + i\sin(2\ell\phi)|\Phi^-_{\ell-\ell}\rangle_{\mathrm{AB}}\Big].
\end{aligned} \tag{2.16}$$

Thus regardless of ϕ, the state will be symmetric; however, different values of ϕ produce different superpositions of the correlated Bell states. We can denote a single two-dimensional subspace with OAM values $\pm\ell$ as

$$|\Phi_\ell\rangle_{\mathrm{AB}} = \cos(2\ell\phi)|\Phi^+_{\ell-\ell}\rangle_{\mathrm{AB}} + i\sin(2\ell\phi)|\Phi^-_{\ell-\ell}\rangle_{\mathrm{AB}}. \tag{2.17}$$

Looking again at the case where the Dove prism is at an angle $\phi = \pi/4$, we obtain for the $\ell = \pm 1$ subspace

$$|\Phi_1\rangle_{\mathrm{AB}} = i|\Phi^-_{1-1}\rangle_{\mathrm{AB}}. \tag{2.18}$$

For the $\ell = \pm 2$ subspace and with the Dove prism at the same angle, we obtain

$$|\Phi_2\rangle_{\mathrm{AB}} = -|\Phi^+_{2-2}\rangle_{\mathrm{AB}}, \tag{2.19}$$

a purely symmetric state.

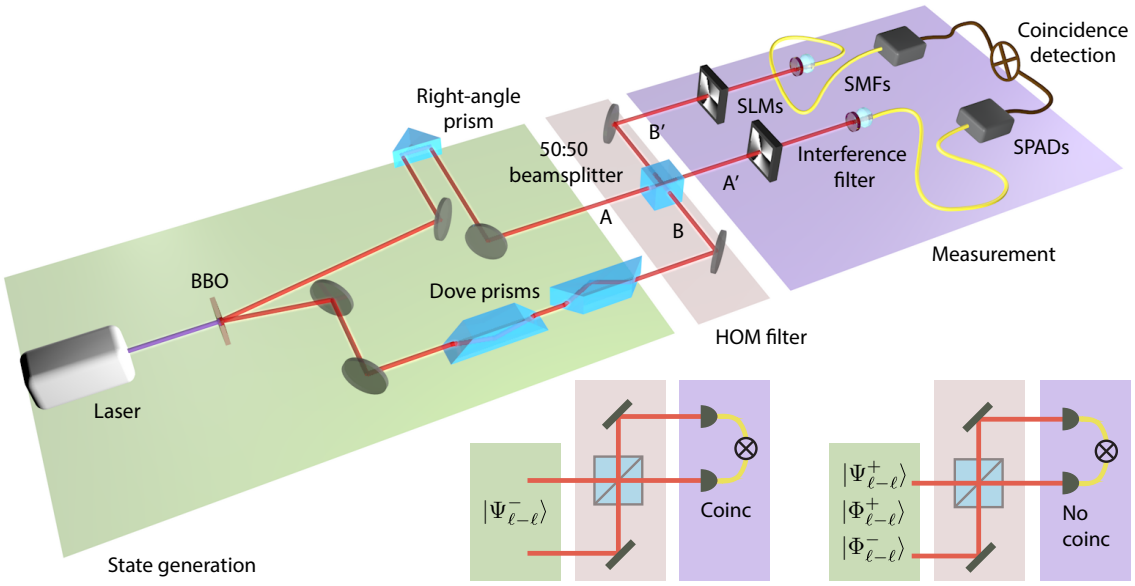

Figure 2.3: **Diagram of the experimental setup used to demonstrate high-dimensional HOM interference.** The HOM filter, indicated by the beige section, consists of two mirrors and a 50:50 beamsplitter. Any antisymmetric state $|\Psi^-_{\ell k}\rangle$ will result in one photon in each of the modes A′ and B′ and the detection of coincidences; any symmetric state $|\Psi^+_{\ell k}\rangle$, $|\Phi^+_{\ell k}\rangle$, or $|\Phi^-_{\ell k}\rangle$ will result in a superposition of two photons in either A′ or B′ and the absence of a coincidence signal. SLM = spatial light modulator, SPAD = single-photon avalanche detector, SMF = single-mode fibre.

2.6 Hong-Ou-Mandel Interference

After the photons are prepared in the desired state, they undergo Hong-Ou-Mandel interference in the antisymmetric state filter. The state in Eq. (2.13) is affected by the filter as follows:

$$\begin{aligned}|\Psi_\ell\rangle_{\mathrm{AB}} &= \cos(2\ell\phi)|\Psi^+_{\ell-\ell}\rangle_{\mathrm{AB}} + i\sin(2\ell\phi)|\Psi^-_{\ell-\ell}\rangle_{\mathrm{AB}} \\ &\xrightarrow{\text{filter}} \cos(2\ell\phi)\frac{1}{\sqrt{2}}\Big(|\ell\rangle_3|-\ell\rangle_3|\emptyset\rangle_4 - |\emptyset\rangle_3|\ell\rangle_4|-\ell\rangle_4\Big) - i\sin(2\ell\phi)|\Psi^-_{\ell-\ell}\rangle. \quad (2.20)\end{aligned}$$

This state exiting the filter has two components: a bunched state with probability $\cos^2(2\ell\phi)$ that will not result in a coincidence detection, and an anti-bunched (antisymmetric) state with probability $\sin^2(2\ell\phi)$ that will result in a coincidence detection. Thus we expect to observe maximal coincidence counts at $\phi = \pi(1+2n)/4\ell$ for any integer n. Conversely, we expect to observe zero coincidence counts at $\phi = n\pi/2\ell$.

Similarly, the state in Eq. (2.17) is affected by the filter as follows:

$$\begin{aligned}|\Phi_\ell\rangle_{\mathrm{AB}} &= \cos(2\ell\phi)|\Phi^+_{\ell-\ell}\rangle_{\mathrm{AB}} + i\sin(2\ell\phi)|\Phi^-_{\ell-\ell}\rangle_{\mathrm{AB}} \\ &\xrightarrow{\text{filter}} \cos(2\ell\phi)\Big[\big(|\ell\rangle_3|\ell\rangle_3 + |-\ell\rangle_3|-\ell\rangle_3\big)|\emptyset\rangle_4 - |\emptyset\rangle_3\big(|\ell\rangle_4|\ell\rangle_4 + |-\ell\rangle_4|-\ell\rangle_4\big)\Big] \\ &\quad + i\sin(2\ell\phi)\Big[\big(|\ell\rangle_3|\ell\rangle_3 - |-\ell\rangle_3|-\ell\rangle_3\big)|\emptyset\rangle_4 - |\emptyset\rangle_3\big(|\ell\rangle_4|\ell\rangle_4 - |-\ell\rangle_4|-\ell\rangle_4\big)\Big] \\ &= e^{i2\ell\phi}\big(|\ell\rangle_3|\ell\rangle_3|\emptyset\rangle_4 - |\emptyset\rangle_3|\ell\rangle_4|\ell\rangle_4\big) + e^{-i2\ell\phi}\big(|-\ell\rangle_3|-\ell\rangle_3|\emptyset\rangle_4 - |\emptyset\rangle_3|-\ell\rangle_4|-\ell\rangle_4\big).\end{aligned} \tag{2.21}$$

This state exiting the filter consists of two components, each of which is a superposition of two photons in path 3 and two photons in path 4. This will produce zero coincidence counts regardless of the value of ϕ.

Thus when we postselect on coincidence counts between paths 3 and 4, the mirrors and beamsplitter act as a filter that only allows antisymmetric states through. As the above analysis leaves ℓ as a variable, the filter acts identically for all values of ℓ; however, we can manipulate which ℓ values are in symmetric and anti-symmetric states in order to observe the filtering effect.

2.7 Summary of Experimental Methods

A 350-mW continuous-wave laser with wavelength 355 nm is used to pump a β-barium borate (BBO) crystal to produce degenerate photon pairs (labelled A and B) entangled in their OAM degree of freedom with Type-I phase matching. The photon in path A is reflected off a right-angle prism mounted on a translational stage that is used to adjust the path length. As there are exactly two internal reflections in the prism and they are both in the plane of propagation, the OAM state remains unchanged. Path B has two Dove prisms which can be rotated to change the phase of the OAM-entangled state to produce $|\Psi_\ell\rangle$. Optionally, we can remove a Dove prism to produce $|\Phi_\ell\rangle$.

The photons are then passed through the HOM filter, which consists of a 50:50 beamsplitter and two mirrors. After the filter, the photons are incident on spatial light modulators (SLMs), which, in combination with single-mode optical fibres (SMFs), allow us to make joint projective measurements of particular spatial modes. The SLMs allow us to consider both two-dimensional subspaces, e.g., where the OAM is restricted to $\ell = \pm 1$, and high-dimensional state spaces, e.g., where the OAM can take on the values $\ell = \pm 1, \pm 2$ and ± 3.

An interference filter of width 10 nm is used to select out photons around 710 nm just before the SMFs. The SMFs are connected to avalanche photodiodes to detect the single photons, and coincidences are registered via a coincidence counter. To maximize the coincidence count rate, we image the photon pairs from the plane

of the BBO crystal onto the SLMs and then from the SLMs into the SMFs. We also adjust the angle of the BBO crystal such that the photon pairs are produced in slightly non-collinear paths (the dip in the ring of light being just visible) as we find this produces around 1.5 times more coincidence counts compared to when the photons are produced collinearly or non-collinearly.

2.8 Results

To test the filter experimentally, we characterise its performance for entangled OAM modes. We first ensure the path length difference between the two inputs is such that the photons undergo Hong-Ou-Mandel interference at the beamsplitter. Fig. 2.4 shows coincidence count rates between the two output arms as the path length difference is varied. When the input state is $|\Psi^-_{1-1}\rangle$, produced by setting $\phi = 0$ with two Dove prisms and setting the SLMs to measure $\ell = 1$ for the signal and $\ell = -1$ for the idler, we observe a peak in the coincidence counts at zero path difference; anti-bunching occurs as expected. When the input state is $|\Psi^+_{1-1}\rangle$, produced by setting $\phi = \pi/4$ with two Dove prisms and setting the SLMs to measure $\ell = 1$ for the signal and $\ell = -1$ for the idler, we observe a dip in the coincidence counts at zero path difference as the photons bunch. All subsequent measurements are made at zero path length difference.

We fit a Gaussian function multiplied by a sinc function to the data, shown as solid lines. For the dip data, we find a vertical offset of 1985.36 counts, while for the peak data, we find a vertical offset of 2229.68 counts. These two values should be identical, but they are slightly different due to the alignment of the Dove prisms. If a Dove prism is even slightly misaligned, a surprisingly large amount of deviation of the beam occurs [134]. This deviation is magnified when rotating the Dove prism from the angle at which it was aligned; thus the difference in baseline counts between the $\phi = 0$ position and the $\phi = \pi/4$ position is not unexpected.

We vary the angle ϕ of the Dove prism to observe the change in coincidence counts based on the superposition of symmetric and anti-symmetric states. Fig. 2.5(a) shows measurements of the $\ell = \pm 1$ subspace for both $|\Phi_1\rangle$ and $|\Psi_1\rangle$. Coincidence counts have been normalised by dividing by the coincidence counts outside of the dip. As expected, we see roughly zero coincidence counts for $|\Phi_1\rangle$ regardless of the value of ϕ. Conversely, the coincidences produced by $|\Psi_1\rangle$ vary with ϕ as the component of the anti-symmetric state is made stronger or weaker as $2\sin^2(2\ell\phi)$; we observe maximal coincidence counts at $\phi = \pi/4$ when $|\Psi^-_{1-1}\rangle$ provides the full contribution to the state, and we observe zero coincidence counts at $\phi = 0$ when $|\Psi^+_{1-1}\rangle$ provides the full contribution to the state.

Fig. 2.5(b) shows the above measurements for the subspace $\ell = \pm 2$. Again, we

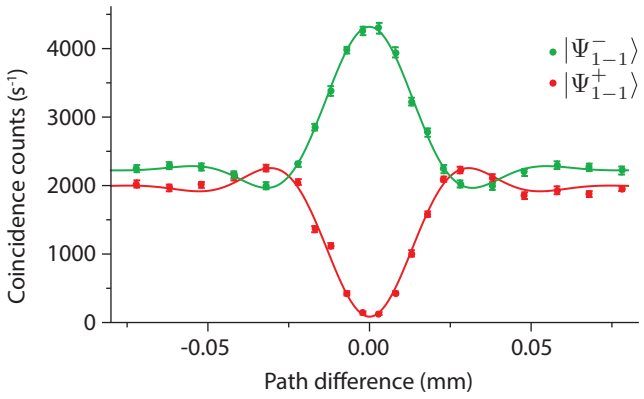

Figure 2.4: **Photon coincidence counts measured as a function of the path length difference.** The red points denote input states $|\Psi^+_{1-1}\rangle$, and the green points denote input states $|\Psi^-_{1-1}\rangle$. We observe a HOM interference dip/peak when the path length difference is equal to zero. The data points shown are the average of 20 readings. A Gaussian function multiplied by a sinc function was fitted to data and is shown as solid curves.

see roughly zero coincidence counts for $|\Phi_2\rangle$ regardless of the value of ϕ, while the coincidences produced by $|\Psi_2\rangle$ vary with ϕ. Due to the factor of $\ell = 2$ in the effect of Dove prism rotation, the period of the variation in coincidences is half the angle of the $\ell = \pm 1$ subspace. As a result, the maximal coincidence counts are found at $\phi = \pi/8$ where $|\Psi^-_{2-2}\rangle$ provides the full contribution to the state.

In Fig. 2.5(c) we show the normalised measurements for each of the eight OAM Bell states measured, taken from Figs. 2.2(a) and (b). Only the $|\Psi^-_{1-1}\rangle$ and $|\Psi^-_{2-2}\rangle$ states result in coincidences, while the other Bell states give approximately zero coincidence counts. All of the preceding measurements were performed twenty times each in order to determine the mean and standard deviation of the count rates. The small standard deviations on the majority of the points indicates a very stable system with very little variation in power.

Finally, we examine the action of the anti-symmetric filter in a high-dimensional space. We set the input state with two Dove prisms at angle $\phi = \pi/4$ with respect to each other; this generates an anti-symmetric state for odd OAM values and a symmetric state for even OAM values. We choose to measure only $\ell = \pm 1, \pm 2, \pm 3$, meaning that our input state from Eq. (2.1) is $|\psi_{\text{in}}\rangle = \eta_{1-1}|\Psi^-_{1-1}\rangle + \gamma_{2-2}|\Psi^+_{2-2}\rangle + \eta_{3-3}|\Psi^-_{3-3}\rangle$, where $|\eta_{1-1}|^2 + |\gamma_{2-2}|^2 + |\eta_{3-3}|^2 = 1$. Passing this state through the anti-symmetric filter, we expect to obtain the state $|\psi_{\text{out}}\rangle = \eta'_{1-1}|\Psi^-_{1-1}\rangle + \eta'_{3-3}|\Psi^-_{3-3}\rangle$, where $|\eta'_{1-1}|^2 + |\eta'_{3-3}|^2 = 1$.

We perform full tomography of the state before and after the filter and reconstruct the high-dimensional density matrix for each state as shown in Fig. 2.6. We have highlighted the two-dimensional subspaces of interest in green ($\ell = \pm 1$), blue ($\ell = \pm 2$), and red ($\ell = \pm 3$), leaving the remaining elements in grey. There are

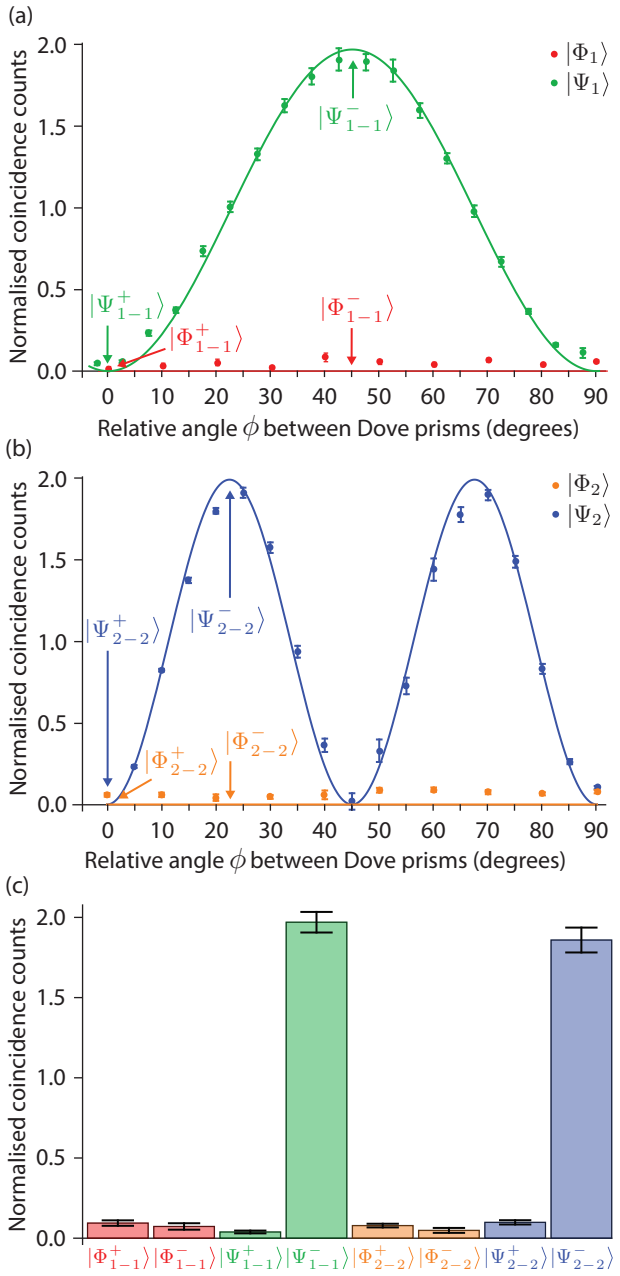

Figure 2.5: **Coincidence counts as a function of input state.** (a) Graph showing the variation of coincidence counts for the input states $|\Psi_1\rangle$, indicated by the green points, and $|\Phi_1\rangle$, indicated by the red points. The theoretical variation in coincidence counts of any $|\Psi_1\rangle$ input state is equal to $2\sin^2(2\phi)$. For any $|\Phi_1\rangle$ input state, the coincidence counts should remain zero as a function of ϕ. The normalized count rate is determined by dividing the coincidence rate in the dip/peak by that outside of the dip/peak. The error bars represent one standard deviation from averaging 20 readings. (b) Graph showing the variation of coincidence counts for the input states $|\Psi_2\rangle$, indicated by the blue points, and $|\Phi_2\rangle$, indicated by the orange points. The theoretical variation in coincidence counts of any $|\Psi_2\rangle$ input state is equal to $2\sin^2(4\phi)$. (c) Normalised coincidence counts for the OAM $\ell = 1$ and 2 Bell states. Only the $|\Psi_1^-\rangle$ and $|\Psi_2^-\rangle$ input states result in coincidences being recorded.

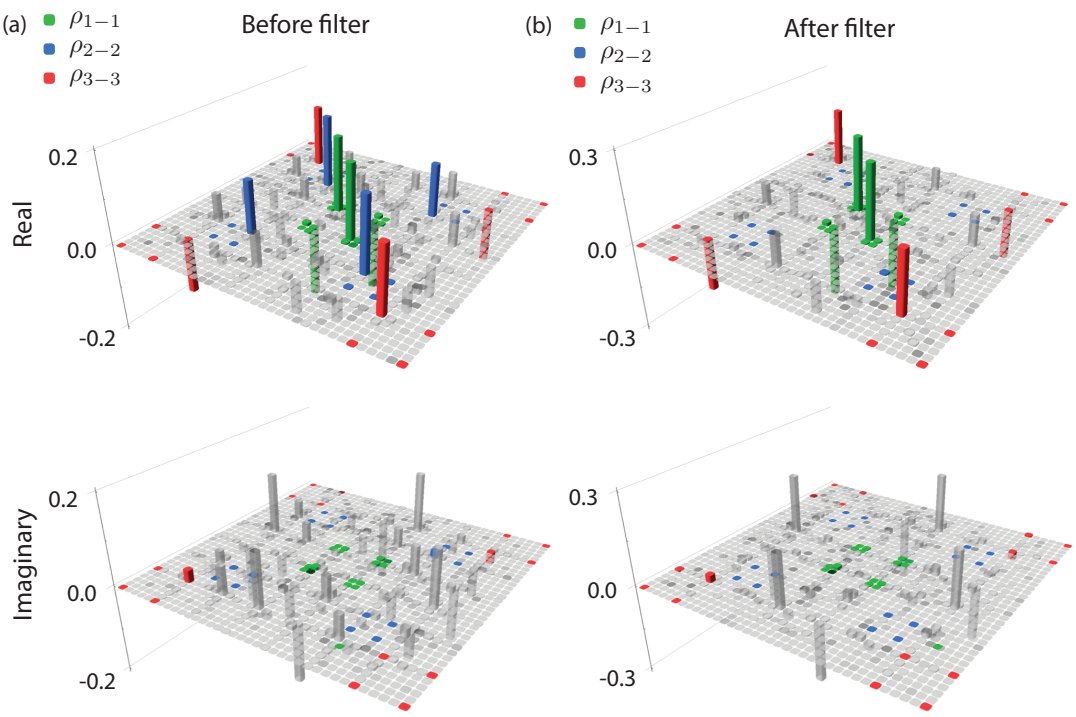

Figure 2.6: **The high-dimensional density matrices corresponding to the states before and after the filter.** (a) The state before the filter is, in principle, given by $\eta_{1-1}|\Psi^-_{1-1}\rangle + \gamma_{2-2}|\Psi^+_{2-2}\rangle + \eta_{3-3}|\Psi^-_{3-3}\rangle$; there is a strong contribution from the $\ell = 1$, 2, and 3 subspaces. (b) The state after the filter is, in principle, given by $\eta'_{1-1}|\Psi^-_{1-1}\rangle + \eta'_{3-3}|\Psi^-_{3-3}\rangle$; the contribution from the $\ell = 2$ subspace is $3.8 \pm 0.2\%$ of its original value. The top panels show the real parts of the density matrices and the bottom panels show the imaginary parts. The diagonal of each density matrix runs vertically from top to bottom.

noticeably large grey bars in several off-diagonal elements; this is to be expected as the state is a (roughly) pure superposition of the three Bell states of interest. If these grey bars did not exist, the density matrix would represent a mixture of the three Bell states, which would indicate entanglement in each two-dimensional subspace, but not in the larger high-dimensional space.

Before the filter (Fig. 2.6(a)), the subspaces contribute approximately equally to the high-dimensional state. In accordance with our predictions, after passing through the filter (Fig. 2.6(b)), the blue ($\ell = \pm 2$) subspace has been effectively filtered out and has only near-zero values, whereas the red and green subspaces remain unchanged (other than a slight increase in the height of the bars due to the requirement of unit trace in the density matrix reconstruction).

In Fig. 2.7, we extract the relevant two-dimensional subspaces from the high-dimensional density matrix. We show the experimental result alongside the theoretically expected result for each subspace both before and after the filter. As we have not measured the OAM distribution explicitly, we compare our experimental

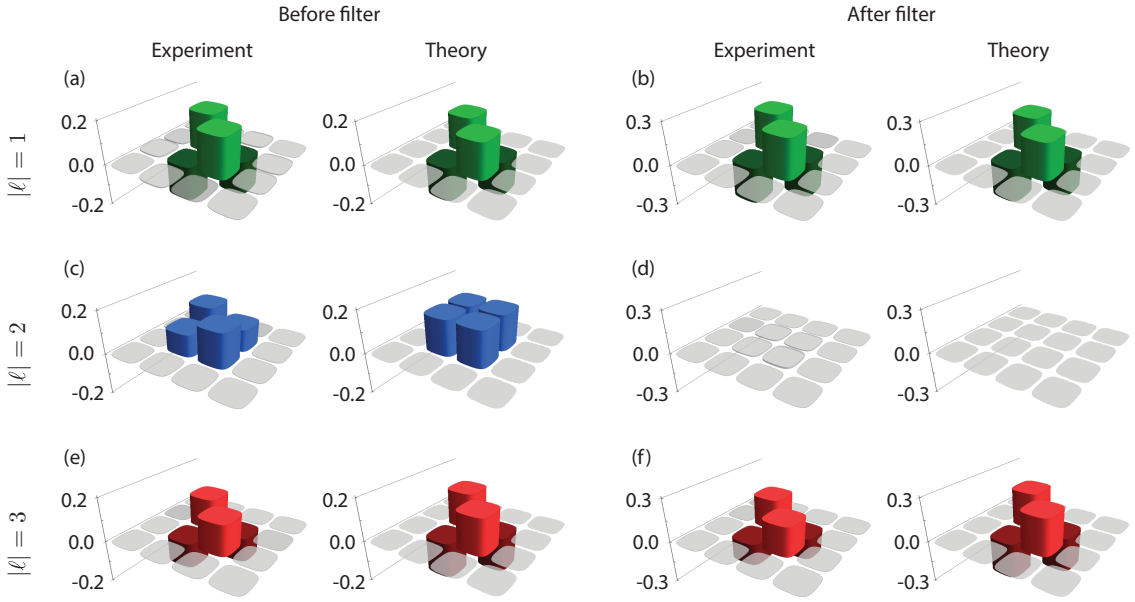

Figure 2.7: **Two-dimensional density matrices.** A comparison of the density matrices of the individual two-dimensional subspaces extracted from Fig. 2.6. Only real parts are shown. The first two columns, (a), (c), and (e), show the subspaces before the filter; the final two columns, (b), (d), and (f), show the subspaces after the filter. Experimental results are shown in the left column of each pair, and theoretical predictions are shown in the right column of each pair. The $\ell = 1$ subspace is shown in green, $\ell = 2$ in blue, and $\ell = 3$ in red. Darker bars indicate negative values, whilst grey bars indicate absolute values less than 0.05. The diagonal of each density matrix runs vertically from top to bottom.

result to theoretical states with a uniform OAM distribution. Thus, theoretical predictions before the filter assume an equal contribution from the three subspaces $|\psi_{\text{in}}\rangle = (|\Psi^-_{1-1}\rangle + |\Psi^+_{2-2}\rangle + |\Psi^-_{3-3}\rangle)/\sqrt{3}$, while predictions after the filter assume an equal contribution from the two remaining subspaces $|\psi_{\text{out}}\rangle = (|\Psi^-_{1-1}\rangle + |\Psi^-_{3-3}\rangle)/\sqrt{2}$. As shown in the figure, the $\ell = \pm 1$ and $\ell = \pm 3$ subspaces remain unchanged besides the trace: before the filter, each represents approximately a third of the state, while after the filter, each represents approximately half of the state. Conversely, the $\ell = \pm 2$ subspace represents a third of the state before the filter, but after the filter it is reduced to less than 2% of the state.

To quantify the performance of the filter, we take the trace of each subspace's density matrix $\rho_{\ell-\ell}$. The trace of $\rho_{\ell-\ell}$ indicates the probability of projecting onto a state with OAM values $\pm\ell$. As shown in Table 2.1, the probability of projecting onto the $\ell = \pm 2$ subspace changes from $31.9 \pm 0.2\%$ before the filter to $1.8 \pm 0.1\%$ after the filter. This corresponds to $3.8 \pm 0.2\%$ of the original signal and is a clear demonstration of effective filtering of the symmetric contribution to the high-dimensional state. We find that there is also a small probability of projecting onto

Subspace	$\mathrm{Tr}[\rho_{\ell-\ell}]$ before the filter	$\mathrm{Tr}[\rho_{\ell-\ell}]$ after the filter
ρ_{1-1}	0.370 ± 0.002	0.556 ± 0.001
ρ_{2-2}	0.319 ± 0.002	0.018 ± 0.001
ρ_{3-3}	0.278 ± 0.002	0.409 ± 0.001

Table 2.1: **The trace of each subspace ρ_ℓ before and after the filter.** This provides the probability to project onto a particular subspace spanned by the states with OAM values $\pm\ell$. The density matrices of the subspaces before and after the filter are show in the supplementary information.

other subspaces (e.g., ρ_{1-2}), but this is only on the order of 2 to 3% combined. This is due to the difficulty in measuring absolutely zero counts; there will almost always be a few background counts or accidentals arriving during a measurement expected to be zero.

2.9 Discussion

We have demonstrated the first HOM interference for high-dimensional entangled photon fields. Our results illustrate the discrimination of the antisymmetric state from the symmetric triplet for high-dimensional entangled states. We analyse the density operator from the output of a HOM filter for OAM modes, which provides direct evidence of state-specific constructive and destructive quantum interference of two photons in a high-dimensionally entangled mode. Specifically, in the anti-symmetric state we observe constructive interference of the components leading to a coincidence signal, while in the symmetric states we observe destructive interference of these components. Our results show effective filtering of the antisymmetric component of a high-dimensional space, demonstrating that HOM interference can be used to engineer the quantum state of OAM-entangled photons. This increases the feasibility of applications of the HOM effect to higher-dimensional OAM qudit states.

Chapter 3

Entanglement Swapping of Orbital Angular Momentum States

3.1 Notes and Acknowledgements

In this chapter, we describe entanglement swapping of the orbital angular momentum state of light. Due to the behaviour of the beamsplitter in high dimensional systems, we achieve simultaneous entanglement swapping in multiple two-dimensional subspaces.

The work in this chapter formed part of a collaboration with colleagues from South Africa. A version of this work has been published in Nature Communications [135]:

Y. Zhang*, M. Agnew*, T. Roger, F.S. Roux, T. Konrad, D. Faccio, J. Leach, A. Forbes, *Simultaneous entanglement swapping of multiple orbital angular momentum states of light*, Nature Communications **8**, 632 (2017).

*These authors contributed equally to this work.

Contributions to this chapter are as follows:

YZ, MA, TR and JL performed the experiment. YZ and MA performed the data analysis. FSR and TK provided the theoretical framework. JL, FSR, AF and DF supervised the project, and the idea was conceived by JL, FSR, AF and TK. MA wrote the first draft of the paper, and all authors contributed to the final version of the manuscript. The text in this thesis was written exclusively by MA.

3.2 Overview

Entanglement swapping generates remote quantum correlations between particles that have not interacted and is the cornerstone of long-distance quantum communication, quantum networks, and fundamental tests of quantum science. The remote creation of high-dimensional entanglement provides an avenue to increase the bandwidth of quantum communications and provides more stringent limits for tests of quantum foundations. Here we simultaneously swap the entanglement of multiple orbital angular momentum states of light. The system is based on a new quantum protocol using a degenerate filter that cannot distinguish between different anti-symmetric states, and thus entanglement swapping occurs for several thousand pairs of spatial light modes simultaneously. We also identify a previously unrealised mechanism that allows high-dimensional entanglement swapping with only four photons, removing the need for scaling photon numbers with dimensions.

3.3 Background

An integral part of a quantum repeater is the ability to entangle two systems that have not interacted – a process referred to as entanglement swapping [25–30,133]. In optics, it is accomplished by interfering two photons via Hong-Ou-Mandel (HOM) interference [88,89,112,115], each from a different entangled pair, in such a way that their remote partners become mutually entangled. This allows the establishment of entanglement between two distant points without requiring single photons to travel the entire distance, thus reducing the effects of decay and loss.

While quantum communication has largely been demonstrated using two-level systems – qubits – to carry information, the use of high-dimensional systems allows more information to be encoded per particle. One way to accomplish this is to encode the information in the orbital angular momentum (OAM) of a photon. It is routinely possible to obtain OAM states entangled in very high dimensions [9,32,92,94,95], and entanglement of OAM is easily produced via spontaneous parametric downconversion (SPDC) [31,136], making OAM an ideal method to increase information capacity [98, 99]. Other high-dimensional systems that could increase information capacity include time bins [39], the path degree of freedom in waveguides [137], and hybrid entanglement [45, 53, 54, 138]. Recently, a number of multi-photon OAM experiments have been reported, including a demonstration of four-photon entanglement [139] and the creation of Greenberger-Horne-Zeilinger states [96]. However, realising entanglement swapping and teleportation in high dimensions has been thought to require increasing the photon number with dimension [131, 132], a prohibitive constraint due to the low count rates associated with many-photon entanglement experiments.

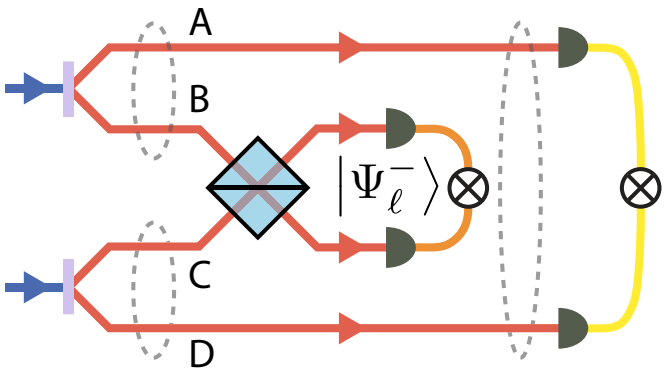

Figure 3.1: **A conceptual diagram of entanglement swapping.** Entanglement between A and B is transferred to A and D via interference at a beamsplitter and detection in coincidence.

In this work, we perform the first implementation of entanglement swapping of spatial states of light. We use photons entangled in the OAM degree of freedom and transfer entanglement from one pair of entangled photons to another, even though the final entangled pair have not interacted with each other. We present results for swapped entanglement in six two-dimensional subspaces. Four of these subspaces did not show entanglement prior to the entanglement swapping. We combine these six subspaces into a four-dimensional mixed state that is representative of the final state in high dimensions. We outline entanglement purification schemes to convert this mixed state into a pure high-dimensional state, allowing scalability of our approach to any dimension without the need for additional ancillary photons, thus providing an approach towards high-dimensional, long-distance secure quantum communication.

3.4 Entanglement Swapping in High Dimensions

We begin with two pairs of entangled photons, each generated from SPDC in a nonlinear crystal. The combined state of the four photons is

$$\begin{aligned}|\psi\rangle_{\mathrm{AB}} &= \sum_\ell c_\ell |\ell\rangle_{\mathrm{A}} |-\ell\rangle_{\mathrm{B}} \otimes \sum_k c_k |k\rangle_{\mathrm{C}} |-k\rangle_{\mathrm{D}} \\ &= \left(c_0 |0\rangle_{\mathrm{A}} |0\rangle_{\mathrm{B}} + \sum_{\ell>0} c_\ell \sqrt{2} |\Psi^+_{\ell-\ell}\rangle_{\mathrm{AB}} \right) \otimes \left(c_0 |0\rangle_{\mathrm{C}} |0\rangle_{\mathrm{D}} + \sum_{k>0} c_k \sqrt{2} |\Psi^+_{k-k}\rangle_{\mathrm{CD}} \right),\end{aligned} \tag{3.1}$$

where for simplicity we assume the probability amplitudes c_ℓ for the two crystals to be identical.

Recall the anti-symmetric state filter from Section 2.4, which we used to filter out anti-symmetric states from a high-dimensionally entangled state. We will use

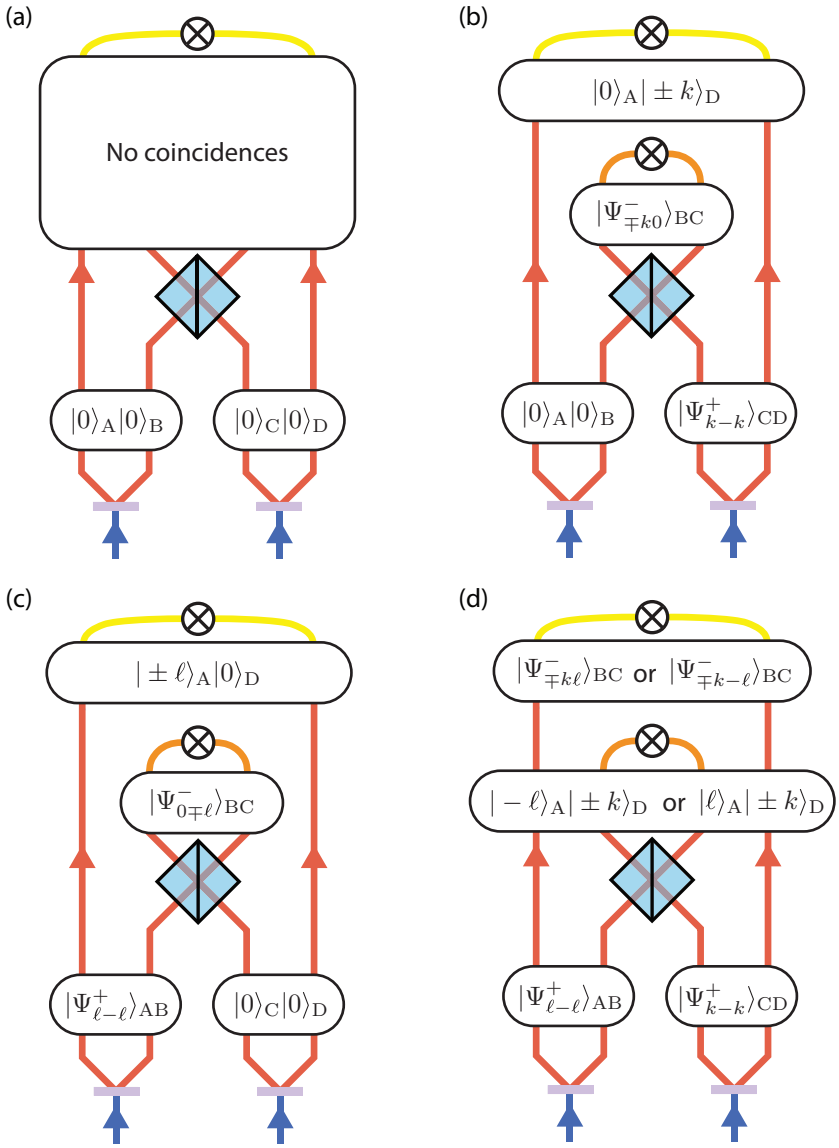

Figure 3.2: **Terms in entanglement swapping calculation from Eq. (3.1).** (a) First term. (b) Second term. (c) Third term. (d) Fourth term.

this filter again here, but this time photons B and C are incident on the two input ports of the filter. Recall the action of the filter

$$\begin{pmatrix} \ell_1^\dagger \\ \ell_2^\dagger \end{pmatrix} = \frac{1}{\sqrt{2}} \begin{pmatrix} 1 & 1 \\ 1 & -1 \end{pmatrix} \begin{pmatrix} \ell_3^\dagger \\ \ell_4^\dagger \end{pmatrix}, \tag{3.2}$$

which can be re-written in terms of the state of photons B and C before and after the filter

$$|\ell\rangle_{\mathrm{B}} \to \frac{1}{\sqrt{2}}\Big(|\ell\rangle_{\mathrm{C}} - |\ell\rangle_{\mathrm{B}}\Big) \tag{3.3}$$

$$|\ell\rangle_{\mathrm{C}} \to \frac{1}{\sqrt{2}}\Big(|\ell\rangle_{\mathrm{C}} + |\ell\rangle_{\mathrm{B}}\Big). \tag{3.4}$$

As the calculation to determine the resultant state $|\psi_{\mathrm{out}}\rangle$ after the beamsplitter is quite involved, we will separate Eq. (3.1) into four terms and look at the action of the beamsplitter on each term individually.

First Term

First and most straightforward is the term with OAM $\ell = 0$ in all four photons

$$\begin{aligned} & c_0|0\rangle_{\mathrm{A}}|0\rangle_{\mathrm{B}} \otimes c_0|0\rangle_{\mathrm{C}}|0\rangle_{\mathrm{D}} \\ \xrightarrow{\text{filter}} & c_0^2|0\rangle_{\mathrm{A}}\left[\frac{1}{\sqrt{2}}\Big(|0\rangle_{\mathrm{C}} - |0\rangle_{\mathrm{B}}\Big)\right]\left[\frac{1}{\sqrt{2}}\Big(|0\rangle_{\mathrm{C}} + |0\rangle_{\mathrm{B}}\Big)\right]|0\rangle_{\mathrm{D}} \\ \xrightarrow{4-\text{ways}} & \mathcal{K}\frac{c_0^2}{2}\Big[|0\rangle_{\mathrm{A}}|0\rangle_{\mathrm{C}}|0\rangle_{\mathrm{B}}|0\rangle_{\mathrm{D}} - |0\rangle_{\mathrm{A}}|0\rangle_{\mathrm{B}}|0\rangle_{\mathrm{C}}|0\rangle_{\mathrm{D}}\Big] \\ & = 0, \end{aligned} \tag{3.5}$$

where we have postselected on the events that produce four-way coincidences (i.e., one photon detection in each of the four paths) and introduced a normalisation factor $\mathcal{K}$ to account for the loss of the other terms. Unsurprisingly, this term produces no four-way coincidences as the OAM values of the interfering photons are identical, meaning that the photons bunch. This scenario is shown in Fig. 3.2(a).

Second Term

Next we examine the case of $\ell = 0$ in photons A and B, with photons C and D taking on any other pair of OAM values:

$$
\begin{aligned}
& c_0|0\rangle_{\mathrm{A}}|0\rangle_{\mathrm{B}} \otimes \sum_{k>0} c_k\sqrt{2}|\Psi^{+}_{k-k}\rangle_{\mathrm{CD}} \\
=\, & c_0|0\rangle_{\mathrm{A}}|0\rangle_{\mathrm{B}} \otimes \sum_{k>0} c_k\Big(|k\rangle_{\mathrm{C}}|-k\rangle_{\mathrm{D}} + |-k\rangle_{\mathrm{C}}|k\rangle_{\mathrm{D}}\Big) \\
\xrightarrow{\text{filter}}\, & c_0|0\rangle_{\mathrm{A}}\frac{1}{\sqrt{2}}\Big(|0\rangle_{\mathrm{C}} - |0\rangle_{\mathrm{B}}\Big) \\
& \qquad \otimes \sum_{k>0} c_k\left[\frac{1}{\sqrt{2}}\Big(|k\rangle_{\mathrm{C}} + |k\rangle_{\mathrm{B}}\Big)|-k\rangle_{\mathrm{D}} + \frac{1}{\sqrt{2}}\Big(|-k\rangle_{\mathrm{C}} + |-k\rangle_{\mathrm{B}}\Big)|k\rangle_{\mathrm{D}}\right] \\
=\, & \sum_{k>0}\frac{c_0c_k}{2}\Bigg[|0\rangle_{\mathrm{A}}|0\rangle_{\mathrm{C}}\Big(|k\rangle_{\mathrm{C}} + |k\rangle_{\mathrm{B}}\Big)|-k\rangle_{\mathrm{D}} - |0\rangle_{\mathrm{A}}|0\rangle_{\mathrm{B}}\Big(|k\rangle_{\mathrm{C}} + |k\rangle_{\mathrm{B}}\Big)|-k\rangle_{\mathrm{D}} \\
& \qquad + |0\rangle_{\mathrm{A}}|0\rangle_{\mathrm{C}}\Big(|-k\rangle_{\mathrm{C}} + |-k\rangle_{\mathrm{B}}\Big)|k\rangle_{\mathrm{D}} - |0\rangle_{\mathrm{A}}|0\rangle_{\mathrm{B}}\Big(|-k\rangle_{\mathrm{C}} + |-k\rangle_{\mathrm{B}}\Big)|k\rangle_{\mathrm{D}}\Bigg] \\
\xrightarrow{4-\text{ways}}\, & \mathcal{K}\sum_{k>0}\frac{c_0c_k}{2}\Bigg[|0\rangle_{\mathrm{A}}|0\rangle_{\mathrm{C}}|k\rangle_{\mathrm{B}}|-k\rangle_{\mathrm{D}} - |0\rangle_{\mathrm{A}}|0\rangle_{\mathrm{B}}|k\rangle_{\mathrm{C}}|-k\rangle_{\mathrm{D}} \\
& \qquad + |0\rangle_{\mathrm{A}}|0\rangle_{\mathrm{C}}|-k\rangle_{\mathrm{B}}|k\rangle_{\mathrm{D}} - |0\rangle_{\mathrm{A}}|0\rangle_{\mathrm{B}}|-k\rangle_{\mathrm{C}}|k\rangle_{\mathrm{D}}\Bigg] \\
=\, & \mathcal{K}\sum_{k>0}\frac{c_0c_k}{2}\Bigg[|0\rangle_{\mathrm{A}}|-k\rangle_{\mathrm{D}}\Big(|0\rangle_{\mathrm{C}}|k\rangle_{\mathrm{B}} - |0\rangle_{\mathrm{B}}|k\rangle_{\mathrm{C}}\Big) \\
& \qquad + |0\rangle_{\mathrm{A}}|k\rangle_{\mathrm{D}}\Big(|0\rangle_{\mathrm{C}}|-k\rangle_{\mathrm{B}} - |0\rangle_{\mathrm{B}}|-k\rangle_{\mathrm{C}}\Big)\Bigg] \\
=\, & \mathcal{K}\sum_{k>0}\frac{c_0c_k}{\sqrt{2}}\Big(|0\rangle_{\mathrm{A}}|-k\rangle_{\mathrm{D}}|\Psi^{-}_{k0}\rangle_{\mathrm{BC}} + |0\rangle_{\mathrm{A}}|k\rangle_{\mathrm{D}}|\Psi^{-}_{-k0}\rangle_{\mathrm{BC}}\Big). \qquad (3.6)
\end{aligned}
$$

From this term, we obtain photons A and D in the state $|0\rangle_{\mathrm{A}}|\pm k\rangle_{\mathrm{D}}$ and photons B and C correspondingly in the state $|\Psi^{-}_{\mp k0}\rangle_{\mathrm{BC}}$. This scenario is shown in Fig. 3.2(b).

Third Term

Similarly, for the case of $\ell = 0$ in photons C and D, with photons A and B taking on any other pair of OAM values, we obtain

$$
\begin{aligned}
&\sum_{\ell>0} c_\ell \sqrt{2} |\Psi^+_{\ell -\ell}\rangle_{\mathrm{AB}} \otimes c_0 |0\rangle_{\mathrm{C}} |0\rangle_{\mathrm{D}} \\
&= \sum_{\ell>0} c_\ell \Big(|\ell\rangle_{\mathrm{A}} |-\ell\rangle_{\mathrm{B}} + |-\ell\rangle_{\mathrm{A}} |\ell\rangle_{\mathrm{B}} \Big) \otimes c_0 |0\rangle_{\mathrm{C}} |0\rangle_{\mathrm{D}} \\
\xrightarrow{\text{filter}} &\sum_{\ell>0} c_\ell \left[|\ell\rangle_{\mathrm{A}} \frac{1}{\sqrt{2}} \Big(|-\ell\rangle_{\mathrm{C}} - |-\ell\rangle_{\mathrm{B}} \Big) + |-\ell\rangle_{\mathrm{A}} \frac{1}{\sqrt{2}} \Big(|\ell\rangle_{\mathrm{C}} - |\ell\rangle_{\mathrm{B}} \Big) \right] \\
&\qquad \otimes c_0 \frac{1}{\sqrt{2}} \Big(|0\rangle_{\mathrm{C}} + |0\rangle_{\mathrm{B}} \Big) |0\rangle_{\mathrm{D}} \\
&= \sum_{\ell>0} \frac{c_0 c_\ell}{2} \Big[|\ell\rangle_{\mathrm{A}} \Big(|-\ell\rangle_{\mathrm{C}} - |-\ell\rangle_{\mathrm{B}} \Big) |0\rangle_{\mathrm{C}} |0\rangle_{\mathrm{D}} + |\ell\rangle_{\mathrm{A}} \Big(|-\ell\rangle_{\mathrm{C}} - |-\ell\rangle_{\mathrm{B}} \Big) |0\rangle_{\mathrm{B}} |0\rangle_{\mathrm{D}} \\
&\qquad + |-\ell\rangle_{\mathrm{A}} \Big(|\ell\rangle_{\mathrm{C}} - |\ell\rangle_{\mathrm{B}} \Big) |0\rangle_{\mathrm{C}} |0\rangle_{\mathrm{D}} + |-\ell\rangle_{\mathrm{A}} \Big(|\ell\rangle_{\mathrm{C}} - |\ell\rangle_{\mathrm{B}} \Big) |0\rangle_{\mathrm{B}} |0\rangle_{\mathrm{D}} \Big] \\
\xrightarrow{4-\text{ways}} &\mathcal{K} \sum_{\ell>0} \frac{c_0 c_\ell}{2} \Big[- |\ell\rangle_{\mathrm{A}} |-\ell\rangle_{\mathrm{B}} |0\rangle_{\mathrm{C}} |0\rangle_{\mathrm{D}} + |\ell\rangle_{\mathrm{A}} |-\ell\rangle_{\mathrm{C}} |0\rangle_{\mathrm{B}} |0\rangle_{\mathrm{D}} \\
&\qquad - |-\ell\rangle_{\mathrm{A}} |\ell\rangle_{\mathrm{B}} |0\rangle_{\mathrm{C}} |0\rangle_{\mathrm{D}} + |-\ell\rangle_{\mathrm{A}} |\ell\rangle_{\mathrm{C}} |0\rangle_{\mathrm{B}} |0\rangle_{\mathrm{D}} \Big] \\
&= \mathcal{K} \sum_{\ell>0} \frac{c_0 c_\ell}{2} \Big[|\ell\rangle_{\mathrm{A}} |0\rangle_{\mathrm{D}} \Big(|-\ell\rangle_{\mathrm{C}} |0\rangle_{\mathrm{B}} - |-\ell\rangle_{\mathrm{B}} |0\rangle_{\mathrm{C}} \Big) \\
&\qquad + |-\ell\rangle_{\mathrm{A}} |0\rangle_{\mathrm{D}} \Big(|\ell\rangle_{\mathrm{C}} |0\rangle_{\mathrm{B}} - |\ell\rangle_{\mathrm{B}} |0\rangle_{\mathrm{C}} \Big) \Big] \\
&= \mathcal{K} \sum_{\ell>0} \frac{c_0 c_\ell}{\sqrt{2}} \Big(|\ell\rangle_{\mathrm{A}} |0\rangle_{\mathrm{D}} |\Psi^-_{0-\ell}\rangle_{\mathrm{BC}} + |-\ell\rangle_{\mathrm{A}} |0\rangle_{\mathrm{D}} |\Psi^-_{0\ell}\rangle_{\mathrm{BC}} \Big). \qquad (3.7)
\end{aligned}
$$

From this term, we obtain photons A and D in the state $|\pm\ell\rangle_{\mathrm{A}} |0\rangle_{\mathrm{D}}$ and photons B and C correspondingly in the state $|\Psi^-_{0\mp\ell}\rangle_{\mathrm{BC}}$. This scenario is shown in Fig. 3.2(c).

Simplification of First Three Terms

We can simplify the first three terms by using the fact that $|\Psi^-_{ab}\rangle = -|\Psi^-_{ba}\rangle$. Taking the sum of Eqs. (3.5–3.7), we obtain

$$\begin{aligned}
&\mathcal{K}\sum_{k>0}\frac{c_0c_k}{\sqrt{2}}\Big(|0\rangle_{\rm A}|-k\rangle_{\rm D}|\Psi^-_{k0}\rangle_{\rm BC}+|0\rangle_{\rm A}|k\rangle_{\rm D}|\Psi^-_{-k0}\rangle_{\rm BC}\Big)\\
&\qquad+\mathcal{K}\sum_{\ell>0}\frac{c_0c_\ell}{\sqrt{2}}\Big(|\ell\rangle_{\rm A}|0\rangle_{\rm D}|\Psi^-_{0-\ell}\rangle_{\rm BC}+|-\ell\rangle_{\rm A}|0\rangle_{\rm D}|\Psi^-_{0\ell}\rangle_{\rm BC}\Big)\\
=&\,\mathcal{K}\sum_{\ell>0}\frac{c_0c_\ell}{\sqrt{2}}\Big(|0\rangle_{\rm A}|-\ell\rangle_{\rm D}|\Psi^-_{\ell0}\rangle_{\rm BC}+|0\rangle_{\rm A}|\ell\rangle_{\rm D}|\Psi^-_{-\ell0}\rangle_{\rm BC}\Big)\\
&\qquad-\mathcal{K}\sum_{\ell>0}\frac{c_0c_\ell}{\sqrt{2}}\Big(|\ell\rangle_{\rm A}|0\rangle_{\rm D}|\Psi^-_{-\ell0}\rangle_{\rm BC}+|-\ell\rangle_{\rm A}|0\rangle_{\rm D}|\Psi^-_{\ell0}\rangle_{\rm BC}\Big)\\
=&\,\mathcal{K}\sum_{\ell>0}c_0c_\ell\Big(|\Psi^-_{0-\ell}\rangle_{\rm AD}|\Psi^-_{\ell0}\rangle_{\rm BC}+|\Psi^-_{0\ell}\rangle_{\rm AD}|\Psi^-_{-\ell0}\rangle_{\rm BC}\Big).
\end{aligned}\tag{3.8}$$

Thus considering the first three terms of the state in Eq. (3.1) passing through our anti-symmetric filter, we obtain photons A and D in the state $|\Psi^-_{0\pm\ell}\rangle_{\rm AD}$ and photons B and C correspondingly in the state $|\Psi^-_{\mp\ell0}\rangle_{\rm BC}$.

Fourth Term

Finally, the fourth term consists of any non-zero OAM value in either pair of photons:

$$
\begin{aligned}
&\sum_{\ell>0} c_\ell\sqrt{2}|\Psi^+_{\ell-\ell}\rangle_{\mathrm{AB}} \otimes \sum_{k>0} c_k\sqrt{2}|\Psi^+_{k-k}\rangle_{\mathrm{CD}} \\
&= \sum_{\ell>0}\sum_{k>0} c_\ell c_k \Big(|\ell\rangle_{\mathrm{A}}|-\ell\rangle_{\mathrm{B}} + |-\ell\rangle_{\mathrm{A}}|\ell\rangle_{\mathrm{B}}\Big) \otimes \Big(|k\rangle_{\mathrm{C}}|-k\rangle_{\mathrm{D}} + |-k\rangle_{\mathrm{C}}|k\rangle_{\mathrm{D}}\Big) \\
&\xrightarrow{\text{filter}} \sum_{\ell>0}\sum_{k>0} c_\ell c_k \left[|\ell\rangle_{\mathrm{A}}\frac{1}{\sqrt{2}}\Big(|-\ell\rangle_{\mathrm{C}} - |-\ell\rangle_{\mathrm{B}}\Big) + |-\ell\rangle_{\mathrm{A}}\frac{1}{\sqrt{2}}\Big(|\ell\rangle_{\mathrm{C}} - |\ell\rangle_{\mathrm{B}}\Big)\right] \\
&\qquad \otimes \left[\frac{1}{\sqrt{2}}\Big(|k\rangle_{\mathrm{C}} + |k\rangle_{\mathrm{B}}\Big)|-k\rangle_{\mathrm{D}} + \frac{1}{\sqrt{2}}\Big(|-k\rangle_{\mathrm{C}} + |-k\rangle_{\mathrm{B}}\Big)|k\rangle_{\mathrm{D}}\right] \\
&= \sum_{\ell>0}\sum_{k>0} \frac{c_\ell c_k}{2}\Big(|\ell\rangle_{\mathrm{A}}|-\ell\rangle_{\mathrm{C}} - |\ell\rangle_{\mathrm{A}}|-\ell\rangle_{\mathrm{B}} + |-\ell\rangle_{\mathrm{A}}|\ell\rangle_{\mathrm{C}} - |-\ell\rangle_{\mathrm{A}}|\ell\rangle_{\mathrm{B}}\Big) \\
&\qquad \otimes \Big(|k\rangle_{\mathrm{C}}|-k\rangle_{\mathrm{D}} + |k\rangle_{\mathrm{B}}|-k\rangle_{\mathrm{D}} + |-k\rangle_{\mathrm{C}}|k\rangle_{\mathrm{D}} + |-k\rangle_{\mathrm{B}}|k\rangle_{\mathrm{D}}\Big) \\
&\xrightarrow{4-\text{ways}} \mathcal{K}\sum_{\ell>0}\sum_{k>0} \frac{c_\ell c_k}{2}\Big(|\ell\rangle_{\mathrm{A}}|-\ell\rangle_{\mathrm{C}}|k\rangle_{\mathrm{B}}|-k\rangle_{\mathrm{D}} + |\ell\rangle_{\mathrm{A}}|-\ell\rangle_{\mathrm{C}}|-k\rangle_{\mathrm{B}}|k\rangle_{\mathrm{D}} \\
&\qquad\qquad - |\ell\rangle_{\mathrm{A}}|-\ell\rangle_{\mathrm{B}}|k\rangle_{\mathrm{C}}|-k\rangle_{\mathrm{D}} - |\ell\rangle_{\mathrm{A}}|-\ell\rangle_{\mathrm{B}}|-k\rangle_{\mathrm{C}}|k\rangle_{\mathrm{D}} \\
&\qquad\qquad + |-\ell\rangle_{\mathrm{A}}|\ell\rangle_{\mathrm{C}}|k\rangle_{\mathrm{B}}|-k\rangle_{\mathrm{D}} + |-\ell\rangle_{\mathrm{A}}|\ell\rangle_{\mathrm{C}}|-k\rangle_{\mathrm{B}}|k\rangle_{\mathrm{D}} \\
&\qquad\qquad - |-\ell\rangle_{\mathrm{A}}|\ell\rangle_{\mathrm{B}}|k\rangle_{\mathrm{C}}|-k\rangle_{\mathrm{D}} - |-\ell\rangle_{\mathrm{A}}|\ell\rangle_{\mathrm{B}}|-k\rangle_{\mathrm{C}}|k\rangle_{\mathrm{D}}\Big) \\
&= \mathcal{K}\sum_{\ell>0}\sum_{k>0} \frac{c_\ell c_k}{2}\Big[|\ell\rangle_{\mathrm{A}}|-k\rangle_{\mathrm{D}}\Big(|-\ell\rangle_{\mathrm{C}}|k\rangle_{\mathrm{B}} - |-\ell\rangle_{\mathrm{B}}|k\rangle_{\mathrm{C}}\Big) \\
&\qquad\qquad + |\ell\rangle_{\mathrm{A}}|k\rangle_{\mathrm{D}}\Big(|-\ell\rangle_{\mathrm{C}}|-k\rangle_{\mathrm{B}} - |-\ell\rangle_{\mathrm{B}}|-k\rangle_{\mathrm{C}}\Big) \\
&\qquad\qquad + |-\ell\rangle_{\mathrm{A}}|-k\rangle_{\mathrm{D}}\Big(|\ell\rangle_{\mathrm{C}}|k\rangle_{\mathrm{B}} - |\ell\rangle_{\mathrm{B}}|k\rangle_{\mathrm{C}}\Big) \\
&\qquad\qquad + |-\ell\rangle_{\mathrm{A}}|k\rangle_{\mathrm{D}}\Big(|\ell\rangle_{\mathrm{C}}|-k\rangle_{\mathrm{B}} - |\ell\rangle_{\mathrm{B}}|-k\rangle_{\mathrm{C}}\Big)\Big] \\
&= \mathcal{K}\sum_{\ell>0}\sum_{k>0} \frac{c_\ell c_k}{\sqrt{2}}\Big(|\ell\rangle_{\mathrm{A}}|-k\rangle_{\mathrm{D}}|\Psi^-_{k-\ell}\rangle_{\mathrm{BC}} + |\ell\rangle_{\mathrm{A}}|k\rangle_{\mathrm{D}}|\Psi^-_{-k-\ell}\rangle_{\mathrm{BC}} \\
&\qquad\qquad + |-\ell\rangle_{\mathrm{A}}|-k\rangle_{\mathrm{D}}|\Psi^-_{k\ell}\rangle_{\mathrm{BC}} + |-\ell\rangle_{\mathrm{A}}|k\rangle_{\mathrm{D}}|\Psi^-_{-k\ell}\rangle_{\mathrm{BC}}\Big). \qquad (3.9)
\end{aligned}
$$

From this term, we obtain either photons A and D in the state $|\ell\rangle_{\mathrm{A}}|\pm k\rangle_{\mathrm{D}}$ and photons B and C correspondingly in the state $|\Psi^-_{\mp k-\ell}\rangle_{\mathrm{BC}}$, or photons A and D in the state $|-\ell\rangle_{\mathrm{A}}|\pm k\rangle_{\mathrm{D}}$ and photons B and C correspondingly in the state $|\Psi^-_{\mp k\ell}\rangle_{\mathrm{BC}}$. This scenario is shown in Fig. 3.2(d).

Simplification of Fourth Term

To simplify the above expression, we examine three cases of Eq. (3.9). First, we assume $\ell = k$ to obtain

$$\begin{aligned}
&\mathcal{K}\sum_{k>0}\frac{c_k^2}{\sqrt{2}}\Big(|k\rangle_{\rm A}|-k\rangle_{\rm D}|\Psi^-_{k-k}\rangle_{\rm BC}+|k\rangle_{\rm A}|k\rangle_{\rm D}|\Psi^-_{-k-k}\rangle_{\rm BC}\\
&\qquad\qquad+|-k\rangle_{\rm A}|-k\rangle_{\rm D}|\Psi^-_{kk}\rangle_{\rm BC}+|-k\rangle_{\rm A}|k\rangle_{\rm D}|\Psi^-_{-kk}\rangle_{\rm BC}\Big)\\
=&\mathcal{K}\sum_{k>0}\frac{c_k^2}{\sqrt{2}}\Big(|k\rangle_{\rm A}|-k\rangle_{\rm D}|\Psi^-_{k-k}\rangle_{\rm BC}+|-k\rangle_{\rm A}|k\rangle_{\rm D}|\Psi^-_{-kk}\rangle_{\rm BC},\Big)
\end{aligned}\tag{3.10}$$

since $|\Psi^-_{kk}\rangle = 0$.

Next, we assume $\ell \neq k$, $\ell = n$, $k = m$, $n > m$ to obtain

$$\begin{aligned}
&\mathcal{K}\sum_{n>m}\sum_{m>0}\frac{c_nc_m}{\sqrt{2}}\Big(|n\rangle_{\rm A}|-m\rangle_{\rm D}|\Psi^-_{m-n}\rangle_{\rm BC}+|n\rangle_{\rm A}|m\rangle_{\rm D}|\Psi^-_{-m-n}\rangle_{\rm BC}\\
&\qquad\qquad+|-n\rangle_{\rm A}|-m\rangle_{\rm D}|\Psi^-_{mn}\rangle_{\rm BC}+|-n\rangle_{\rm A}|m\rangle_{\rm D}|\Psi^-_{-mn}\rangle_{\rm BC}\Big).
\end{aligned}\tag{3.11}$$

Similarly, with $\ell \neq k$, $\ell = m$, $k = n$, $n > m$, we obtain

$$\begin{aligned}
&\mathcal{K}\sum_{m>0}\sum_{n>m}\frac{c_mc_n}{\sqrt{2}}\Big(|m\rangle_{\rm A}|-n\rangle_{\rm D}|\Psi^-_{n-m}\rangle_{\rm BC}+|m\rangle_{\rm A}|n\rangle_{\rm D}|\Psi^-_{-n-m}\rangle_{\rm BC}\\
&\qquad\qquad+|-m\rangle_{\rm A}|-n\rangle_{\rm D}|\Psi^-_{nm}\rangle_{\rm BC}+|-m\rangle_{\rm A}|n\rangle_{\rm D}|\Psi^-_{-nm}\rangle_{\rm BC}\Big).
\end{aligned}\tag{3.12}$$

Again, we can simplify the above equations by using the fact that $|\Psi^-_{ab}\rangle = -|\Psi^-_{ab}\rangle$.

Taking the sum of Eqs. (3.10–3.12), we obtain

$$
\begin{aligned}
&\mathcal{K}\sum_{k>0}\frac{c_k^2}{\sqrt{2}}\Big(|k\rangle_{\mathrm{A}}|-k\rangle_{\mathrm{D}}|\Psi^-_{k-k}\rangle_{\mathrm{BC}}+|-k\rangle_{\mathrm{A}}|k\rangle_{\mathrm{D}}|\Psi^-_{-kk}\rangle_{\mathrm{BC}}\Big)\\
&\quad+\mathcal{K}\sum_{n>m}\sum_{m>0}\frac{c_nc_m}{\sqrt{2}}\Big(|n\rangle_{\mathrm{A}}|-m\rangle_{\mathrm{D}}|\Psi^-_{m-n}\rangle_{\mathrm{BC}}+|n\rangle_{\mathrm{A}}|m\rangle_{\mathrm{D}}|\Psi^-_{-m-n}\rangle_{\mathrm{BC}}\\
&\qquad\quad+|-n\rangle_{\mathrm{A}}|-m\rangle_{\mathrm{D}}|\Psi^-_{mn}\rangle_{\mathrm{BC}}+|-n\rangle_{\mathrm{A}}|m\rangle_{\mathrm{D}}|\Psi^-_{-mn}\rangle_{\mathrm{BC}}\Big)\\
&\quad+\mathcal{K}\sum_{m>0}\sum_{n>m}\frac{c_mc_n}{\sqrt{2}}\Big(|m\rangle_{\mathrm{A}}|-n\rangle_{\mathrm{D}}|\Psi^-_{n-m}\rangle_{\mathrm{BC}}+|m\rangle_{\mathrm{A}}|n\rangle_{\mathrm{D}}|\Psi^-_{-n-m}\rangle_{\mathrm{BC}}\\
&\qquad\quad+|-m\rangle_{\mathrm{A}}|-n\rangle_{\mathrm{D}}|\Psi^-_{nm}\rangle_{\mathrm{BC}}+|-m\rangle_{\mathrm{A}}|n\rangle_{\mathrm{D}}|\Psi^-_{-nm}\rangle_{\mathrm{BC}}\Big)\\
=&\,\mathcal{K}\sum_{k>0}\frac{c_k^2}{\sqrt{2}}\Big(|k\rangle_{\mathrm{A}}|-k\rangle_{\mathrm{D}}|\Psi^-_{k-k}\rangle_{\mathrm{BC}}-|-k\rangle_{\mathrm{A}}|k\rangle_{\mathrm{D}}|\Psi^-_{k-k}\rangle_{\mathrm{BC}}\Big)\\
&\quad+\mathcal{K}\sum_{n>m}\sum_{m>0}\frac{c_nc_m}{\sqrt{2}}\Big(|n\rangle_{\mathrm{A}}|-m\rangle_{\mathrm{D}}|\Psi^-_{m-n}\rangle_{\mathrm{BC}}+|n\rangle_{\mathrm{A}}|m\rangle_{\mathrm{D}}|\Psi^-_{-m-n}\rangle_{\mathrm{BC}}\\
&\qquad\quad+|-n\rangle_{\mathrm{A}}|-m\rangle_{\mathrm{D}}|\Psi^-_{mn}\rangle_{\mathrm{BC}}+|-n\rangle_{\mathrm{A}}|m\rangle_{\mathrm{D}}|\Psi^-_{-mn}\rangle_{\mathrm{BC}}\Big)\\
&\quad-\mathcal{K}\sum_{n>m}\sum_{m>0}\frac{c_nc_m}{\sqrt{2}}\Big(|m\rangle_{\mathrm{A}}|-n\rangle_{\mathrm{D}}|\Psi^-_{-mn}\rangle_{\mathrm{BC}}+|m\rangle_{\mathrm{A}}|n\rangle_{\mathrm{D}}|\Psi^-_{-m-n}\rangle_{\mathrm{BC}}\\
&\qquad\quad+|-m\rangle_{\mathrm{A}}|-n\rangle_{\mathrm{D}}|\Psi^-_{mn}\rangle_{\mathrm{BC}}+|-m\rangle_{\mathrm{A}}|n\rangle_{\mathrm{D}}|\Psi^-_{m-n}\rangle_{\mathrm{BC}}\Big)\\
=&\,\mathcal{K}\sum_{k>0}c_k^2|\Psi^-_{k-k}\rangle_{\mathrm{AD}}|\Psi^-_{k-k}\rangle_{\mathrm{BC}}\\
&\quad+\mathcal{K}\sum_{n>m}\sum_{m>0}c_nc_m\Big(|\Psi^-_{n-m}\rangle_{\mathrm{AD}}|\Psi^-_{m-n}\rangle_{\mathrm{BC}}+|\Psi^-_{nm}\rangle_{\mathrm{AD}}|\Psi^-_{-m-n}\rangle_{\mathrm{BC}}\\
&\qquad\quad+|\Psi^-_{-n-m}\rangle_{\mathrm{AD}}|\Psi^-_{mn}\rangle_{\mathrm{BC}}+|\Psi^-_{-nm}\rangle_{\mathrm{AD}}|\Psi^-_{-mn}\rangle_{\mathrm{BC}}\Big).
\end{aligned}
\tag{3.13}
$$

Final State

Combining Eqs. (3.8) and (3.13), we obtain the final expression for a high-dimensionally entangled OAM state after passing through the anti-symmetric filter:

$$
\begin{aligned}
|\psi_{\mathrm{out}}\rangle=&\,\mathcal{K}\sum_{\ell>0}c_0c_\ell\Big(|\Psi^-_{0-\ell}\rangle_{\mathrm{AD}}|\Psi^-_{\ell0}\rangle_{\mathrm{BC}}+|\Psi^-_{0\ell}\rangle_{\mathrm{AD}}|\Psi^-_{-\ell0}\rangle_{\mathrm{BC}}\Big)+\mathcal{K}\sum_{k>0}c_k^2|\Psi^-_{k-k}\rangle_{\mathrm{AD}}|\Psi^-_{k-k}\rangle_{\mathrm{BC}}\\
&\quad+\mathcal{K}\sum_{n>m}\sum_{m>0}c_nc_m\Big(|\Psi^-_{n-m}\rangle_{\mathrm{AD}}|\Psi^-_{m-n}\rangle_{\mathrm{BC}}+|\Psi^-_{nm}\rangle_{\mathrm{AD}}|\Psi^-_{-m-n}\rangle_{\mathrm{BC}}\\
&\qquad\quad+|\Psi^-_{-n-m}\rangle_{\mathrm{AD}}|\Psi^-_{mn}\rangle_{\mathrm{BC}}+|\Psi^-_{-nm}\rangle_{\mathrm{AD}}|\Psi^-_{-mn}\rangle_{\mathrm{BC}}\Big)\\
=&\,\mathcal{K}\sum_{\ell>0}\Big[c_0c_\ell\Big(|\Psi^-_{0-\ell}\rangle_{\mathrm{AD}}|\Psi^-_{\ell0}\rangle_{\mathrm{BC}}+|\Psi^-_{0\ell}\rangle_{\mathrm{AD}}|\Psi^-_{-\ell0}\rangle_{\mathrm{BC}}\Big)+c_\ell^2|\Psi^-_{\ell-\ell}\rangle_{\mathrm{AD}}|\Psi^-_{\ell-\ell}\rangle_{\mathrm{BC}}\Big]\\
&\quad+\mathcal{K}\sum_{\ell>k}\sum_{k>0}c_\ell c_k\Big(|\Psi^-_{\ell-k}\rangle_{\mathrm{AD}}|\Psi^-_{k-\ell}\rangle_{\mathrm{BC}}+|\Psi^-_{\ell k}\rangle_{\mathrm{AD}}|\Psi^-_{-k-\ell}\rangle_{\mathrm{BC}}\\
&\qquad\quad+|\Psi^-_{-\ell-k}\rangle_{\mathrm{AD}}|\Psi^-_{k\ell}\rangle_{\mathrm{BC}}+|\Psi^-_{-\ell k}\rangle_{\mathrm{AD}}|\Psi^-_{-k\ell}\rangle_{\mathrm{BC}}\Big).
\end{aligned}
\tag{3.14}
$$

Essentially, passing the state in Eq. (3.1) through our anti-symmetric filter, we obtain photons A and D in the state $|\Psi^-_{\ell k}\rangle_{\mathrm{AD}}$ and photons B and C correspondingly

in the state $|\Psi^-_{-k-\ell}\rangle_{\mathrm{BC}}$, for all unique combinations of OAM values ℓ and k.

As we are interested in observing entanglement swapping, which is evidenced by an entangled state between photons A and D, we trace out photons B and C to obtain the state of photons A and D. For convenience, we use the Bell basis to perform the partial trace

$$\rho_{\mathrm{AD}} = \sum_m \sum_n \sum_{i=1}^{4} \langle \phi^{(i)}_{mn}|_{\mathrm{BC}} \Big(|\psi_{\mathrm{out}}\rangle\langle\psi_{\mathrm{out}}| \Big) |\phi^{(i)}_{mn}\rangle_{\mathrm{BC}}, \tag{3.15}$$

where $|\phi\rangle^{(i)}_{mn} \in \{|\Phi^+_{mn}\rangle, |\Phi^-_{mn}\rangle, |\Psi^+_{mn}\rangle, |\Psi^-_{mn}\rangle\}$. As all terms in Eq. (3.14) are antisymmetric, they are orthogonal to $|\Phi^+_{mn}\rangle$, $|\Phi^-_{mn}\rangle$, and $|\Psi^+_{mn}\rangle$; thus the above equation can be simplified to

$$\rho_{\mathrm{AD}} = \sum_m \sum_n \langle \Psi^-_{mn}|_{\mathrm{BC}} \Big(|\psi_{\mathrm{out}}\rangle\langle\psi_{\mathrm{out}}| \Big) |\Psi^-_{mn}\rangle_{\mathrm{BC}}. \tag{3.16}$$

The inner product of two anti-symmetric states is

$$\begin{aligned}
\langle \Psi^-_{mn}|\Psi^-_{\ell k}\rangle &= \frac{1}{\sqrt{2}}\big(\langle m|\langle n| - \langle n|\langle m|\big)\frac{1}{\sqrt{2}}\big(|\ell\rangle|k\rangle - |k\rangle|\ell\rangle\big) \\
&= \frac{1}{2}\big(\langle m|\ell\rangle\langle n|k\rangle - \langle m|k\rangle\langle n|\ell\rangle - \langle n|\ell\rangle\langle m|k\rangle + \langle n|k\rangle\langle m|\ell\rangle\big) \\
&= \langle m|\ell\rangle\langle n|k\rangle - \langle m|k\rangle\langle n|\ell\rangle \\
&= \delta_{m\ell}\delta_{nk} - \delta_{mk}\delta_{n\ell} \\
&= \begin{cases} 1, & \text{for } m = \ell \text{ and } n = k \\ -1, & \text{for } m = k \text{ and } n = \ell \\ 0, & \text{otherwise.} \end{cases}
\end{aligned} \tag{3.17}$$

Applying this to the partial trace, we obtain the final state of photons A and D

$$\begin{aligned}
\rho_{\mathrm{AD}} = |\mathcal{K}|^2 \sum_{\ell>0} \Bigg[& |c_0|^2|c_\ell|^2 \Big(|\Psi^-_{0-\ell}\rangle_{\mathrm{AD}}\langle\Psi^-_{0-\ell}|_{\mathrm{AD}} + |\Psi^-_{0\ell}\rangle_{\mathrm{AD}}\langle\Psi^-_{0\ell}|_{\mathrm{AD}} \Big) \\
& + |c_\ell|^4 |\Psi^-_{\ell-\ell}\rangle_{\mathrm{AD}}\langle\Psi^-_{\ell-\ell}|_{\mathrm{AD}} \Bigg] \\
+ |\mathcal{K}|^2 \sum_{\ell>k} \sum_{k>0} & |c_\ell|^2|c_k|^2 \Big(|\Psi^-_{\ell-k}\rangle_{\mathrm{AD}}\langle\Psi^-_{\ell-k}|_{\mathrm{AD}} + |\Psi^-_{\ell k}\rangle_{\mathrm{AD}}\langle\Psi^-_{\ell k}|_{\mathrm{AD}} \\
& + |\Psi^-_{-\ell-k}\rangle_{\mathrm{AD}}\langle\Psi^-_{-\ell-k}|_{\mathrm{AD}} + |\Psi^-_{-\ell k}\rangle_{\mathrm{AD}}\langle\Psi^-_{-\ell k}|_{\mathrm{AD}} \Big).
\end{aligned} \tag{3.18}$$

This state is a statistical mixture of all possible two-dimensional anti-symmetric Bell states. For a d-dimensional OAM space, the number of two-dimensional subspaces for which an anti-symmetric Bell state exists is equal to the binomial coefficient $\binom{d}{2}$.

Note that the above state contains entanglement between photons A and D, which did not exist before the anti-symmetric state filter; however, it consists of two-dimensional entanglement in many different subspaces. This is in contrast to

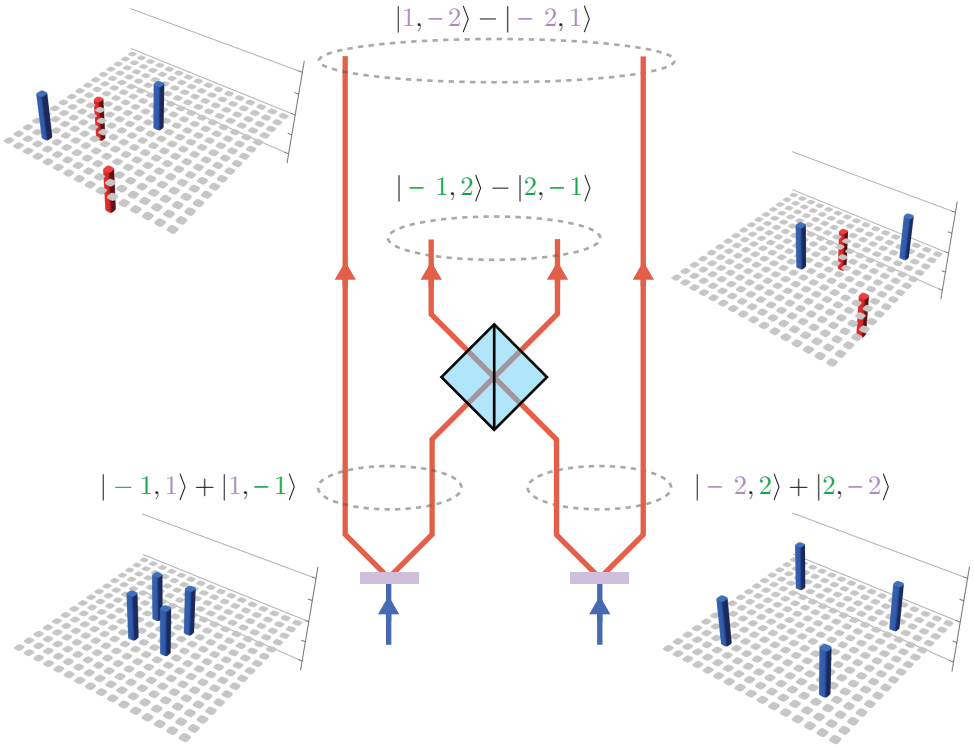

Figure 3.3: **Transcription of entanglement.** We start with the entangled states $|\Psi^+_{-11}\rangle_{\mathrm{AB}}$ and $|\Psi^+_{-22}\rangle_{\mathrm{CD}}$. After the beamsplitter and projection onto the appropriate anti-symmetric state $|\Psi^-_{-12}\rangle$, the state between photons A and D is $|\Psi^-_{-21}\rangle_{\mathrm{AD}}$. The OAM values shown in green become the OAM values in the state projected onto B and C. The OAM values shown in purple become the OAM values in the state between photons A and D. States are shown without normalisation for clarity. The density matrices show the corresponding maximally entangled states.

the expected result from true high-dimensional entanglement swapping, in which we would obtain the exact same state in photons A and D that we originally had in photons A and B.

Indeed, entanglement between the majority of these subspaces did not exist at all in the original entanglement between photons A and B or C and D. For example, it is not possible to obtain an entangled state in the $\ell = 1, -2$ subspace via downconversion from a Gaussian mode. This is because orbital angular momentum must be conserved in the process that produces entanglement; the OAM of all the entangled subspaces must sum to zero (the input Gaussian mode). However, due to the interference in our anti-symmetric state filter, the entanglement in the $\ell = \pm 1$ and $\ell = \pm 2$ subspaces is transferred into the $\ell = -1, 2$ and $\ell = 1, -2$ subspaces. In effect, we have transcribed the entanglement from one set of modes to another, generating correlations that did not previously exist. An illustration of this transcription process is shown in Fig. 3.3.

Four-Dimensional State

In our experiment, we focus on the OAM values $\ell = -2, -1, 1, 2$ for simplicity; as a result, we can ignore the terms with other OAM values, and Eq. (3.18) simplifies to

$$\begin{aligned}\rho_{\mathrm{AD}} = |\mathcal{K}|^2 \Big[& |c_1|^4 |\Psi^-_{1-1}\rangle_{\mathrm{AD}}\langle\Psi^-_{1-1}|_{\mathrm{AD}} + |c_2|^4 |\Psi^-_{2-2}\rangle_{\mathrm{AD}}\langle\Psi^-_{2-2}|_{\mathrm{AD}} \\ & + |c_2|^2|c_1|^2 \Big(|\Psi^-_{2-1}\rangle_{\mathrm{AD}}\langle\Psi^-_{2-1}|_{\mathrm{AD}} + |\Psi^-_{21}\rangle_{\mathrm{AD}}\langle\Psi^-_{21}|_{\mathrm{AD}} \\ & + |\Psi^-_{-2-1}\rangle_{\mathrm{AD}}\langle\Psi^-_{-2-1}|_{\mathrm{AD}} + |\Psi^-_{-21}\rangle_{\mathrm{AD}}\langle\Psi^-_{-21}|_{\mathrm{AD}} \Big) \Big]. \end{aligned} \tag{3.19}$$

This state includes entanglement in all two-dimensional subspaces with unique combinations of OAM values: $\ell = \pm 1$; $\ell = \pm 2$; $\ell = -2, -1$; $\ell = -2, 1$; $\ell = 2, -1$; and $\ell = 2, 1$. Note that the input state to the beamsplitter in Eq. 3.1 only included entanglement in subspaces with equal and opposite OAM values $\ell = \pm 1$ and $\ell = \pm 2$. We see that after the anti-symmetric filter, the entanglement has been transcribed to all two-dimensional subspaces available.

3.5 Experiment

As shown in Fig. 3.4, our experiment uses a pulsed Ti:sapphire laser (Coherent Chameleon Ultra II) centred at 808 nm, with a pulse width of 140 fs and a repetition rate of 80 MHz. Our setup is far from the laser due to space constraints, so to reduce beam wobble, we image the output plane of the laser to the beginning of our setup using a $2f$–$2f$ system of focal length 1000 mm (L1000). Using a lens of focal length 75 mm (L75), we focus the laser into a 0.5-mm-thick BBO crystal (BBO0). The resultant sum frequency generation produces between ≈0 mW and ≈800 mW of ultraviolet (UV) light at 404 nm, depending on the power of the incident 808-nm beam. We choose a UV power output of ≈350 mW in order to optimise the combination of minimal background counts and minimal measurement times, which are in conflict with one another. The reasons behind this are discussed in more depth in Section 5.7.1.

We focus the upconverted light through a 100-μm circular aperture (spatial filter SF) using a 100-mm lens (L100). The light that passes through the aperture is collimated with a 50-mm lens (L50). The spatial filtering at the aperture ensures that the pump beam used for the downconversion has a Gaussian beam profile. The remaining infrared light is removed using two consecutive bandpass filters BF1 (10-nm width centred at 405 nm, each with 2×10^{-5}% transmission of 808-nm light).

The UV light is used to pump a 1-mm BBO crystal (BBO1), producing pairs of photons at 808 nm via type-I, near-collinear SPDC. The remaining UV light is deflected using a dichroic mirror (DM), and the downconverted light continues on

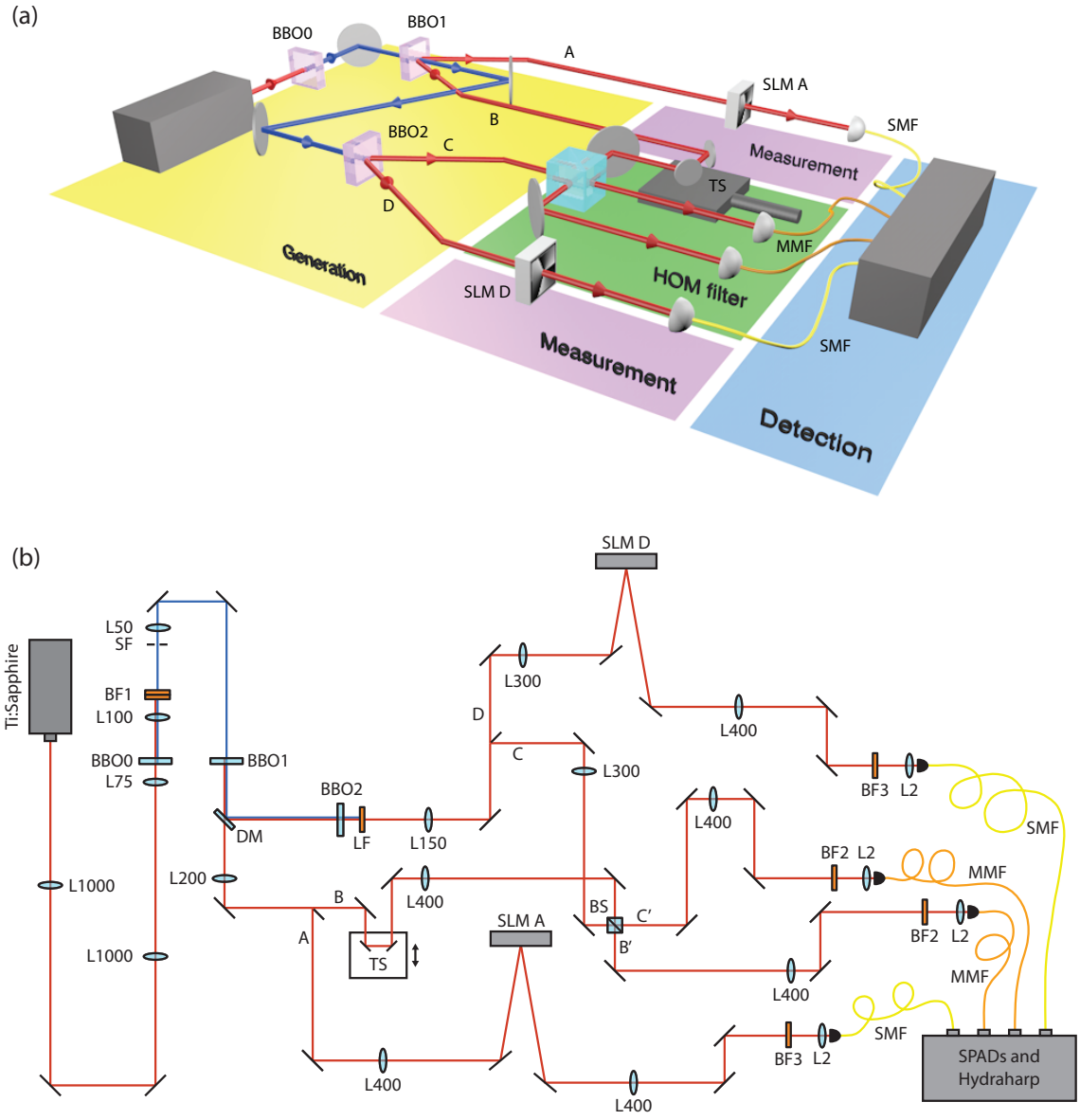

Figure 3.4: **Experimental setup.** (a) A simplified version of the experimental setup. (b) A detailed schematic of the experimental setup. Abbreviations are explained in the main text.

through a 200-mm lens (L200). It is then split using a D-shaped mirror so that one photon continues on as photon B and the other is reflected as photon A. The D-shaped mirror is used so as to split the far field of the downconverted light down the middle, sending half of the photons in one direction and their entangled twins in the other direction.

Photon B strikes two mirrors on a motorised translation stage (TS) for precise path length adjustment. Photon B then passes through a 400-mm lens (L400) before striking a non-polarising beamsplitter (BS) in the image plane of BBO1. Meanwhile, photon A passes through L400 before striking SLM A in the image plane of BBO1. SLM A is imaged to a single-mode fibre (SMF) using L400 and a 2-mm lens (L2).

After being deflected by the dichroic mirror, the UV light then pumps a second 1-mm BBO crystal (BBO2), after which it is filtered out using longpass filter LF (cutoff wavelength 750 nm). A second pair of photons at 808 nm is produced via SPDC and passes through lens L150. It is then split with a D-shaped mirror so that one photon continues on as photon D and the other is reflected as photon C.

Photon D passes through a 300-mm lens (L300) before striking SLM D in the image plane of BBO2. SLM D is imaged to an SMF using L400 and L2. Photon C passes through L300 before striking the BS in the image plane of BBO2.

Here photons B and C undergo Hong-Ou-Mandel (HOM) interference; the exact position of the HOM interference dip is identified by moving the translation stage in path B until a minimum in the four-photon coincidence rate is observed. In Fig. 3.5, we show two HOM dips: the red points indicate when both photons B and C are in the mode $|1\rangle$, accomplished by displaying a $|-1\rangle$ hologram on both SLMs A and D, while the blue points indicate when both photons B and C are in the mode $(|1\rangle + |-1\rangle)/\sqrt{2}$, accomplished by displaying a $(|-1\rangle + |1\rangle)/\sqrt{2}$ hologram on both SLMs A and D. The two HOM dips have very different visibilities, meaning that our measurements in the $(|1\rangle \pm |-1\rangle)/\sqrt{2}$ basis will not have as good a contrast as those in the $|\pm 1\rangle$ basis. After the BS, the new paths B′ and C′ are each imaged to multi-mode fibres (MMFs, core diameter 50 μm) using L400 and L2.

Prior to entering the fibres, each photon encounters a bandpass filter to select a narrow band of wavelengths. BF2, which has a 3-nm spectral width centred at 808 nm, is used in paths B′ and C′ in order to ensure a HOM dip of sufficient width and depth, as the width of the HOM dip is inversely proportional to the width of the photon spectrum and hence the filter. BF3, which has a 20-nm spectral width centred at 810 nm, is used in paths A and D in order to maximise count rates.

Each of the four fibres is connected to a single-photon avalanche detector (SPAD, Excelitas SPCM-800-14-FC), which is in turn connected to a time-tagging system (HydraHarp) with a 12.5-ns coincidence gate. The average four-way coincidence

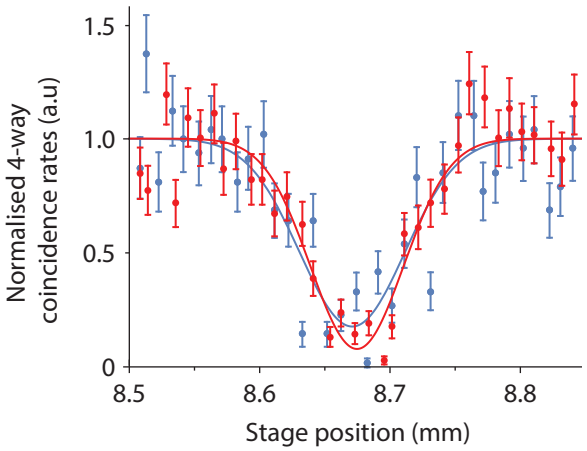

Figure 3.5: **Hong-Ou-Mandel (HOM) interference.** HOM dips for photons in the OAM $\ell = \pm 1$ subspace. The red points show data when the photons in paths B and C are both in the mode $|1\rangle$; the blue points show data when the photons in paths B and C are both in the mode $\frac{1}{\sqrt{2}}(|1\rangle + |-1\rangle)$. We fit a Gaussian curve with a visibility of 0.86 ± 0.04 and 0.70 ± 0.05, respectively. The error bars correspond to the standard deviation of the count rate assuming Poisson statistics, and these data are background-subtracted.

count rate for the $\ell = \pm 1$ subspace is 0.04 counts per second, while the average count rate for the $\ell = \pm 2$ subspace is 0.01 counts per second.

The combined two-dimensional state of photons A and D is determined by displaying holograms of four OAM states on each SLM in turn: $|\ell_1\rangle$, $|\ell_2\rangle$, $(|\ell_1\rangle + |\ell_2\rangle)/\sqrt{2}$, and $(|\ell_1\rangle + i|\ell_2\rangle)/\sqrt{2}$. Using the 16 resulting measurements, we reconstruct the density matrix using quantum state tomography.

3.6 Results

In order to verify that the entanglement has successfully been swapped from photons A and B to photons A and D, we perform two-qubit tomography on all six two-dimensional subspaces in A and D: $\ell = \pm 1$; $\ell = \pm 2$; $\ell = -2, -1$; $\ell = -2, 1$; $\ell = 2, -1$; and $\ell = 2, 1$. The reconstructed states are shown in Fig. 3.6.

The fidelity of each reconstructed state with the expected anti-symmetric state indicates the success of the entanglement swapping. Table 3.1 shows the fidelity for each subspace, the average of which is 0.80 ± 0.10. As these fidelities are limited by the visibility of our HOM dip as detailed in the following paragraph, this indicates excellent overlap between the measured and expected states.

The maximum fidelity of each subspace is constrained by the visibility of our HOM dip. The visibility V is defined as the percentage difference between the

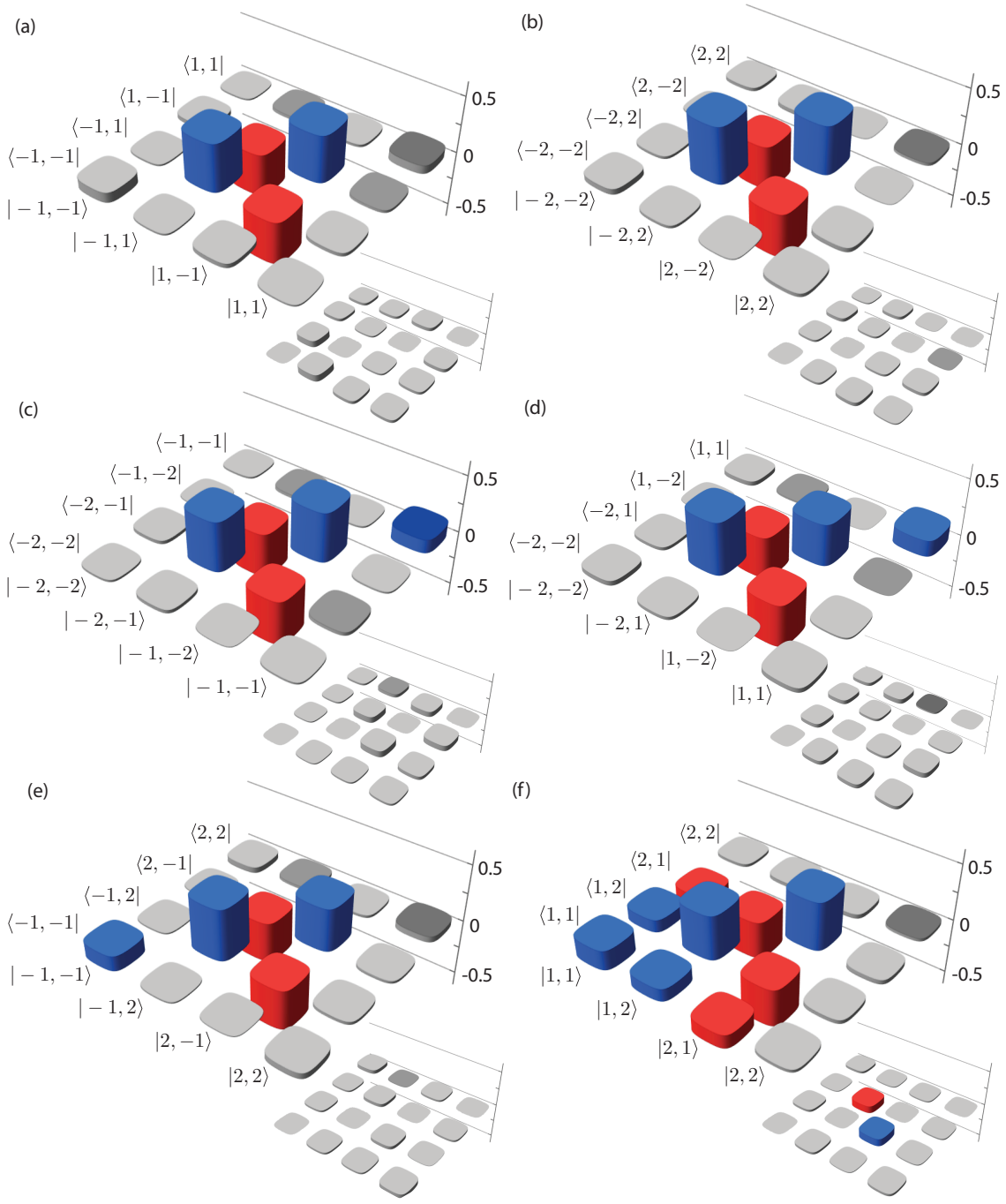

Figure 3.6: **Two-dimensional density matrices.** Reconstructed density matrices of two-dimensional subspaces (a) $\ell = \pm 1$; (b) $\ell = \pm 2$; (c) $\ell = -2, -1$; (d) $\ell = -2, 1$; (e) $\ell = 2, -1$; and (f) $\ell = 2, 1$. Positive values are shown in blue, while negative values are shown in red; grey bars indicate the absolute value is < 0.1. The main images show the real part of the state, while the insets show the imaginary part.

minimum and maximum counts

$$V = \frac{C_{\max} - C_{\min}}{C_{\max} + C_{\min}}. \tag{3.20}$$

This indicates the percentage of events where the interference results in entanglement swapping, meaning that $(1 - V)\%$ of the time, entanglement swapping does not occur and we observe uncorrelated noise. Under this assumption, the theoretically expected state of photons A and D is

$$\rho_{\text{th}} = V|\Psi^-_{\ell k}\rangle\langle\Psi^-_{\ell k}| + (1 - V)\frac{\mathbb{1}}{4}. \tag{3.21}$$

In Fig. 3.7, the blue line represents the theoretical fidelity of ρ_{th} with the ideal state $|\Psi^-_{\ell k}\rangle\langle\Psi^-_{\ell k}|$ as a function of dip visibility.

We can place our measured visibilities and measured fidelity on the graph to estimate whether they are consistent with one another; for example, if our dip visibility is 50%, according to the blue line we would expect to see a fidelity of approximately 60%. We place our measured visibilities on the graph in orange: 0.86 ± 0.04 for the $|1\rangle$ mode and 0.70 ± 0.05 for the $\frac{1}{\sqrt{2}}(|1\rangle + |-1\rangle)$ mode. For these visibilities, we would expect to find a resultant state fidelity of $\approx 85\%$ and $\approx 75\%$, respectively; we have drawn lines leading up to the corresponding points on the blue line to indicate our expected fidelity using each of these visibilities. Similarly, we place our measured fidelity of 0.80 ± 0.02 for the $\ell = \pm 1$ subspace on the graph in green. This fidelity indicates a likely visibility of $\approx 75\%$; we have drawn a line leading to the corresponding point on the blue line to indicate the expected visibility given this measured fidelity. From these points added to the blue line, we see that our actual measured fidelity is between the two expected fidelities based on the measured visibilities. This is because the $\ell = \pm 1$ density matrix is reconstructed from measurements in both of the bases for which we have visibility measurements.

We also use the concurrence of the density matrices to determine the degree of entanglement in the state. Zero concurrence indicates no entanglement present, while unit concurrence indicates a maximally entangled state. Table 3.1 shows the concurrence for each subspace, the average of which is 0.68 ± 0.18. This indicates an acceptable amount of entanglement exists between photons A and D, which were not entangled at the beginning of the experiment.

Note that we calculate our standard deviations under the assumption that both the raw counts and the background-subtracted counts follow a Poisson distribution. We simulate each count rate 100 different times with a Poisson distribution centred at the measured count rate. We reconstruct the density matrices each time and calculate the corresponding fidelity and concurrence, then take the standard deviation of the results.

Table 3.1: **Measures of entanglement.** Fidelity and concurrence for each of the six two-dimensional subspaces.

Subspace	Fidelity	Concurrence
$\ell = \pm 1$	0.80 ± 0.02	0.67 ± 0.04
$\ell = \pm 2$	0.86 ± 0.04	0.75 ± 0.08
$\ell = -2, -1$	0.83 ± 0.04	0.76 ± 0.07
$\ell = -2, 1$	0.77 ± 0.02	0.65 ± 0.05
$\ell = 2, -1$	0.79 ± 0.07	0.65 ± 0.11
$\ell = 2, 1$	0.74 ± 0.04	0.61 ± 0.07
Average	0.80 ± 0.10	0.68 ± 0.18

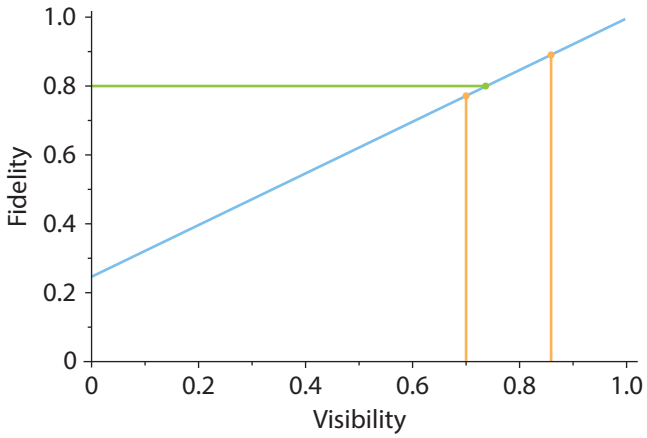

Figure 3.7: **Fidelity vs. visibility.** Fidelity of the predicted state with the ideal states as a function of HOM visibility for the $\ell = \pm 1$ subspace. The green point corresponds to the measured fidelity (0.80 ± 0.02); the orange points correspond to the measured four-way HOM visibility of the data in Figure 3.5 (0.86 ± 0.04 and 0.70 ± 0.05). The blue line corresponds to the theoretical prediction.

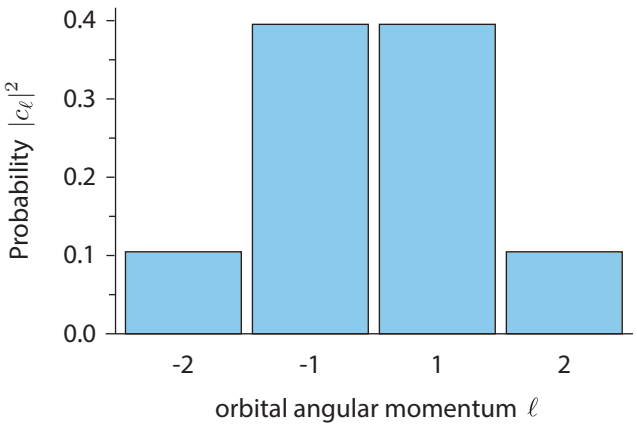

Figure 3.8: **Experimentally measured OAM distribution.**

3.6.1 Estimation of Four-Dimensional State

We combine the six two-dimensional density matrices in order to estimate the four-dimensional state. The state we expect to find is in Eq. (3.19). The majority of the elements in this density matrix are zero; the rest correspond to the two-dimensional subspace matrices appropriately placed into the four-dimensional matrix. We note that the fidelity between a pure state and any other state depends only on the nonzero elements, as shown in Section 1.3.3. Thus if we are comparing a measured matrix to a sparse pure state matrix, we need only measure the elements that are expected to be nonzero; measuring the elements expected to be zero will not provide further information about the fidelity. As a result, we can estimate the four-dimensional state using only the two-dimensional density matrices.

We determine the OAM distribution over the four OAM values of interest by comparing the count rates from the ± 1 and ± 2 subspaces

$$|c_{\text{ratio}}|^2 = \frac{|c_2|^2}{|c_1|^2} = \frac{M[-2,-2] + M[-2,2] + M[2,-2] + M[2,2]}{M[-1,-1] + M[-1,1] + M[1,-1] + M[1,1]}, \tag{3.22}$$

where $M[\ell_1, \ell_2]$ is the result of a projective measurement of the state $|\ell_1\rangle_{\text{A}}|\ell_2\rangle_{\text{D}}$. We can then obtain an estimated OAM distribution $\{|c_{-2}|^2, |c_{-1}|^2, |c_1|^2, |c_2|^2\} = \{|c_2|^2, |c_1|^2, |c_1|^2, |c_2|^2\}$ given by $A/\sum_i A[i]$, where $A = \{|c_{\text{ratio}}|^2, 1, 1, |c_{\text{ratio}}|^2\}$. The estimated OAM distribution is shown in Fig. 3.8.

Substituting this estimated OAM distribution and the six measured two-dimensional density matrices into Eq. (3.19), we obtain an estimate of the four-dimensional state, as shown in Fig. 3.9(a). We compare this estimated density matrix to the theoretical state given by Eq. (3.19) with the estimated OAM distribution and the theoretically expected two-dimensional states, as shown in Fig. 3.9(b). We find a fidelity of 0.79 ± 0.01, indicating acceptable overlap between the states.

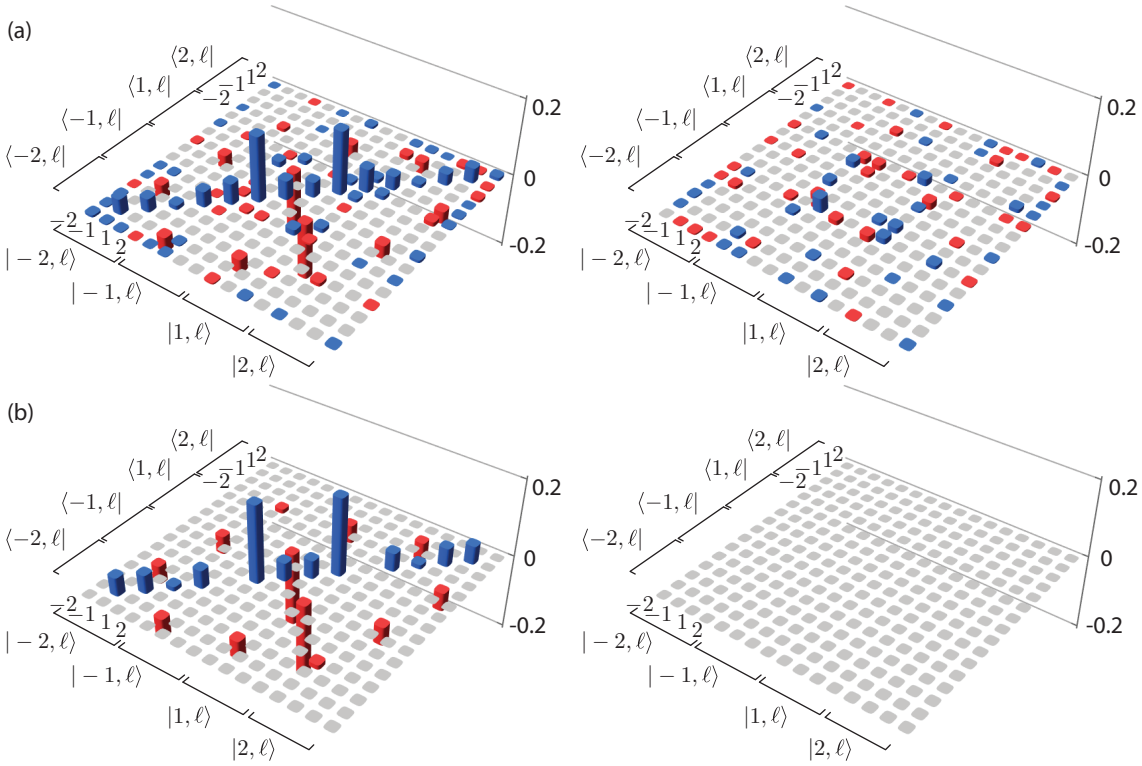

Figure 3.9: **Four-dimensional density matrix.** Estimated density matrix of the joint state of A and D for the four-dimensional space with $\ell = \pm 1, \pm 2$. (a) The state estimated using the reconstructed density matrices of all six two-dimensional subspaces in Eq. (3.19). (b) The theoretical prediction using the experimentally observed OAM distribution. Positive values are shown in blue, while negative values are shown in red; grey indicates the element is unmeasured in (a) or zero in (b). The real parts of the states are on the left, while the imaginary parts are on the right.

3.7 Background Subtraction

In our experiment, we use spatial light modulators (SLMs) and single-mode fibres to detect photons in paths A and D and multi-mode fibres to detect photons in paths B and C. The use of multi-mode fibres is so that we detect within the 4-dimensional space spanning the modes $\{\ell = -2, \ell = -1, \ell = +1, \ell = +2\}$ in an unrestricted fashion, i.e., we do not select out a subspace in paths B and C. The use of additional SLMs and single-mode fibres, rather than multi-mode fibres, would enable a choice of which particular space we detect in, but it would also remove the ability to observe multiple subspaces at once to obtain a high-dimensional state.

A consequence of the multi-mode fibres is, however, that the rate of the single-photon detection events at detectors B and C is significantly higher than that recorded at detectors A and D. Table 3.2 provides representative single-channel and coincidence count rates recorded for the $\ell = \pm 1$ and $\ell = \pm 2$ subspaces. The B and C single-channel rates recorded with the multi-mode fibres are on average $\approx$4 times higher than those recorded at A and D. This trend is observed across all the subspaces that we investigate.

The high count rates in the multi-mode fibres are mainly due to the fibres' indiscriminate acceptance of all OAM modes. In arms A and D, we select out the modes of interest by projecting them into a Gaussian state, leaving the remaining modes in non-Gaussian states and unable to couple into single-mode fibres. However, multi-mode fibres accept all OAM modes, so they accept the photons in B and C that are entangled with the photons in A and D that *do not* make it through the single-mode fibre due to being in the wrong mode. These uncorrelated counts are partially responsible for our high background level.

The large single-channel rates resulting from the multi-mode fibres contribute to unwanted 4-way coincidence counts that do not participate in any entanglement swapping. However, these unwanted 4-way coincidences that arise from uncorrelated photon detection events can be calculated and subtracted off the measured 4-way counts.

3.7.1 Expected 4-Way Coincidence

To determine the number of background counts, we first estimate the number of 4-way coincidences we expect. For a single pair of entangled photons A and B, we denote the rate of detected coincidence events as C'_{AB}. If the pump laser producing the entangled pair via SPDC has repetition rate R, then the probability that a coincidence event will be detected is C'_{AB}/R. For a second pair of entangled photons C and D, produced by the same laser via SPDC in a second crystal, the probability

Table 3.2: **Raw count rates.** Representative count rates for the $\ell = \pm 1$ and $\ell = \pm 2$ subspaces. The background count rate calculated using Eq. (3.26) is also shown. All rates are in counts per second.

	Single-channel counts			
Subspace	S_A	S_B	S_C	S_D
$\ell = \pm 1$	77 000	280 000	280 000	64 000
$\ell = \pm 2$	70 000	280 000	280 000	61 000
	Two-channel coincidence counts			
Subspace	C_{AB}	C_{AC}	C_{BD}	C_{CD}
$\ell = \pm 1$	1800	1500	1700	1500
$\ell = \pm 2$	1000	900	1000	900

	Four-channel coincidence counts		
Subspace	Expected raw counts	Background-subtracted	Accidentals
$\ell = \pm 1$	0.07	0.05	0.02
$\ell = \pm 2$	0.02	0.01	0.01

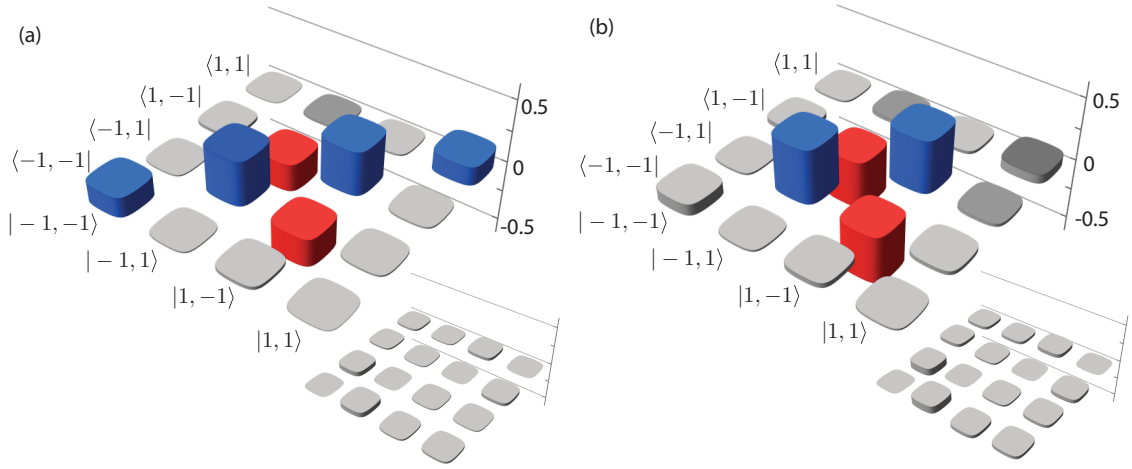

Figure 3.10: **Background subtraction.** Density matrices reconstructed using (a) the raw counts and (b) the background-subtracted counts for the $\ell = \pm 1$ subspace.

is C'_{CD}/R. Thus the probability to detect one pair in detectors A and B and the other pair in detectors C and D is

$$\frac{C'_{AB}C'_{CD}}{R^2}. \tag{3.23}$$

Multiplying by the repetition rate, we obtain the rate of detection of both photon pairs

$$\frac{C'_{AB}C'_{CD}}{R}. \tag{3.24}$$

However, as photons B and C interact in our experiment, it is also possible for the first pair to be detected in A and C (rather than A and B) and the second pair to be detected in B and D (rather than C and D). Taking this possibility into account, we obtain the total rate of 4-way coincidence events from two entangled pairs

$$C'_{4\mathrm{W}} = \frac{1}{R}\left(C'_{\mathrm{AB}}C'_{\mathrm{CD}} + C'_{\mathrm{AC}}C'_{\mathrm{BD}}\right). \tag{3.25}$$

3.7.2 Background of 4-Way Coincidence

The above equation includes accidental counts, which occur in any coincidence experiment and are caused by two uncorrelated photons arriving at the detectors at the same time. Thus the accidentals can be expressed as $A_{ij} = S_i S_j / R$ where S_i is the number of single counts at detector i. The detected counts C'_{ij} are then the sum of the real coincidences C_{ij} and the accidentals A_{ij}, allowing Eq. (3.25) to be written as

$$\begin{aligned} C'_{4\mathrm{W}} &= \frac{1}{R}\left[\left(C_{\mathrm{AB}} + \frac{S_{\mathrm{A}}S_{\mathrm{B}}}{R}\right)\left(C_{\mathrm{CD}} + \frac{S_{\mathrm{C}}S_{\mathrm{D}}}{R}\right) + \left(C_{\mathrm{AC}} + \frac{S_{\mathrm{A}}S_{\mathrm{C}}}{R}\right)\left(C_{\mathrm{BD}} + \frac{S_{\mathrm{B}}S_{\mathrm{D}}}{R}\right)\right] \\ &= \frac{1}{R}(C_{\mathrm{AB}}C_{\mathrm{CD}} + C_{\mathrm{AC}}C_{\mathrm{BD}}) \\ &\quad + \frac{1}{R^2}(C_{\mathrm{AB}}S_{\mathrm{C}}S_{\mathrm{D}} + S_{\mathrm{A}}S_{\mathrm{B}}C_{\mathrm{CD}} + C_{\mathrm{AC}}S_{\mathrm{B}}S_{\mathrm{D}} + S_{\mathrm{A}}S_{\mathrm{C}}C_{\mathrm{BD}}) + \frac{2}{R^3}S_{\mathrm{A}}S_{\mathrm{B}}S_{\mathrm{C}}S_{\mathrm{D}} \\ &= C_{4\mathrm{W}} + A_{4\mathrm{W}}. \end{aligned} \tag{3.26}$$

We subtract the calculated number of background counts $A_{4\mathrm{W}}$ from the measured data $C'_{4\mathrm{W}}$ to obtain the actual number of counts $C_{4\mathrm{W}}$. Occasionally with count rates that are expected to be very low, the measured number of counts is smaller than the expected number of background counts; in this case, we replace the count rate with zero.

3.7.3 Impact of Background Subtraction

We can use either the raw counts or the background-subtracted counts to calculate density matrices from which fidelities and concurrences are extracted. Figure 3.10 and Table 3.3 provide evidence of the impact of the background subtraction on the quality of our entanglement swapping. As can be seen, a higher fidelity and concurrence (0.80 ± 0.10 and 0.68 ± 0.18) is observed for the density matrix generated using the background-subtracted data as compared to that using the raw counts (0.54 ± 0.08 and 0.09 ± 0.14).

This increase in quality when background subtraction is applied is to be expected. If, as mentioned above, we project into the $\ell = \pm 1$ subspace using SLMs and

Table 3.3: **Raw vs. background-subtracted.** Comparison of the fidelity and concurrence for the raw and background-subtracted counts.

	BS		Raw	
Subspace	Fidelity	Concurrence	Fidelity	Concurrence
$\ell = \pm 1$	0.80 ± 0.02	0.67 ± 0.04	0.57 ± 0.02	0.16 ± 0.05
$\ell = \pm 2$	0.86 ± 0.04	0.75 ± 0.08	0.50 ± 0.03	0.01 ± 0.05
$\ell = -2, -1$	0.83 ± 0.04	0.76 ± 0.07	0.58 ± 0.03	0.24 ± 0.07
$\ell = -2, 1$	0.77 ± 0.02	0.65 ± 0.05	0.49 ± 0.02	0.03 ± 0.04
$\ell = 2, -1$	0.79 ± 0.07	0.65 ± 0.11	0.50 ± 0.05	0.05 ± 0.08
$\ell = 2, 1$	0.74 ± 0.04	0.61 ± 0.07	0.49 ± 0.03	0.05 ± 0.05
Average	0.80 ± 0.10	0.68 ± 0.18	0.54 ± 0.08	0.09 ± 0.14

single-mode fibres in paths B and C, the raw count rates would only differ from the background-subtracted rates by $\approx 1\%$. This in turn would result in a very small difference between the two different density matrices, and high fidelities and concurrences would be observed in both cases.

3.8 Pure Final State

While OAM forms a high-dimensional state space, the above results only have entanglement in two dimensions due to the action of the anti-symmetric filter on only two-dimensional anti-symmetric states. A true high-dimensional filter would project onto a pure high-dimensional final state, rather than a mixture of pure two-dimensional states.

This can be achieved by replacing the anti-symmetric filter with a nonlinear crystal to perform upconversion of photons B and C. If the resultant upconverted photon is collected using a single-mode fibre, it ensures that photons B and C have equal and opposite OAM. Thus photons B and C will be projected into the state

$|\psi_{\text{upc}}\rangle = \sum_\ell a_\ell |\ell\rangle_{\text{B}}|-\ell\rangle_{\text{C}}$. The resultant state is

$$\begin{aligned}
|\psi_{\text{pure}}\rangle =& \Big(\mathbb{1}_{\text{AD}} \otimes |\psi_{\text{upc}}\rangle_{\text{BC}}\langle\psi_{\text{upc}}|_{\text{BC}}\Big)|\psi_{\text{init}}\rangle \\
=& \left(\mathbb{1}_{\text{AD}} \otimes \sum_i a_i |i\rangle_{\text{B}}|-i\rangle_{\text{C}} \sum_j a_j^* \langle j|_{\text{B}}\langle -j|_{\text{C}}\right) \\
& \qquad \times \left(\sum_\ell c_\ell |\ell\rangle_{\text{A}}|-\ell\rangle_{\text{B}} \otimes \sum_k c_k |k\rangle_{\text{C}}|-k\rangle_{\text{D}}\right) \\
=& \sum_{ij\ell k} a_i a_j^* c_\ell c_k \delta_{j-\ell}\delta_{-jk} |i\rangle_{\text{B}}|-i\rangle_{\text{C}}|\ell\rangle_{\text{A}}|-k\rangle_{\text{D}} \\
=& \sum_{ij} a_i a_j^* c_j^2 |i\rangle_{\text{B}}|-i\rangle_{\text{C}}|-j\rangle_{\text{A}}|j\rangle_{\text{D}} \\
=& \sum_i a_i |i\rangle_{\text{B}}|-i\rangle_{\text{C}} \otimes \sum_j a_j^* c_j^2 |-j\rangle_{\text{A}}|j\rangle_{\text{D}}. \qquad (3.27)
\end{aligned}$$

Thus photons A and D end up in the pure, high-dimensionally entangled state $|\psi\rangle_{\text{AD}} = \sum_\ell a_\ell^* c_\ell^2 |-\ell\rangle_{\text{A}}|\ell\rangle_{\text{D}}$.

In practice, the upconversion of two single photons is an extremely low-probability event [140]. However, it is a promising possibility to extend full entanglement swapping to high-dimensional systems as these techniques develop further.

Chapter 4

Teleportation of Multiple Orbital Angular Momentum States of Light

4.1 Notes and Acknowledgements

In this chapter, we describe teleportation of the orbital angular momentum of light. We teleport several two-dimensional OAM states and describe a method of incomplete teleportation of high-dimensional OAM states.

The work in this chapter formed part of a collaboration with colleagues from South Africa. The data used in this chapter is taken from the data in Chapter 3. A manuscript is being prepared for publication:

M. Agnew, Y. Zhang, F.S. Roux, T. Konrad, D. Faccio, J. Leach, A. Forbes, *Teleportation of multiple orbital angular momentum states of light*, in preparation.

Contributions to this chapter are as follows:

YZ, MA, and JL performed the experiment. MA performed the data analysis. MA provided the theoretical framework with guidance from FSR and TK. JL, FSR, AF and DF supervised the project, and the idea was conceived by JL, FSR, AF and TK. The text in this thesis was written exclusively by MA.

4.2 Overview

Quantum teleportation is a key component of many quantum communication applications, allowing the transmission of information from one location to another without physically moving the system in which the information is encoded. Here we discuss quantum teleportation of orbital angular momentum states of light. We demonstrate experimentally the teleportation of several two-dimensional OAM states. We also describe the partial teleportation of high-dimensional OAM states using a beamsplitter, as well as the potential for complete teleportation of high-dimensional states using upconversion. This represents an important first step towards high-dimensional quantum teleportation, which will allow for higher information capacity in quantum communication.

4.3 Background

Quantum entanglement allows the transfer of information from one particle to another over large distances. This process is called quantum teleportation [51] and relies on a joint measurement between the state being teleported and the state of one entangled particle. This measurement reproduces the information in the second entangled particle, while destroying the state of the initial particle; thus teleportation does not violate the no-cloning theorem [141]. Teleportation has applications in quantum communication [133] and quantum computing [69, 142] and was first performed experimentally in 1997 [52]. It has since been repeated in many different experiments in various quantum systems [55–62, 143–146].

The most common system used for quantum communication is the polarisation of single photons. This is because photons are ideal carriers of information; they travel fast and can easily be coupled into fibres to protect from turbulence. However, there is a limit to how far a photon can go before the state becomes unusable. This is where teleportation provides an advantage; the photon holding the quantum state of interest need not travel the entire distance to its destination. Instead, an entangled pair is generated and each photon of the pair can be sent half the desired distance: one to the transmitter and one to the receiver. This extends the range of quantum communication to twice the usual distance, and in fact, cascading teleportations can extend this range indefinitely.

Photons can also carry orbital angular momentum (OAM), which manifests in a spatial structure forming an infinite-dimensional but discrete state space. High-dimensional systems like OAM can carry more information than simple two-dimensional systems like polarisation, making them an ideal candidate for communication applications [124]. Recently, teleportation of multiple degrees of freedom of a single

photon (polarisation and OAM) was demonstrated [53, 54].

Here, we demonstrate experimentally teleportation of orbital angular momentum qubits. As teleportation is a necessary consequence of entanglement swapping, we use the data from Chapter 3. We also discuss the possibility of partial and full teleportation of high-dimensional states.

4.4 Theory

Recall the general concept of teleportation as described in Section 1.5.3. Bob has a quantum state $\alpha|H\rangle_{\mathrm{B}} + \beta|V\rangle_{\mathrm{B}}$ that he would like Delilah to have; see Fig. 1.18. He also has a pair of entangled photons in the state $|\Psi^+\rangle_{\mathrm{DC}}$ to facilitate this. Bob sends photon D to Delilah and performs a Bell measurement on the remaining photons B and C. If Bob chooses to project only onto the $|\Psi^-\rangle$ Bell state and Delilah does not apply the final unitary on her photon, then we expect the state $\frac{1}{2}\big(\alpha|H\rangle_{\mathrm{D}} - \beta|V\rangle_{\mathrm{D}}\big)$ in Delilah's photon.

Here we will examine the same scenario, but we will examine the orbital angular momentum of light instead of the polarisation state. When dealing with the polarisation of photons, a two-dimensional state space, a Bell measurement is typically accomplished using a beamsplitter; a coincidence between the two output ports indicates that particles B and C are in the anti-symmetric state $|\Psi^-\rangle$. In a high-dimensional system such as OAM, there exists more than one anti-symmetric state; therefore, combining photons B and C on a beamsplitter and postselecting on coincidences projects the two photons into one of several anti-symmetric states. This results in transmission of the complete but scrambled quantum information from photon B to photon D. We will explain what "complete" and "scrambled" mean in the context of quantum information in this chapter.

We begin with a general superposition of OAM states in photon B $\sum_m a_m|m\rangle_{\mathrm{B}}$, which we would like to teleport, and a high-dimensional entangled state in photons C and D:

$$|\psi\rangle = \sum_m a_m|m\rangle_{\mathrm{B}} \otimes \sum_\ell c_\ell|\ell\rangle_{\mathrm{C}}|-\ell\rangle_{\mathrm{D}}. \tag{4.1}$$

Recall the action of the anti-symmetric state filter

$$|\ell\rangle_{\mathrm{B}} \to \frac{1}{\sqrt{2}}\Big(|\ell\rangle_{\mathrm{C}} - |\ell\rangle_{\mathrm{B}}\Big) \tag{4.2}$$

$$|\ell\rangle_{\mathrm{C}} \to \frac{1}{\sqrt{2}}\Big(|\ell\rangle_{\mathrm{C}} + |\ell\rangle_{\mathrm{B}}\Big). \tag{4.3}$$

Applying the filter to photons B and C in this state, we obtain

$$\begin{aligned}
|\psi\rangle &= \sum_m a_m |m\rangle_{\mathrm{B}} \otimes \sum_\ell c_\ell |\ell\rangle_{\mathrm{C}} |-\ell\rangle_{\mathrm{D}} \\
&\xrightarrow{\text{filter}} \sum_m a_m \frac{1}{\sqrt{2}}\Big(|m\rangle_{\mathrm{C}} - |m\rangle_{\mathrm{B}}\Big) \otimes \sum_\ell c_\ell \frac{1}{\sqrt{2}}\Big(|\ell\rangle_{\mathrm{C}} + |\ell\rangle_{\mathrm{B}}\Big)|-\ell\rangle_{\mathrm{D}} \\
&\xrightarrow{3-\text{ways}} \mathcal{K} \sum_m \sum_\ell \frac{a_m c_\ell}{2}\Big(|m\rangle_{\mathrm{C}}|\ell\rangle_{\mathrm{B}} - |m\rangle_{\mathrm{B}}|\ell\rangle_{\mathrm{C}}\Big)|-\ell\rangle_{\mathrm{D}} \\
|\psi_{\mathrm{out}}\rangle &= \frac{\mathcal{K}}{\sqrt{2}} \sum_m \sum_\ell a_m c_\ell |\Psi^-_{\ell m}\rangle_{\mathrm{BC}} |-\ell\rangle_{\mathrm{D}}. \qquad (4.4)
\end{aligned}$$

We can then trace out photons B and C to obtain the state of photon D:

$$\begin{aligned}
\rho_{\mathrm{D}} &= \sum_k \sum_n \sum_{i=1}^{4} \langle \phi^{(i)}_{kn}|_{\mathrm{BC}} \Big(|\psi_{\mathrm{out}}\rangle\langle\psi_{\mathrm{out}}|\Big) |\phi^{(i)}_{kn}\rangle_{\mathrm{BC}} \\
&= \sum_k \sum_n \langle \Psi^-_{kn}|_{\mathrm{BC}} \Big(|\psi_{\mathrm{out}}\rangle\langle\psi_{\mathrm{out}}|\Big) |\Psi^-_{kn}\rangle_{\mathrm{BC}} \\
&= \sum_{kn} \langle \Psi^-_{kn}|_{\mathrm{BC}} \Bigg(\frac{\mathcal{K}}{\sqrt{2}} \sum_m \sum_\ell a_m c_\ell |\Psi^-_{\ell m}\rangle_{\mathrm{BC}} |-\ell\rangle_{\mathrm{D}} \\
&\qquad\qquad \times \frac{\mathcal{K}}{\sqrt{2}} \sum_q \sum_p a^*_q c^*_p \langle \Psi^-_{pq}|_{\mathrm{BC}} \langle -p|_{\mathrm{D}} \Bigg) |\Psi^-_{kn}\rangle_{\mathrm{BC}} \\
&= \frac{\mathcal{K}^2}{2} \sum_{kn} \sum_{m\ell} \sum_{qp} a_m a^*_q c_\ell c^*_p (\delta_{k\ell}\delta_{nm} - \delta_{km}\delta_{n\ell})(\delta_{pk}\delta_{qn} - \delta_{pn}\delta_{kq}) |-\ell\rangle_{\mathrm{D}} \langle -p|_{\mathrm{D}} \\
&= \frac{\mathcal{K}^2}{2} \sum_{m\ell} \sum_{qp} a_m a^*_q c_\ell c^*_p (\delta_{p\ell}\delta_{qm} - \delta_{pm}\delta_{q\ell} - \delta_{pm}\delta_{q\ell} + \delta_{p\ell}\delta_{qm}) |-\ell\rangle_{\mathrm{D}} \langle -p|_{\mathrm{D}} \\
&= \mathcal{K}^2 \sum_{m\ell} \Big(|a_m|^2 |c_\ell|^2 |-\ell\rangle_{\mathrm{D}} \langle -\ell|_{\mathrm{D}} - a_m a^*_\ell c_\ell c^*_m |-\ell\rangle_{\mathrm{D}} \langle -m|_{\mathrm{D}} \Big). \qquad (4.5)
\end{aligned}$$

The diagonal elements in this density matrix are $|c_\ell|^2\big(1 - |a_\ell|^2\big)$, while the off-diagonal elements are of the form $-a_m a^*_\ell c_\ell c^*_m = -|a_m||a_\ell| c_\ell c^*_m e^{i(\phi_\ell - \phi_m)}$. Thus in the case of a uniform OAM distribution ($c_\ell = c_m$), performing tomography on the state of photon D reveals full information about the coefficients a_m of the initial state to be teleported. While this is not true teleportation, the information has been transmitted partially intact and can be recovered, which is an intriguing result.

In the case of a two-dimensional subspace with OAM ℓ, k, this reduces to

$$\begin{aligned}
\rho_{\mathrm{D}} = \mathcal{K}^2 \Big(& |a_\ell|^2 |c_\ell|^2 |-\ell\rangle_{\mathrm{D}} \langle -\ell|_{\mathrm{D}} - a_\ell a^*_\ell c_\ell c^*_\ell |-\ell\rangle_{\mathrm{D}} \langle -\ell|_{\mathrm{D}} \\
& + |a_\ell|^2 |c_k|^2 |-k\rangle_{\mathrm{D}} \langle -k|_{\mathrm{D}} - a_\ell a^*_k c_k c^*_\ell |-k\rangle_{\mathrm{D}} \langle -\ell|_{\mathrm{D}} \\
& + |a_k|^2 |c_\ell|^2 |-\ell\rangle_{\mathrm{D}} \langle -\ell|_{\mathrm{D}} - a_k a^*_\ell c_\ell c^*_k |-\ell\rangle_{\mathrm{D}} \langle -k|_{\mathrm{D}} \\
& + |a_k|^2 |c_k|^2 |-k\rangle_{\mathrm{D}} \langle -k|_{\mathrm{D}} - a_k a^*_k c_k c^*_k |-k\rangle_{\mathrm{D}} \langle -k|_{\mathrm{D}} \Big) \\
= \mathcal{K}^2 \Big(& |a_k|^2 |c_\ell|^2 |-\ell\rangle_{\mathrm{D}} \langle -\ell|_{\mathrm{D}} - a_k a^*_\ell c_\ell c^*_k |-\ell\rangle_{\mathrm{D}} \langle -k|_{\mathrm{D}} \\
& - a_\ell a^*_k c_k c^*_\ell |-k\rangle_{\mathrm{D}} \langle -\ell|_{\mathrm{D}} + |a_\ell|^2 |c_k|^2 |-k\rangle_{\mathrm{D}} \langle -k|_{\mathrm{D}} \Big). \qquad (4.6)
\end{aligned}$$

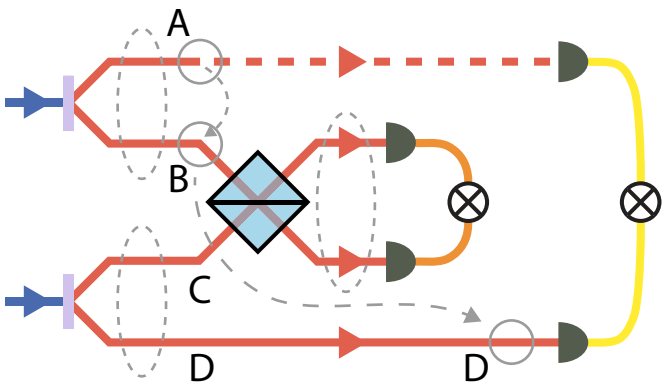

Figure 4.1: **Teleportation using remote state preparation.** The state of photon B is prepared by performing a projective measurement on photon A. The state of photon B is then teleported to photon D using a Bell measurement on photons B and C.

We can use a Dove prism to reverse the sign of the OAMs and return the photon to the original basis:

$$\begin{aligned}
\rho'_{\mathrm{D}} &= M_{\mathrm{Dove}}\rho_{\mathrm{D}}M^{\dagger}_{\mathrm{Dove}} \\
&= \Big(\sum_m |-m\rangle_{\mathrm{D}}\langle m|_{\mathrm{D}}\Big)\rho_{\mathrm{D}}\Big(\sum_n |n\rangle_{\mathrm{D}}\langle -n|_{\mathrm{D}}\Big) \\
&= \mathcal{K}^2\sum_m\sum_n |-m\rangle_{\mathrm{D}}\Big(|a_k|^2|c_\ell|^2\delta_{m-\ell}\delta_{-\ell n} - a_k a^*_\ell c_\ell c^*_k\delta_{m-\ell}\delta_{-kn} \\
&\qquad - a_\ell a^*_k c_k c^*_\ell\delta_{m-k}\delta_{-\ell n} + |a_\ell|^2|c_k|^2\delta_{m-k}\delta_{-kn}\Big)\langle -n|_{\mathrm{D}} \\
&= \mathcal{K}^2\Big(|a_k|^2|c_\ell|^2|\ell\rangle_{\mathrm{D}}\langle\ell|_{\mathrm{D}} - a_k a^*_\ell c_\ell c^*_k|\ell\rangle_{\mathrm{D}}\langle k|_{\mathrm{D}} \\
&\qquad - a_\ell a^*_k c_k c^*_\ell|k\rangle_{\mathrm{D}}\langle\ell|_{\mathrm{D}} + |a_\ell|^2|c_k|^2|k\rangle_{\mathrm{D}}\langle k|_{\mathrm{D}}\Big).
\end{aligned} \tag{4.7}$$

The original state can then be recovered using the unitary operation σ_y

$$\begin{aligned}
\rho''_{\mathrm{D}} &= \sigma_y\rho'_{\mathrm{D}}\sigma^{\dagger}_y \\
&= \Big(i|\ell\rangle_{\mathrm{D}}\langle k|_{\mathrm{D}} - i|k\rangle_{\mathrm{D}}\langle\ell|_{\mathrm{D}}\Big)\rho'_{\mathrm{D}}\Big(i|\ell\rangle_{\mathrm{D}}\langle k|_{\mathrm{D}} - i|k\rangle_{\mathrm{D}}\langle\ell|_{\mathrm{D}}\Big) \\
&= \mathcal{K}^2\Big(|a_k|^2|c_\ell|^2|k\rangle_{\mathrm{D}}\langle k|_{\mathrm{D}} + a_k a^*_\ell c_\ell c^*_k|k\rangle_{\mathrm{D}}\langle\ell|_{\mathrm{D}} \\
&\qquad + a_\ell a^*_k c_k c^*_\ell|\ell\rangle_{\mathrm{D}}\langle k|_{\mathrm{D}} + |a_\ell|^2|c_k|^2|\ell\rangle_{\mathrm{D}}\langle\ell|_{\mathrm{D}}\Big).
\end{aligned} \tag{4.8}$$

In the case that we begin with a maximally entangled state, i.e., $c_\ell = c_k = 1/\sqrt{2}$, we obtain the exact original state, thus achieving full teleportation in any two-dimensional subspace.

4.5 Experiment

As teleportation is necessarily a consequence of entanglement swapping, we use the same data acquired in Chapter 3. Thus our experimental setup is described in detail

in Section 3.5 and shown in Fig. 3.4.

In our particular system, we use remote state preparation as described in Section 1.4.4 to prepare photon B in the desired state. To this end, we require a fourth photon, A, to begin entangled with photon B, as shown in Fig. 4.1. This changes the above equations as follows for our experimental implementation.

Consider the initial four-photon state

$$|\Psi\rangle = \sum_{\ell} c_\ell |\ell\rangle_{\rm A}|-\ell\rangle_{\rm B} \otimes \sum_k c_k |k\rangle_{\rm C}|-k\rangle_{\rm D}. \tag{4.9}$$

We prepare the state of photon B using remote state preparation by projecting photon A into the state $|\psi\rangle_{\rm A} = \alpha|q\rangle_{\rm A} + \beta|p\rangle_{\rm B}$. This acts on the overall state as

$$\begin{aligned}
\langle\psi|_{\rm A}|\Psi\rangle &= \Big(\alpha^*\langle q|_{\rm A} + \beta^*\langle p|_{\rm A}\Big) \sum_{\ell} c_\ell |\ell\rangle_{\rm A}|-\ell\rangle_{\rm B} \otimes \sum_k c_k |k\rangle_{\rm C}|-k\rangle_{\rm D} \\
&= \sum_{\ell} c_\ell \Big(\alpha^*\delta_{q\ell}|-\ell\rangle_{\rm B} + \beta^*\delta_{p\ell}|-\ell\rangle_{\rm B}\Big) \otimes \sum_k c_k |k\rangle_{\rm C}|-k\rangle_{\rm D} \\
&= \Big(c_q\alpha^*|-q\rangle_{\rm B} + c_p\beta^*|-p\rangle_{\rm B}\Big) \otimes \sum_k c_k |k\rangle_{\rm C}|-k\rangle_{\rm D}.
\end{aligned} \tag{4.10}$$

In the ideal case of $c_i = 1/\sqrt{d}$ when measuring a d-dimensional subspace, photon B is now in the state $\alpha^*|-q\rangle_{\rm B} + \beta^*|-p\rangle_{\rm B}$, which is the state we would like to teleport.

We then project photons B and C into the relevant anti-symmetric state using the HOM filter

$$\begin{aligned}
&\langle\Psi^-_{-p-q}|_{\rm BC}\Big(c_q\alpha^*|-q\rangle_{\rm B} + c_p\beta^*|-p\rangle_{\rm B}\Big) \otimes \sum_k c_k |k\rangle_{\rm C}|-k\rangle_{\rm D} \\
&= \frac{1}{\sqrt{2}}\Big(\langle -p|_{\rm B}\langle -q|_{\rm C} - \langle -q|_{\rm B}\langle -p|_{\rm C}\Big)\Big(c_q\alpha^*|-q\rangle_{\rm B} + c_p\beta^*|-p\rangle_{\rm B}\Big) \otimes \sum_k c_k |k\rangle_{\rm C}|-k\rangle_{\rm D} \\
&= \frac{1}{\sqrt{2}} \sum_k c_k \Big(c_q\beta^*\delta_{-qk}|-k\rangle_{\rm D} - c_p\alpha^*\delta_{-pk}|-k\rangle_{\rm D}\Big) \\
&= \frac{1}{\sqrt{2}}\Big(c_q c_{-q}\beta^*|q\rangle_{\rm D} - c_p c_{-p}\alpha^*|p\rangle_{\rm D}\Big).
\end{aligned} \tag{4.11}$$

Again, in the ideal case that $c_i = 1/\sqrt{d}$, this implements the operation

$$\alpha^*|-q\rangle_{\rm B} + \beta^*|-p\rangle_{\rm B} \to \beta^*|q\rangle_{\rm D} - \alpha^*|p\rangle_{\rm D}. \tag{4.12}$$

The original state can then be recovered using a Dove prism and σ_y operation, resulting in teleportation of the state in photon B to photon D.

4.6 Results

We examine six two-dimensional subspaces: $\ell = \pm 1$; $\ell = \pm 2$; $\ell = 1, 2$; $\ell = -1, 2$; $\ell = 1, -2$; and $\ell = -1, -2$. In each subspace, we measure six resultant states: $|\ell_1\rangle$,

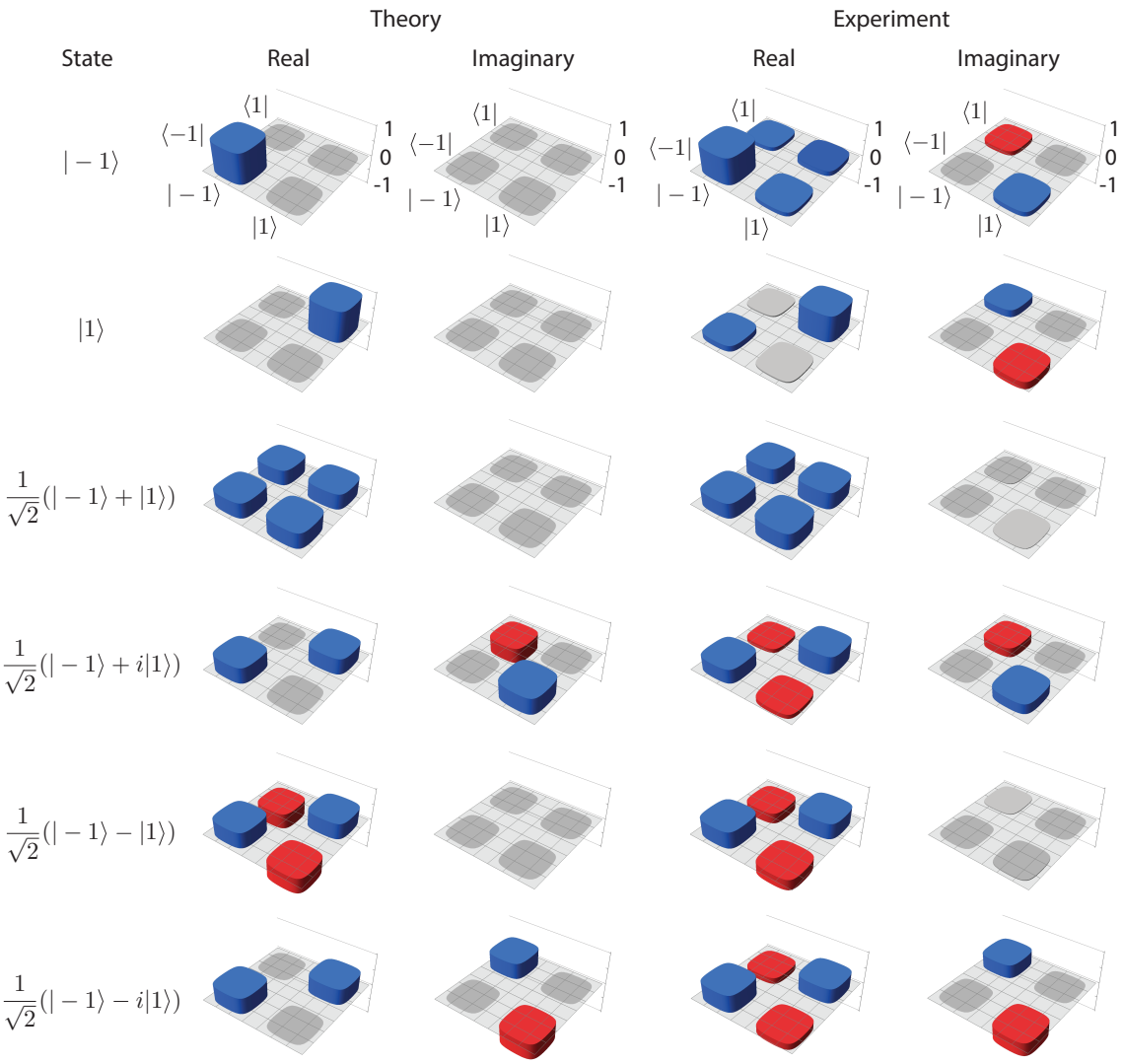

Figure 4.2: **Teleported qubit states.** We compare the theoretically expected density matrices (first column real, second column imaginary) to the measured density matrices (third column real, fourth column imaginary) for six input states in the subspace $\ell = \pm 1$. The six states are $|-1\rangle$ (a-b), $|1\rangle$ (c-d), $\big(|-1\rangle + |1\rangle\big)/\sqrt{2}$ (e-f), $\big(|-1\rangle + i|1\rangle\big)/\sqrt{2}$ (g-h), $\big(|-1\rangle - |1\rangle\big)/\sqrt{2}$ (i-j), and $\big(|-1\rangle - i|1\rangle\big)/\sqrt{2}$ (k-l).

$|\ell_2\rangle$, $\big(|\ell_1\rangle + |\ell_2\rangle\big)/\sqrt{2}$, $\big(|\ell_1\rangle + i|\ell_2\rangle\big)/\sqrt{2}$, $\big(|\ell_1\rangle - |\ell_2\rangle\big)/\sqrt{2}$, and $\big(|\ell_1\rangle - i|\ell_2\rangle\big)/\sqrt{2}$. We obtained all these data in our entanglement swapping experiment in Chapter 3.

As we do not transform the resulting state using a Dove prism and σ_y operation, we perform quantum state tomography on photon D when it is in the state of Eq. (4.11). We show the reconstructed density matrices for the subspace $\ell = \pm 1$ in Fig. 4.2.

We calculate the fidelity between the measured state and the expected state. The fidelities each of the six states in each subspace are shown in Tables 4.1 and 4.2, and the average fidelities of all six states in each subspace are shown in Table 4.3.

State	BS Fidelity	Raw Fidelity
$\|-1\rangle$	0.85 ± 0.03	0.71 ± 0.03
$\|1\rangle$	0.82 ± 0.04	0.69 ± 0.03
$\big(\|-1\rangle + \|1\rangle\big)/\sqrt{2}$	0.999 ± 0.005	0.76 ± 0.04
$\big(\|-1\rangle + i\|1\rangle\big)/\sqrt{2}$	0.81 ± 0.05	0.68 ± 0.04
$\big(\|-1\rangle - \|1\rangle\big)/\sqrt{2}$	0.83 ± 0.04	0.69 ± 0.03
$\big(\|-1\rangle - i\|1\rangle\big)/\sqrt{2}$	0.93 ± 0.03	0.75 ± 0.03
$\|-2\rangle$	0.96 ± 0.03	0.67 ± 0.05
$\|2\rangle$	0.90 ± 0.05	0.67 ± 0.05
$\big(\|-2\rangle + \|2\rangle\big)/\sqrt{2}$	0.74 ± 0.10	0.58 ± 0.06
$\big(\|-2\rangle + i\|2\rangle\big)/\sqrt{2}$	0.96 ± 0.03	0.75 ± 0.05
$\big(\|-2\rangle - \|2\rangle\big)/\sqrt{2}$	0.97 ± 0.03	0.70 ± 0.06
$\big(\|-2\rangle - i\|2\rangle\big)/\sqrt{2}$	0.86 ± 0.07	0.63 ± 0.06
$\|1\rangle$	0.95 ± 0.03	0.77 ± 0.05
$\|2\rangle$	0.69 ± 0.07	0.56 ± 0.05
$\big(\|1\rangle + \|2\rangle\big)/\sqrt{2}$	0.84 ± 0.05	0.65 ± 0.04
$\big(\|1\rangle + i\|2\rangle\big)/\sqrt{2}$	0.83 ± 0.05	0.67 ± 0.05
$\big(\|1\rangle - \|2\rangle\big)/\sqrt{2}$	0.78 ± 0.07	0.62 ± 0.04
$\big(\|1\rangle - i\|2\rangle\big)/\sqrt{2}$	0.93 ± 0.04	0.71 ± 0.04

Table 4.1: **Fidelity of teleported qubits.** We calculate fidelity for the states reconstructed from background-subtracted counts and the states reconstructed from raw counts for the six states of interest in each subspace. (Subspaces $\ell = \pm 1$; $\ell = \pm 2$; and $\ell = 1, 2$.)

State	BS Fidelity	Raw Fidelity
$\|-1\rangle$	0.62 ± 0.09	0.79 ± 0.11
$\|2\rangle$	0.79 ± 0.15	0.53 ± 0.11
$\big(\|-1\rangle + \|2\rangle\big)/\sqrt{2}$	0.84 ± 0.06	0.69 ± 0.08
$\big(\|-1\rangle + i\|2\rangle\big)/\sqrt{2}$	0.91 ± 0.06	0.67 ± 0.10
$\big(\|-1\rangle - \|2\rangle\big)/\sqrt{2}$	0.89 ± 0.05	0.71 ± 0.09
$\big(\|-1\rangle - i\|2\rangle\big)/\sqrt{2}$	0.82 ± 0.10	0.64 ± 0.10
$\|-2\rangle$	0.65 ± 0.04	0.53 ± 0.03
$\|1\rangle$	0.98 ± 0.01	0.76 ± 0.04
$\big(\|-2\rangle + \|1\rangle\big)/\sqrt{2}$	0.84 ± 0.03	0.67 ± 0.03
$\big(\|-2\rangle + i\|1\rangle\big)/\sqrt{2}$	0.98 ± 0.01	0.72 ± 0.03
$\big(\|-2\rangle - \|1\rangle\big)/\sqrt{2}$	0.88 ± 0.04	0.64 ± 0.04
$\big(\|-2\rangle - i\|1\rangle\big)/\sqrt{2}$	0.88 ± 0.04	0.66 ± 0.04
$\|-2\rangle$	0.94 ± 0.04	0.60 ± 0.06
$\|-1\rangle$	0.99 ± 0.02	0.89 ± 0.04
$\big(\|-2\rangle + \|-1\rangle\big)/\sqrt{2}$	0.97 ± 0.02	0.77 ± 0.04
$\big(\|-2\rangle + i\|-1\rangle\big)/\sqrt{2}$	0.88 ± 0.06	0.66 ± 0.05
$\big(\|-2\rangle - \|-1\rangle\big)/\sqrt{2}$	0.78 ± 0.06	0.65 ± 0.06
$\big(\|-2\rangle - i\|-1\rangle\big)/\sqrt{2}$	0.96 ± 0.02	0.74 ± 0.04

Table 4.2: **Fidelity of teleported qubits (continued).** We calculate fidelity for the states reconstructed from background-subtracted counts and the states reconstructed from raw counts for the six states of interest in each subspace. (Subspaces $\ell = -1, 2$; $\ell = 1, -2$; and $\ell = -1, -2$.)

Subspace	BS Fidelity	Raw Fidelity
± 1	0.87 ± 0.07	0.71 ± 0.04
± 2	0.90 ± 0.09	0.67 ± 0.06
$1, 2$	0.84 ± 0.09	0.66 ± 0.07
$-1, 2$	0.81 ± 0.10	0.67 ± 0.08
$1, -2$	0.87 ± 0.12	0.67 ± 0.08
$-1, -2$	0.92 ± 0.08	0.72 ± 0.10

Table 4.3: **Average fidelities of teleported qubits.** The average fidelity of the six states in each subspace, for the background-subtracted and raw data.

We would like to ensure that our quantum teleportation exceeds any teleportation possible classically. Classical teleportation consists of estimating a state based on a single measurement. While it is possible to guess correctly occasionally and obtain 100% fidelity, on average the best fidelity attainable is $2/(d+1)$ for dimension d [147]. In the single-qubit case, this means quantum teleportation must exceed 67% fidelity in order to beat classical teleportation.

As seen in Table 4.1, all of our background-subtracted density matrices in subspace $\ell = \pm 1$ have fidelities several standard deviations above the classical limit. In particular, the fidelity of the state $\big(|-1\rangle + |1\rangle\big)/\sqrt{2}$ is an astonishing 65σ above the classical limit. This is clearly an artefact of the background subtraction method, implying that perhaps our estimation of the background counts is a bit optimistic. Of the density matrices in subspace $\ell = \pm 1$ reconstructed directly from the raw counts, only some have fidelities one or more standard deviations above the classical limit. This indicates that the sources of noise in our experiment need to be significantly better controlled for the system to be useful for teleportation, as we cannot perform background subtraction in an actual application of teleportation.

As seen in the remainder of Table 4.1 and in Table 4.2, the remaining subspaces have mixed results. Fidelities of states with $\ell = -2$ or $\ell = 2$ typically have lower fidelities and larger standard deviations; this is due to the narrow OAM distribution and thus low count rates detected in $\ell = \pm 2$. This can be most clearly seen in subspace $\ell = 1, 2$ in Table 4.1; the state $|1\rangle$ performs quite well (0.95 ± 0.03), while the remaining states, all of which have a component in state $|2\rangle$, have lower fidelities. This could be resolved using entanglement concentration [110].

An interesting difference is observed between the fidelities of the same states as measured in different subspaces. For example, consider the state $|1\rangle$ as measured in the $\ell = \pm 1$ subspace (the third row in Table 4.1); this state has BS fidelity 0.82 ± 0.04. Conversely, the same state $|1\rangle$ as measured in the $\ell = 1, 2$ subspace (the fourteenth row in Table 4.1) has a BS fidelity of 0.95 ± 0.03. This drastic difference is also apparent in the raw fidelities.

The reason for this is the non-uniform OAM distribution in our experiment. The states $|1\rangle$ and $|-1\rangle$ have approximately equal count rates, while the state $|2\rangle$ produces a quarter of the counts of $|1\rangle$. Thus, even if we are teleporting the state $|1\rangle$ at 82% fidelity, the $|2\rangle$ measurement can only produce a quarter of the 18% of the total counts we would expect in this case. This artificially inflates the fidelity of the state $|1\rangle$ in this subspace. Similarly, the state $|2\rangle$ has only 69% fidelity in the $\ell = 1, 2$ subspace, while it has 90% fidelity in the $\ell = \pm 2$ subspace, which is caused by the same effect. For this reason, it is likely that the fidelities calculated in the $\ell = \pm 1$ and $\ell = \pm 2$ subspaces are the most accurate, as these were measured with similar count rates for all basis states.

Note that we calculate our standard deviation under the assumption that both the raw counts and the background-subtracted counts follow a Poisson distribution. We simulate each count rate 100 different times with a Poisson distribution centred at the measured count rate. We reconstruct the density matrices each time and calculate the corresponding fidelity, then take the standard deviation of the results.

For the remaining subspaces, the average fidelities for the background-subtracted data as shown in Table 4.3 are between one and four standard deviations above the classical limit. The average fidelities for the raw data are not significantly above the classical limit; however, it is important to note that these are averages and some individual density matrices will have fidelities significantly above the classical limit.

4.7 Conclusions

We have demonstrated quantum teleportation for two-dimensional OAM states of light using a beamsplitter and mirrors to filter two-dimensional anti-symmetric states. We have also described the action of the anti-symmetric filter on high-dimensional OAM states, concluding that it results in transmission of the information, but not in the usual definition of teleportation. The solution to this is to use a high-dimensional anti-symmetric state filter, which could take the form of sum frequency generation using the two photons involved in the measurement. This idea is detailed for entanglement swapping in Section 3.8, but it could be applied in the same fashion for teleportation purposes. In fact, it would be more feasible for teleportation as the information to be teleported need not necessarily be imprinted on a heralded single photon; a weak coherent source will do. This would greatly increase the probability of sum frequency generation occurring.

Chapter 5

Ghost Imaging Using Photons that Have Not Interacted

5.1 Notes and Acknowledgements

In this chapter, we demonstrate ghost imaging using two photons that have never interacted. The correlations that enable this arise from entanglement swapping and result in a contrast-reversed image.

The work in this chapter formed part of a collaboration with colleagues from South Africa. A manuscript is being prepared for publication:

M. Agnew, F. Zhu, N. Bornman, A. Valles, D. Faccio, A. Forbes, J. Leach, *Ghost imaging using photons that have not interacted*, in preparation.

Contributions to this chapter are as follows:

MA and JL performed the experiment. MA performed the data analysis. MA and NB provided the theoretical framework. JL and AF supervised the project, and the idea was conceived by JL and AF. The text in this thesis was written exclusively by MA.

5.2 Overview

Ghost imaging is an intriguing phenomenon that results in an image of an object by detecting the light from the object using a detector with no spatial information. This is accomplished using correlations with the light to infer the result. Here we demonstrate ghost imaging using two photons that have not interacted at all; in this case, the correlations come from swapping the entanglement of two separate pairs of entangled photons. The nature of the entanglement swapping results in contrast reversal of the detected image.

5.3 Background

Ghost imaging refers to the ability to obtain an image using spatial information from light that has not directly interacted with the object being imaged. The first realisation of this used light generated by SPDC [49]. An object was placed in the path of the signal photon, and the resulting light was detected using a bucket detector. A bucket detector contains no spatial information, meaning that an image of the object could not be recovered with the signal photon alone. Simultaneously, the idler photon, with no object in its path, was detected with a spatially resolving detector, which in this case was a fibre tip scanned in the detection plane. As the idler photon did not interact with the object, the image of the object could not be recovered with the idler photon alone. However, the combination of the two detectors yields an image using coincidence detection.

This first paper sparked the idea that ghost imaging was a quantum phenomenon, though the authors did concede that the effect might also occur with a classical source. Since this first paper, it has become clear that ghost imaging occurs with both quantum [148–153] and classical [50, 154–159] light. In fact, it is not even necessary to have two correlated light beams; only the information about the spatial structure of the light beam is required [160–164].

Regardless of the physical implementation of the ghost imaging setup, the mathematics are the same. All that is required is the signal from a bucket detector after light passes through the object, which we will denote S, as well as information about the light incident on the object, which we will denote M. The latter information is determined in a different way in each implementation, as seen in Fig. 5.1.

For the SPDC implementation (Fig. 5.1(a)), the incident light information is obtained using a coincidence signal between the signal arm and the idler arm. The spatially-resolving detector indicates the position of the light in the idler arm, which reveals the position of the light in the signal arm, thus providing M.

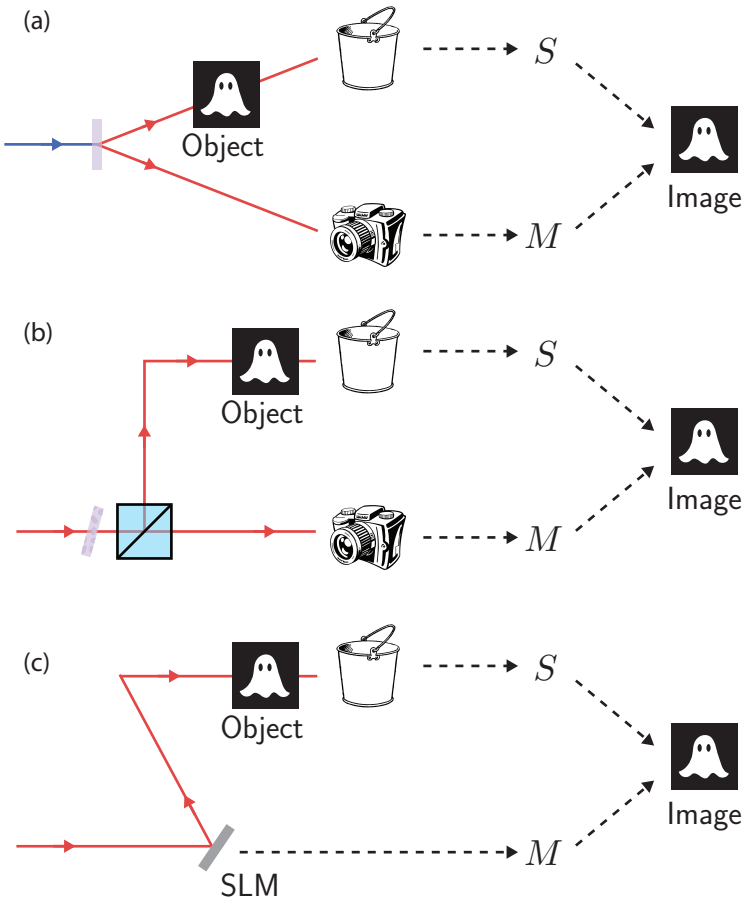

Figure 5.1: **Methods of ghost imaging.** (a) Quantum ghost imaging with SPDC source. (b) Thermal ghost imaging with speckle patterns. (c) Computational ghost imaging.

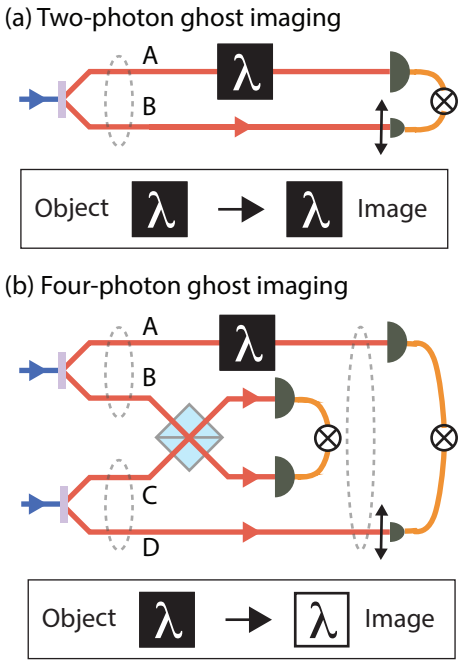

Figure 5.2: **Two-photon vs. four-photon ghost imaging.** (a) Two-photon ghost imaging. (b) Four-photon ghost imaging enabled by entanglement swapping.

For the thermal implementation (Fig. 5.1(b)), M is similarly obtained using the coincidence signal between the object arm and the non-object arm. A camera placed in the non-object arm provides information about the speckle pattern M that is also incident on the object.

For the computational implementation (Fig. 5.1(c)), a computer is controlling the structure of the light incident on the object. M is then the mask placed on the light-structuring device.

In all cases, by running the experiment many times with different illuminations M_i producing different signals S_i, we can reconstruct the object O using

$$O = \sum_i M_i S_i. \tag{5.1}$$

Here we use the principal of ghost imaging in a quantum system with correlations between two photons that have never interacted. This is accomplished via entanglement swapping of two separate pairs of entangled photons; by performing a Bell measurement on one photon from each pair, the two other photons become entangled despite never having interacted. We can then use these photons to produce a contrast-reversed ghost image. See Fig. 5.2 for a comparison of two-photon and four-photon ghost imaging.

5.4 Theory

We start with two SPDC sources producing pairs of entangled photons, the first pair in paths A and B and the second in paths C and D. We are interested in the position basis in this chapter. Since experimentally we can only measure discrete positions, we divide the area of interest into $d_1 \times d_2$ pixels. Each area spanning horizontal positions x_{i-1} to x_i and vertical positions y_{j-1} to y_j in arm k can be represented as $|x_i, y_j\rangle_k$, where we set $x_0 = y_0 = 0$ and $\{1,1\} \leq \{i,j\} \leq \{d_1, d_2\}$. In order to reduce the number of indices used, we will write $|x_i, y_j\rangle_k$ as $|q\rangle$, where $q = j + d_2(i-1)$, $1 \leq q \leq d$ and $d = d_1 d_2$. Then the spatial state of the photons can be written

$$|\Psi_0\rangle = \sum_{q=1}^{d^2} c_q |q\rangle_A |q\rangle_B \otimes \sum_{p=1}^{d^2} c_p |p\rangle_C |p\rangle_D, \tag{5.2}$$

where $|c_q|^2$ is the probability of finding both photons in block q.

The anti-symmetric state filter acts on the position basis in the same way as the OAM basis as discussed in Chapters 2 and 3:

$$\begin{pmatrix} q_1^\dagger \\ q_2^\dagger \end{pmatrix} = \frac{1}{\sqrt{2}} \begin{pmatrix} 1 & 1 \\ 1 & -1 \end{pmatrix} \begin{pmatrix} q_3^\dagger \\ q_4^\dagger \end{pmatrix}. \tag{5.3}$$

This can be re-written in terms of the position states of photons B and C before and after the filter

$$|q\rangle_{\mathrm{B}} \to \frac{1}{\sqrt{2}} \Big(|q\rangle_{\mathrm{C}} - |q\rangle_{\mathrm{B}} \Big) \tag{5.4}$$

$$|q\rangle_{\mathrm{C}} \to \frac{1}{\sqrt{2}} \Big(|q\rangle_{\mathrm{C}} + |q\rangle_{\mathrm{B}} \Big). \tag{5.5}$$

Applying this transformation to the initial state, we obtain

$$\begin{aligned} |\Psi_0\rangle \xrightarrow{\text{filter}} & \sum_{q=1}^{d^2} c_q |q\rangle_{\mathrm{A}} \frac{1}{\sqrt{2}} \Big(|q\rangle_{\mathrm{C}} - |q\rangle_{\mathrm{B}} \Big) \otimes \sum_{p=1}^{d^2} c_p \frac{1}{\sqrt{2}} \Big(|p\rangle_{\mathrm{C}} + |p\rangle_{\mathrm{B}} \Big) |p\rangle_{\mathrm{D}} \\ = & \sum_{q=1}^{d^2} \sum_{p=1}^{d^2} \frac{c_q c_p}{2} |q\rangle_{\mathrm{A}} \Big(|q\rangle_{\mathrm{C}} |p\rangle_{\mathrm{C}} + |q\rangle_{\mathrm{C}} |p\rangle_{\mathrm{B}} - |q\rangle_{\mathrm{B}} |p\rangle_{\mathrm{C}} - |q\rangle_{\mathrm{B}} |p\rangle_{\mathrm{B}} \Big) |p\rangle_{\mathrm{D}} \\ \xrightarrow{4-\text{ways}} & \mathcal{K} \sum_{q=1}^{d^2} \sum_{p=1}^{d^2} \frac{c_q c_p}{2} |q\rangle_{\mathrm{A}} \Big(|p\rangle_{\mathrm{B}} |q\rangle_{\mathrm{C}} - |q\rangle_{\mathrm{B}} |p\rangle_{\mathrm{C}} \Big) |p\rangle_{\mathrm{D}}, \end{aligned} \tag{5.6}$$

where we have postselected on four-fold coincidences.

Tracing out photons B and C, we obtain the density matrix of photons A and D

$$\begin{aligned}
\rho_{\mathrm{AD}} &= \sum_{m=1}^{d^2}\sum_{n=1}^{d^2}\langle m|_{\mathrm{B}}\langle n|_{\mathrm{C}}\left[\mathcal{K}\sum_{q=1}^{d^2}\sum_{p=1}^{d^2}\frac{c_q c_p}{2}|q\rangle_{\mathrm{A}}\Big(|p\rangle_{\mathrm{B}}|q\rangle_{\mathrm{C}}-|q\rangle_{\mathrm{B}}|p\rangle_{\mathrm{C}}\Big)|p\rangle_{\mathrm{D}}\right] \\
&\qquad\qquad \times\left[\mathcal{K}^*\sum_{s=1}^{d^2}\sum_{t=1}^{d^2}\frac{c_s^* c_t^*}{2}\langle s|_{\mathrm{A}}\Big(\langle t|_{\mathrm{B}}\langle s|_{\mathrm{C}}-\langle s|_{\mathrm{B}}\langle t|_{\mathrm{C}}\Big)\langle t|_{\mathrm{D}}\right]|m\rangle_{\mathrm{B}}|n\rangle_{\mathrm{C}} \\
&= \frac{|\mathcal{K}|^2}{4}\sum_{m=1}^{d^2}\sum_{n=1}^{d^2}\sum_{q=1}^{d^2}\sum_{p=1}^{d^2}\sum_{s=1}^{d^2}\sum_{t=1}^{d^2}c_q c_p c_s^* c_t^*|q\rangle_{\mathrm{A}}|p\rangle_{\mathrm{D}}\langle s|_{\mathrm{A}}\langle t|_{\mathrm{D}} \\
&\qquad\qquad \times\Big(\delta_{mp}\delta_{nq}-\delta_{mq}\delta_{np}\Big)\Big(\delta_{tm}\delta_{sn}-\delta_{sm}\delta_{tn}\Big) \\
&= \frac{|\mathcal{K}|^2}{2}\sum_{q=1}^{d^2}\sum_{p=1}^{d^2}\sum_{s=1}^{d^2}\sum_{t=1}^{d^2}c_q c_p c_s^* c_t^*|q\rangle_{\mathrm{A}}|p\rangle_{\mathrm{D}}\langle s|_{\mathrm{A}}\langle t|_{\mathrm{D}}\Big(\delta_{tp}\delta_{sq}-\delta_{sp}\delta_{tq}\Big) \\
&= \frac{|\mathcal{K}|^2}{2}\sum_{q=1}^{d^2}\sum_{p=1}^{d^2}|c_q|^2|c_p|^2\Big(|q\rangle_{\mathrm{A}}\langle q|_{\mathrm{A}}|p\rangle_{\mathrm{D}}\langle p|_{\mathrm{D}}-|q\rangle_{\mathrm{A}}\langle p|_{\mathrm{A}}|p\rangle_{\mathrm{D}}\langle q|_{\mathrm{D}}\Big). \qquad (5.7)
\end{aligned}$$

Now we place an object in the path of photon A whose position state corresponds to $|\mathrm{obj}\rangle_{\mathrm{A}}=\sum_{m=1}^{d^2}a_m|m\rangle_A$. Then the state of photon D is

$$\begin{aligned}
\rho_{\mathrm{D}} &= \langle\mathrm{obj}|_{\mathrm{A}}\rho_{\mathrm{AD}}|\mathrm{obj}\rangle_{\mathrm{A}} \\
&= \frac{|\mathcal{K}|^2}{2}\sum_{m=1}^{d^2}a_m^*\langle m|_A\sum_{q=1}^{d^2}\sum_{p=1}^{d^2}|c_q|^2|c_p|^2\Big(|q\rangle_{\mathrm{A}}\langle q|_{\mathrm{A}}|p\rangle_{\mathrm{D}}\langle p|_{\mathrm{D}} \\
&\qquad\qquad -|q\rangle_{\mathrm{A}}\langle p|_{\mathrm{A}}|p\rangle_{\mathrm{D}}\langle q|_{\mathrm{D}}\Big)\sum_{n=1}^{d^2}a_n|n\rangle_A \\
&= \frac{|\mathcal{K}|^2}{2}\sum_{m=1}^{d^2}\sum_{n=1}^{d^2}\sum_{q=1}^{d^2}\sum_{p=1}^{d^2}a_m^* a_n|c_q|^2|c_p|^2\Big(\delta_{qm}\delta_{qn}|p\rangle_{\mathrm{D}}\langle p|_{\mathrm{D}}-\delta_{qm}\delta_{pn}|p\rangle_{\mathrm{D}}\langle q|_{\mathrm{D}}\Big) \\
&= \frac{|\mathcal{K}|^2}{2}\sum_{q=1}^{d^2}\sum_{p=1}^{d^2}|c_q|^2|c_p|^2\Big(|a_q|^2|p\rangle_{\mathrm{D}}\langle p|_{\mathrm{D}}-a_q^* a_p|p\rangle_{\mathrm{D}}\langle q|_{\mathrm{D}}\Big). \qquad (5.8)
\end{aligned}$$

Now let us examine a simple projective measurement of the intensity of photon D

at position m:

$$\begin{aligned}
\langle m|\rho_{\mathrm{D}}|m\rangle &= \langle m|\frac{|\mathcal{K}|^2}{2}\sum_{q=1}^{d^2}\sum_{p=1}^{d^2}|c_q|^2|c_p|^2\Big(|a_q|^2|p\rangle\langle p| - a_q^* a_p|p\rangle\langle q|\Big)|m\rangle \\
&= \frac{|\mathcal{K}|^2}{2}\sum_{q=1}^{d^2}\sum_{p=1}^{d^2}|c_q|^2|c_p|^2\Big(|a_q|^2\delta_{mp}\delta_{pm} - a_q^* a_p\delta_{mp}\delta_{qm}\Big) \\
&= \frac{|\mathcal{K}|^2}{2}\left[\sum_{q=1}^{d^2}|c_q|^2|c_m|^2|a_q|^2 - |c_m|^2|c_m|^2|a_m|^2\right] \\
&= \frac{|\mathcal{K}|^2|c_m|^2}{2}\left[\sum_{q=1}^{d^2}|c_q|^2|a_q|^2 - |c_m|^2|a_m|^2\right] \\
&= \frac{|\mathcal{K}|^2|c_m|^2}{2}\sum_{q=1,q\neq m}^{d^2}|c_q|^2|a_q|^2. \qquad (5.9)
\end{aligned}$$

From this we see that there will only be intensity observed in photon D at position m if any $|a_{q\neq m}|^2 > 0$. This results in a contrast-reversed image of the object, with slight variations if the OAM distribution $|c_q|^2$ is not uniform.

5.5 Experiment

Our experimental setup is identical to that used in Chapter 3 and consists of a Ti:sapphire laser at a wavelength of 808 nm and a repetition rate of 80 MHz (see Fig. 3.4). We pump a 0.5-mm-thick β-barium borate (BBO) crystal to produce 360 mW of upconverted light at 404 nm. This light then pumps two BBO crystals, each 1 mm thick, to produce downconverted entangled photons, labelled A and B from crystal 1 and C and D from crystal 2. We filter the downconversion immediately after the crystal using 20-nm bandpass filters centred at 810 nm. Additionally we later filter photons B and C with 3-nm bandpass filters centred at 808 nm to ensure a good HOM dip visibility.

In order to produce correlations between photons A and D, we interfere photons B and C on a beamsplitter. Using a translation stage in the path of photon B, we can match the path lengths of photons B and C so that they undergo Hong-Ou-Mandel interference. This projects their joint state into one of the four two-dimensional Bell states, from which the anti-symmetric state can be selected by postselecting on four-fold coincidences. We place an object in arm A, experimentally realised using a spatial light modulator (SLM); we then use a second SLM in arm D to make measurements.

The light is collected using single-mode fibres (SMFs) in arms A and D as this results in very few background counts. However, we use multi-mode fibres (MMFs)

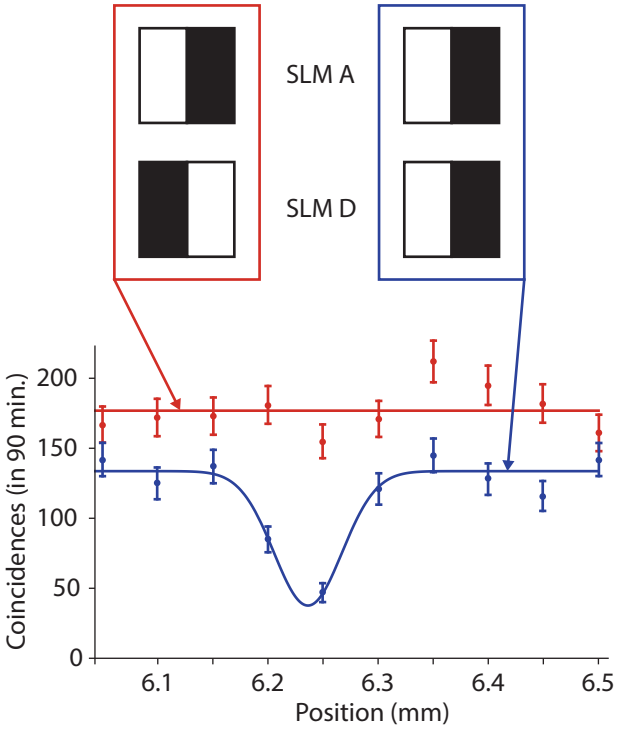

Figure 5.3: **Hong-Ou-Mandel dip.** Four-fold coincidence counts as a function of translation stage position for two cases: contrast-reversed pattern on one SLM (red) and same pattern on both SLMs (blue). There is no discernible reduction in counts for the contrast-reversed case, while there is a dip at 6.24 mm with visibility 0.56 for the same-pattern case.

in arms B and C to ensure that we are collecting as many spatial modes as possible after the interference. The light is detected using single-photon avalanche diodes (Excelitas SPCM-800-14-FC), and time tagging and coincidence counting is performed using a Picoquant HydraHarp.

5.6 Results

First, we examine the behaviour of the system with a simple two-pixel image, as shown in Fig. 5.3. We display an image on SLM A with one half "on" and one half "off". On SLM D we display either the same image or the contrast-reversed image. We then measure the number of four-fold coincidences as we vary the path length difference between photons B and C. We see a Hong-Ou-Mandel dip in the case where both SLMs have the same pattern on them, while the coincidences stay constant in the case where the SLMs have opposite patterns. This indicates contrast reversal.

We also examine the case of a four-pixel image, with the bottom left quarter of SLM A illuminated and the remainder dark as in Fig. 5.4(a). On SLM D we scan

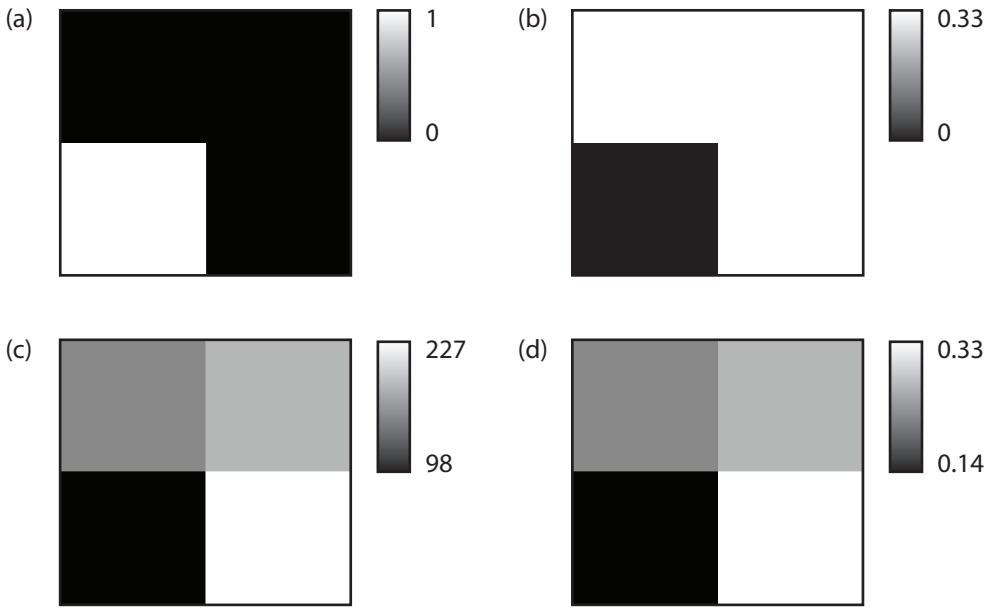

Figure 5.4: **Contrast-reversed image.** (a) Object image on SLM A. (b) Theoretically predicted image in photon D. (c) Raw four-fold coincidence counts detected in photon D. (d) Normalised image in photon D.

through one pixel at a time to obtain four measurements, which are then combined to determine the total image observed in photon D. As shown in Fig. 5.4(b), we expect a contrast-reversed image based on Eq. (5.9).

The raw four-fold coincidences are shown in Fig. 5.4(c), and a normalised image is shown in Fig. 5.4(d). As expected, we obtain a contrast-reversed image in photon D. To quantify how close our measured image is to the expected image, we compare the normalised recovered image to the theoretically predicted image using the mean squared error

$$\mathrm{MSE} = \frac{1}{NM}\sum_{x=0}^{N}\sum_{y=0}^{M}\Big[I(x,y) - P(x,y)\Big]^2, \tag{5.10}$$

where $I(x,y)$ is the intensity of the measured image at pixel $\{x,y\}$ and $P(x,y)$ is the intensity of the predicted image at pixel $\{x,y\}$. For our particular predicted image, the MSE can range from zero for a measured image identical to the prediction and 1/3 for a measured image with no similarity. For our measured image, we obtain $\mathrm{MSE} = 0.0078$.

5.7 Discussion

The visibility of our dip is 0.56, the low value of which results from the high background in our experiment. This background is caused by the large numerical aperture of the multi-mode fibres in arms B and C; with many more single counts in

B and C, we observe more false four-fold coincidences that do not come from actual correlated events. Background counts typically make up approximately 25% of the expected coincidence counts, and up to 90% of the coincidences detected in the middle of the HOM dip, skewing the dip visibility significantly. Using fibres with smaller cores and minimizing outside sources of infrared light would result in a more accurate visibility measurement.

Our experiment suffers from low count rates due in large part to measuring a single pixel at a time. In the case of the two-pixel image, we can at maximum detect $p = 50\%$ of the total single counts at any one time; in the four-pixel case, that number is 25%. As this reduction occurs in both arms A and D, and because the detection of these modes also reduces the counts in arms B and C by the same amount, we see a p^4 reduction in the four-fold coincidences, which in the four-pixel case is a factor of 0.004. For this reason, increasing the resolution of the image makes it prohibitively time-consuming to obtain sufficient counts.

This experiment constitutes the first implementation of ghost imaging using independent photons. While we do use the same laser to produce both pairs of entangled photons, the result would be identical using two different lasers.

5.7.1 Expected Counts

During the course of our experiment, we estimated the number of four-fold coincidences expected based on the number of two-fold coincidences observed. We use a similar calculation to that used in Chapter 3:

$$C_{4\mathrm{W}} = \frac{1}{R}\left(C_{\mathrm{AB}}C_{\mathrm{CD}} + C_{\mathrm{AC}}C_{\mathrm{BD}}\right). \tag{5.11}$$

However, the number of expected four-folds was consistently higher than the number of measured four-folds. The expected counts should be identical (within error) to the measured counts outside the HOM dip. (Obviously the measured counts inside the dip should be lower than the expected counts due to the interference.) As seen in Fig. 5.5, the measured counts outside the dip never reach the level of the expected counts.

Ideally, the cause of this discrepancy could be isolated, and the calculation of expected counts could be adjusted accordingly; however, we were unable to isolate the specific cause. To attempt to isolate the cause, we performed a measurement at several different pump powers and observed a variation in the discrepancy between measured and expected counts. As seen in Fig. 5.6, the gap widens when the power of the UV pump is increased.

To mitigate the effects of pump power, we sought to select a power at which to perform the experiment that minimised the discrepancy; however, selecting too

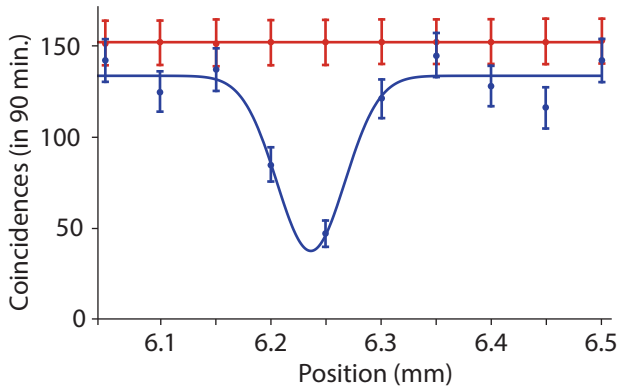

Figure 5.5: **Comparison between expected and measured counts.** The measured four-fold coincidences are shown in blue, while the corresponding expected four-fold coincidences are shown in red. Error bars correspond to Poisson statistics.

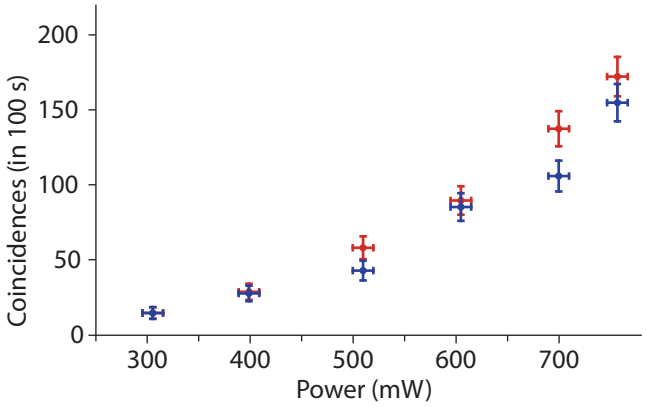

Figure 5.6: **Coincidences vs. UV pump power.** The measured four-fold coincidences are shown in blue, while the corresponding expected four-fold coincidences are shown in red. Vertical error bars correspond to Poisson statistics, while horizontal error bars correspond to the uncertainty on the power meter.

low a pump power would result in very long integration times required to obtain sufficient statistics. As an attempt to balance these two competing goals, the final data was taken at 360 mW.

We also observe a variation in the number of expected counts based on which pixel is being measured. This is due to a variation in the number of two-way coincidences measured at each pixel, which can occur when the light is not perfectly centred on the hologram.

Prior to performing the experiment, we align the hologram to the light using the computer to ensure that we see equal two-way coincidences on all pixels. However, due to the low count rates, the experiment runs for 24+ hours, leaving ample time for the light to drift. Even a slight drift off centre can cause a significant variation in the expected counts. This could be rectified by periodically realigning the hologram programatically, though this was not done in our experiment.

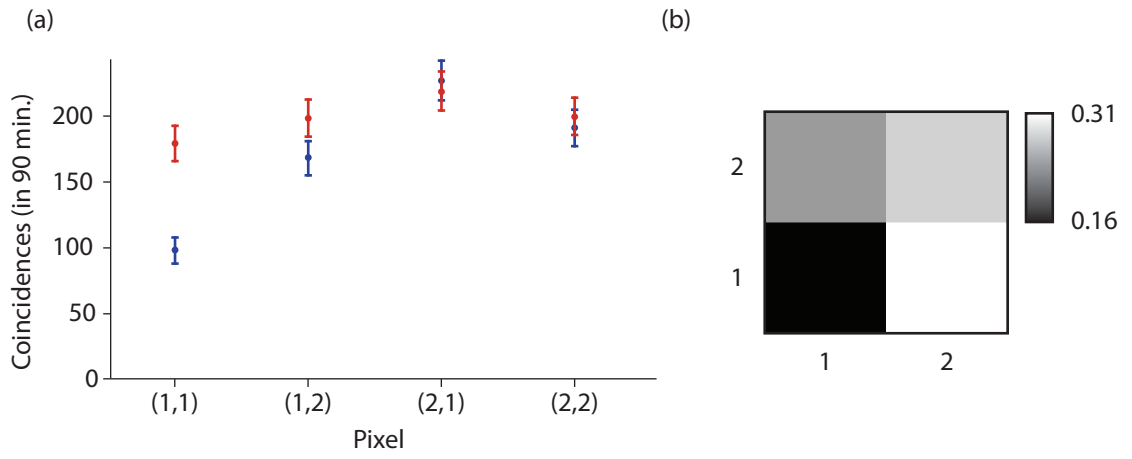

Figure 5.7: **Variation of expected counts by pixel.** (a) Measured counts (blue) compared to expected counts (red) based on pixel measured. The expected counts vary but by less than the measured counts. (b) The reconstructed image based on the ratio between measured and expected counts. We still see contrast reversal, but with slightly lower contrast.

As we do observe a variation in the expected counts, we must ensure that this has not affected the result; i.e., do the expected counts form the same pattern as the measured counts, invalidating our data? Figure 5.7(a) shows the number of expected counts compared to the measured counts for each pixel. Both sets of counts show the same trend, though the expected counts vary less than the measured counts. To confirm that the measured effect is real, we use the ratio between the measured counts and the expected counts to reconstruct the image. As shown in Fig. 5.7(b), we still see distinct contrast reversal, albeit at a slightly lower contrast than the regular reconstructed image. This indicates that the effect is likely to be real.

Chapter 6

Conclusions

Spatial states of light have great potential in quantum information applications, particularly in quantum communication. This is due in large part to the fact that there exist in principle infinite spatial modes, allowing for large information capacity per photon. However, there is significant progress to be made in the implementation of quantum processes that are required for communication in high-dimensional spatial states.

Entanglement swapping and teleportation play a key role in quantum communication, allowing information to be transferred over longer distances. They are a key component in quantum repeaters, which allow the implementation of networks for long-distance communcation. Thus, developing these technologies for spatial states of light is integral to using such states in practical applications.

One current limitation in this area is the scalability of the system. The count rates rely on the efficiency of generation and detection of each OAM mode, which is typically lower for larger OAM. In our particular case of detecting four-photon coincidences, the count rates scale as a power of four, i.e., if the efficiency of a single photon event is η, then the efficiency of a four-photon coincidence event is η^4. This drastically reduces the count rates as well as the signal-to-noise ratios, resulting in long measurement times and large errors. This could be overcome in a number of ways; for example, superconducting nanowire detectors can have an efficiency $\geq 95\%$, which would be an enormous improvement over the photon detectors used in this work, which had an efficiency of $\approx 60\%$. Increasing the generation efficiency would also greatly improve our count rates; for example, periodically poled KTP crystal has a higher downconversion efficiency than BBO, though it also has a lower damage threshold, which would partially limit the improvement.

In this thesis, we began with the main component for teleportation of photon states: Hong-Ou-Mandel interference in a beamsplitter. We confirmed that this component produces the desired filtering of anti-symmetric spatial states when postselected for one photon in each output mode.

We then placed this component in a four-photon system, interfering two of the photons, one from each entangled pair. We then used the interference to entangle the two outer photons, accomplishing entanglement swapping of two-dimensional spatial states of light. This simultaneously accomplishes teleportation of two-dimensional spatial states as well.

However, for high-dimensional spatial states, this interference does not produce pure entanglement swapping or teleportation. To do this, we require a method for projecting into high-dimensional anti-symmetric states. We proposed one such method that was outside the scope of this thesis but would theoretically produce the desired result.

Finally, we used the entanglement created between the two non-interacting photons to perform ghost imaging. Due to the unique behaviour of the interference between these states, we obtain a contrast-reversed ghost image. This represents the first realisation of ghost imaging in a four-photon system, and the first instance of ghost imaging wherein the two photons involved truly never interacted.

APPENDICES

Appendix A

Aligning a four-photon system

A large portion of the work that went into this thesis consisted of aligning and re-aligning a four-photon system. Spending several years optimising a system provides a wealth of knowledge that will quickly become useless unless passed on. Here I will provide an outline of the steps needed to align two pairs of entangled photons and interfere one from each pair on a beamsplitter.

A.1 Upconversion

The first component of the system is the nonlinear crystal used for upconversion of the infrared light. In this case we use a 0.5-mm-thick BBO crystal, but any crystal phase-matched for the appropriate wavelength will do. For BBO, phase-matching is controlled by the angle of incidence of the light. Both the horizontal and vertical angles of the crystal can be tuned to maximize the UV output as measured at a power meter.

The light is focused into the crystal to increase the upconversion efficiency; however, the birefringence in the crystal causes ellipticity in the beam if the focusing is too strong, so we chose a focal length of 75 mm. The crystal should be aligned exactly in the focus. This is made easier by placing the crystal on a translation stage; the z position can then be tuned to maximize UV output as measured at a power meter.

After the crystal, the remaining infrared light is filtered out using two consecutive bandpass filters centred at 405 nm. As we believe most of the background noise in the experiment arose from leftover infrared pump beam, I would advise perhaps an additional filter or some better means by which to remove the excess light.

The UV beam is then focused into a 100-μm circular aperture in order to remove any ellipticity produced by the focusing through the upconversion crystal. We placed the aperture on a three-axis translation stage and looked at the output with a

camera. We aligned the aperture such that we obtained as circular a beam as possible while still being close enough to the focus that we did not produce significant diffraction effects. Ideally, we would have used a smaller aperture as we were not able to cut out all of the elliptical artefacts, but who has time to order and replace new parts when you're on a deadline?

We then re-collimated the light using a 50-mm lens, chosen to slightly reduce the beam waist. The collimated light is then propagated to the first of the two downconversion crystals. At this point it can be helpful to introduce two or more alignment apertures set to the height of the intended collection optics. Ensuring the light exits each newly added mirror and lens parallel to the optical table at the correct height makes later alignment much easier.

Once again, we used BBO crystals for the downconversion, but for both crystals we increased the thickness to 1 mm each in order to increase count rates. Even thicker crystals could further increase counts, but this runs the risk of introducing too much dispersion and jitter, rendering the downconverted photons from different crystals more difficult to interfere. Another possibility for increasing count rates is the use of ppKTP crystals; however, the lower damage threshold for input power is a concern. Determining experimentally the ideal crystals to use would have been an interesting area to explore had we not been confined to the oppressive publication-churning machinations of modern academia.

After aligning the UV pump roughly through the first BBO crystal, a dichroic mirror is placed at 45° in the beam such that the UV is reflected through a second BBO crystal. We chose to place the second BBO 30 cm from the first as this allows for easy path length matching. The downconverted light from the first crystal must travel the same distance to the beamsplitter as the sum of the distance the UV light travels between the first and second crystal and the distance the downconverted light travels from the second crystal to the beamsplitter. We also must image the downconverted light from each crystal to the beamsplitter, requiring two different $2f_1$–$2f_2$ systems that produce the same magnification. The choice of a 30-cm separation between the crystals enables us to use the convenient focal lengths of $f_1 = 200$ mm, $f_2 = 400$ mm for the first crystal and $f_1 = 150$ mm, $f_2 = 300$ mm for the second crystal.

A.2 Downconversion

We will now discuss the alignment of downconverted light from the first crystal; the alignment of the downconversion from the second crystal is much the same, with slightly different focal lengths as stated above.

In order to ensure downconversion is happening in the crystal, we image the light using a Thorlabs CMOS camera with an 810-nm bandpass filter affixed to it. It is easiest to first image the far-field of the downconverted light as it has a distinctive shape that can be manipulated by adjusting the BBO crystal, thus confirming it is in fact downconverted light and not stray background light.

We place a 200-mm lens 200 mm after the crystal. This produces the far-field of the light 200 mm after the lens. The light can be hard to find as it is so dim and can be quite dispersed if the phase-matching is not quite right, so we place a small Allen key in the position at which we expect to find the far-field. We then image the Allen key by placing the camera ≈ 200 mm away, with a short-focal-length lens (e.g., 60 mm) close to the camera. Depending on the size of the camera sensor and the intensity of the downconversion, different focal lengths may have to be used.

It can be helpful to place an iPhone (technically an Android phone would work too, but why would you bother with those?) with its screen turned on leaning against the Allen key and facing the camera; the correct plane to image can then be found easily by moving the lens to obtain a good focused image of the screen. Removing the iPhone, hopefully we see a ring shape of light. If we don't, and we are confident we are imaging the correct plane, tuning the angle of the BBO should produce downconversion. All three angles are fair game: the crystal axis must be correctly aligned to the polarisation of the light, and the pitch and yaw must be adjusted so that the light strikes the crystal at the correct angle for phase-matching.

After finding the far field of the downconverted light, the Allen key can be removed, and we adjust the angle of the crystal until we can only just see a dip in intensity in the middle of the beam. This slightly noncollinear phase-matching results in the highest concentration of photons per square millimetre in our ring, whilst still spatially separating the photon pairs.

It is also a good idea at this time to image the light in the plane of the crystal as well. This can be done by simply moving the camera and lens closer to where the Allen key was. If the 60-mm lens is 60 mm from the far-field and 60 mm from the camera, this implements a $2f_1$–$2f_2$ imaging system. This allows us to check that the downconversion at the crystal is a Gaussian beam.

Now to facilitate later alignment, we place two large apertures in the path of the downconversion, as shown in Fig. A.1. The apertures are placed a sufficient distance from the crystal so that a ring is observed, and therefore the signal and idler photons pass though different irises. Each iris should be placed such that it is vertically centred, and horizontally centred on the brightest part of one side of the ring. The irises must be large enough that when fully opened they do not impact the propagation of the light.

The photon pairs must now be separated. We place a D-shaped mirror in the

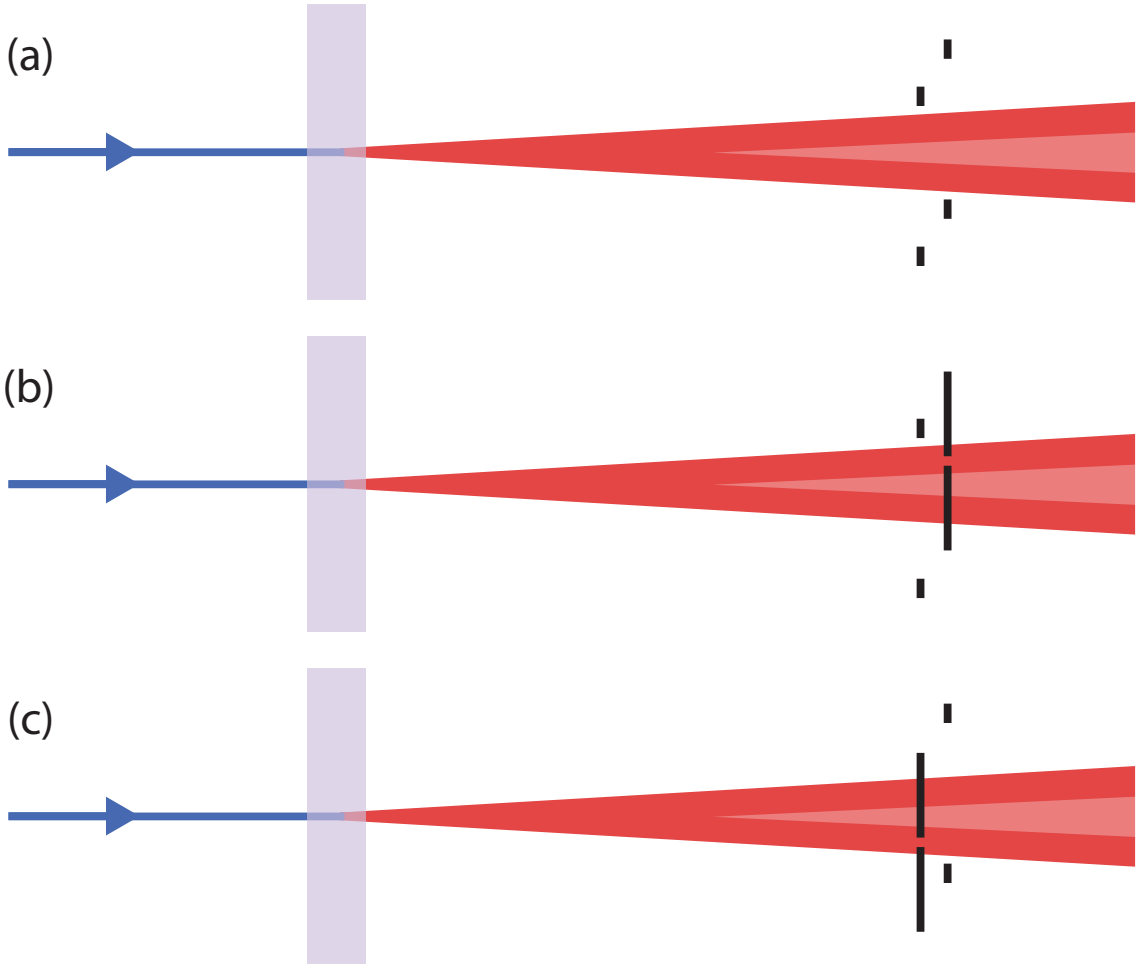

Figure A.1: **Alignment apertures.** (a) Both apertures open. (b) Signal aperture closed down to allow a small circle of light through for alignment. (c) Idler aperture similarly closed down for alignment.

beam as close to the far-field as is possible, though precise positioning is not as important here as one might think. It is very helpful for diagnostic purposes to place the mirror on a translation stage such that it can easily be moved in and out of the beam. The D-mirror should perfectly split the downconverted light down the middle; this can be ensured by imaging the full ring with a camera. Determine on the camera where the centre line of the ring is, place your cursor in that position, and move the D-mirror in from one side until it is aligned with your cursor. It may look as though it is not a perfect semi-circle, but that is often simply an optical illusion; if you have followed the procedure correctly, it is likely aligned correctly. This can be double-checked if needed by taking a screenshot of one semi-circle and then imaging the other semi-circle for comparison.

Shortly after the D-mirror, we place an aperture in each path as an alignment aid. As before, the aperture should be vertically centred, and horizontally centred on the brightest point in the semi-circle. This can be ensured by closing down the relevant aperture near the crystal, imaging the new aperture on the camera, and aligning the new aperture to the light getting through the crystal aperture. It is imperative this alignment is correct, as this two-aperture alignment system will be used extensively for future alignment and re-alignment of the setup.

We label the beam farthest from the second crystal photon A, which will not undergo Hong-Ou-Mandel interference. We place a 400-mm lens 400 mm from the far-field and another 400 mm from SLM A. It is helpful to image the SLM with a camera to ensure that the light is perfectly in focus at the SLM.

With the other photon, labelled B, we place a translation stage with two mirrors on it, each at 45° to the beam and at 90° to each other, immediately after the aperture. This will enable precise path difference alignment later on. It is best to have the translation stage in the middle of its travel for the moment and attempt to place a 400-mm lens 400 mm from the far-field under this condition. We then place a beamsplitter 400 mm after the lens as well, with the beam incident on one plane of the beamsplitter at 90°.

It is worth pointing out that we will require two mirrors for alignment between the second aperture and the beamsplitter in arm B, and between the second aperture and the SLM in arm A. Preferably these mirrors would be a good distance apart in order to provide uncoupled adjustment of the beam angle and position. The mirrors on the translation stage in arm B should never be adjusted if possible, so two other mirrors will have to be included.

A.3 Back-Alignment

At this point, we change perspective and align backwards from our eventual detection optics. We can place a 400-mm lens 400 mm after the SLM (BS), followed by our coupling stage 402 mm after the lens. Our coupling stage is a three-axis precision translation stage with a fibre connector and a 2-mm lens mounted on it. Once again, we will need at least two mirrors to align the angle and position of the beam between the SLM (BS) and stage.

We couple an infrared diode laser into the fibre connected to the stage such that the light propagates out through the 2-mm lens. This light is easier to align due to its higher intensity; it can be seen using an infrared card rather than requiring a camera. First we focus the light on the SLM, and then we propagate it back through the apertures all the way to the crystal. It should be noted that at this time, the SLM should be off and acting simply as a mirror.

The only rule of back-alignment in this experiment is: do not, under any circumstances, touch the mirrors before the second aperture. Assuming you have aligned correctly up until now, touching those mirrors will only ruin everything. For an illustration of which mirrors can be touched at what points during alignment, see Fig. A.2.

Besides that one rule, pretty much everything is fair game. My tendency is to use the mirrors between the SLM and the stage to get the back-aligned spot in the middle of the SLM. Then I use the SLM to align to the second aperture, and I use the mirrors between the second aperture and the SLM to align to the first aperture. But really, anything goes here. As long as you absolutely do not touch the mirrors before the second aperture.

A similar back-alignment procedure can be used for arm B. In this case, I use the mirrors between the BS and the stage to get the back-aligned light going through the beamsplitter centrally at 90° incidence. If desired, the BS can be placed on the intersection of two lines of holes, and two apertures placed at each output port to ensure perfect alignment. Then I use the mirrors between the BS and the second aperture for alignment: the mirror closest to the BS aligns to the second aperture, and the mirror farthest from the BS aligns to the first aperture.

A.4 Finding the Coincidences

Of course, we must complete the above procedure for the other crystal as well. Most importantly, we must ensure that photons B and C overlap extremely well in the beamsplitter. This can be done by splitting the back-alignment laser with

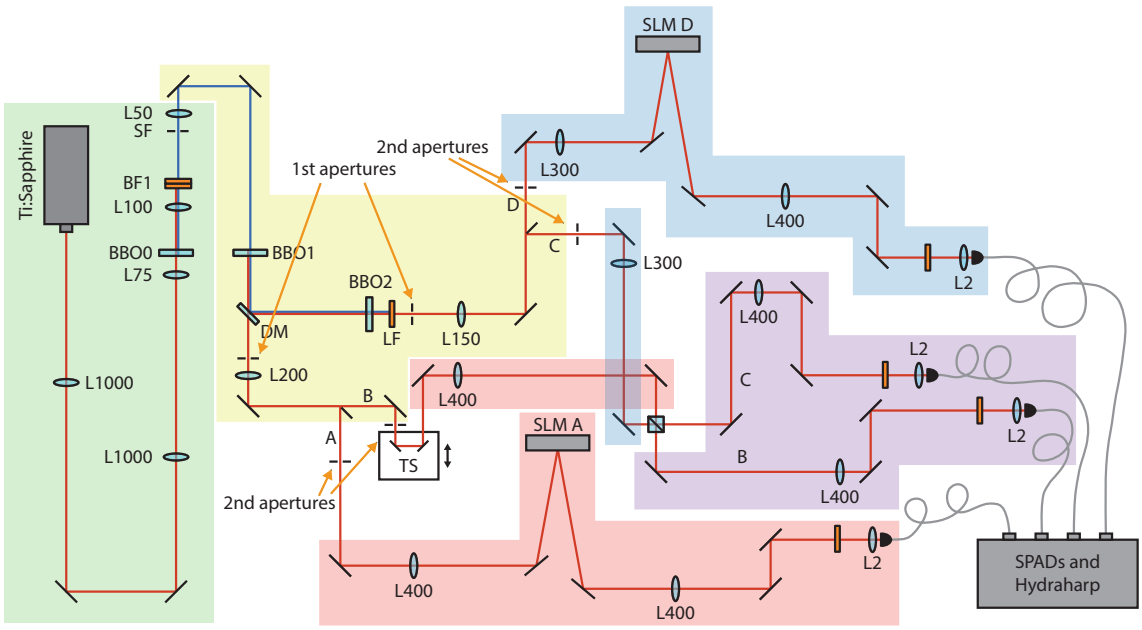

Figure A.2: **When to touch which mirrors.** Green: Upconversion alignment. Yellow: Downconversion alignment. Red: Alignment of singles and coincidences for BBO1. Blue: Alignment of singles and coincidences for BBO2. Purple: Alignment of singles and coincidences for either crystal.

a fibre beamsplitter and sending light back through both stages B and C at once. Typically, the alignment of arm B will have already been set, so I tend to use the mirrors between the BS and stage C to overlap the modes. If the alignment has been done correctly, the light from stage C should end up going through both apertures in arm B. However, make sure not to touch the mirrors in arm B before the BS to achieve this, as this will ruin the alignment of photon B. Similarly, the light from stage B should end up going through both apertures in arm B, as long as the light from stage C is already aligned to them. It is possible to complete this alignment well, but it can be tricky.

Once we are reasonably sure that the system is as aligned as it can be by eye, we place 810-nm filters in front of each of the four stages, to ensure all extraneous light is removed, and we replace the back-alignment laser with single-mode fibres connected to single-photon detectors. We use custom software written in LabVIEW to communicate with the time-tagging system the detectors are plugged into. This allows us to track in real-time the number of singles, two-way coincidences, and four-way coincidences in all channels at the same time.

When we first turn on this software, we hope to see single-channel counts in all four channels. Sometimes the singles can be very low to begin with; if they are so low that it is unclear if they exist at all above the background, blocking the relevant beam path with your hand temporarily can resolve that uncertainty. If any of the channels are lacking counts entirely, the preceding alignment procedures should be

repeated. If you are really struggling, removing the filters can help to find the general area of the single counts.

If we are very lucky, we will also observe two-way coincidences immediately upon turning on the software. However, usually this is not the case. Instead, we must optimise the single-channel counts individually, keeping a constant eye on the two-way coincidences as well until we see a small bump – latch on to that bump! Stop whatever you were doing, and try to make those coincidences grow!

To begin with, it is easiest to optimise the two outer arms, A and D, as they are completely independent of one another and straightforward to align. The three-axis stage, the SLM, and any of the mirrors after the second aperture are fair game.

The inner two arms B and C are not quite so straightforward. The alignment of these two arms together controls all the two-way coincidences (AB, AC, BD, and CD) all at once. We must be careful about whether we are adjusting mirrors before the beamsplitter (between the second aperture and the BS) or after the beamsplitter (between the BS and the stage). We must also be careful about which crystal is producing the counts we are observing.

First, block the first crystal just before the beamsplitter and ensure there are still counts in arms B and C. Then do the same with the second crystal. If either of these actions result in zero counts, go back and check with the camera that there is still downconversion happening at the offending crystal, that there is no clipping before or after the crystal and the beamsplitter, and that the downconverted light is aligned through both apertures. If there's no obvious cause, back-align from both stages all the way back to the offending crystal.

If all is well with the crystals, we can begin optimising channels B and C. Once again, block one of the crystals, let us say crystal 1, and this time use the mirrors after the beamsplitter and the stages to optimise the singles from crystal 2. Here we should be watching coincidences BD and CD very closely. If at any time they increase at all, we should stop caring about the single counts and instead continue increasing the coincidences. This can be done using any of the mirrors after the beamsplitter and the stages, as well as the mirrors and stage from arm D.

Whether we obtain coincidences or not, once we are satisfied with the singles from crystal 2, we can block crystal 2 and optimise crystal 1. However, we can only change the mirrors before the beamsplitter in path B - we absolutely cannot change anything in path C, except at risk of losing what we have from crystal 2.

Ideally, we now have equal singles coming from crystals 1 and 2, and we have found at least some coincidences in each pair of interest. There are a few tricks I use to increase the coincidences.

1. Try tweaking everything just a tiny bit: absolutely every axis on every mirror,

stage, and SLM, excepting those before the second aperture.

2. Generally block one crystal at any given time; however, if you are tweaking mirrors and stages after the beamsplitter, it's a good idea to check on the other crystal every so often.

3. If you increase the coincidences a lot in one arm with a position adjustment, try the corresponding angle adjustment in the same arm, and vice versa. Also try the analogous controls in the other arms, as often a large change in one arm indicates a common problem in the other arms.

4. An excellent strategy is to optimise the singles in one of the outer arms, even if this means partially losing the corresponding coincidences. You can then bring the coincidences back by "walking" the two relevant mirrors prior to the beamsplitter. Walking involves tweaking one axis of one mirror, allowing the coincidences to decrease, and attempting to bring them back with the same axis of the other mirror. This a very effective alignment technique and should always be used when the coincidences are lower than expected to ensure the alignment isn't stuck in a local maximum.

5. A good way to check whether the alignment is at its peak is to adjust the singles in one of the outer arms. As these singles decrease, the corresponding coincidences should also decrease. If one of the coincidences for the relevant crystal begins decreasing before the other, this indicates that arms B and C are not aligned together. Set the outer arm's singles to their highest point, then bring back the coincidences using the mirrors after the beamsplitter.

A.5 Turning on the SLMs

Note that we have not yet turned on the SLMs. Once we are satisfied with the coincidence counts, we can display a plane wave hologram on SLM A, set to an angle of about 6 or 7 μrad. This will move the light in the Gaussian mode into the first diffracted order, leaving some behind. Our singles and coincidences will drop, but not all the way to zero. We now must turn the horizontal angle on the SLM. We will first lose the counts entirely, but then they will come back all at once: this is the first diffracted order. We then do the same on SLM D.

Next, we need to align the holograms on the SLMs so that they are centred on the beam. We have software that allows us to manually move the hologram around, as well as software that automatically finds the centre. We first do it manually to get it close enough for the computer to finish itself. To do this, we place an $\ell = 5$ hologram on SLM A. Detector A can now only see photons that started out as $\ell = -5$, while B

and C are still only seeing photons that started out as $\ell = 0$, meaning there should be no coincidences. We move the hologram on the SLM until the coincidences drop to nearly zero, which indicates the hologram is centred accurately enough to change the $\ell = -5$ photons to $\ell = 0$. We then change the hologram to $\ell = 4$ and repeat, all the way down to $\ell = 1$. We then perform the same procedure on SLM D. After the rough alignment by hand, our autoalign software can find the absolute best hologram position and angle.

At this point, it's worth tweaking the mirrors and stages again by hand as we've changed a lot with the SLMs. If nothing gets better, great! We're aligned. But typically we will be able to increase the coincidences at least a little bit by repeating the alignment in the previous section. Once we are satisfied we've done all we can, we run autoalign one last time.

A.6 Bringing It All Together

Note that we have never mentioned trying to optimise four-way coincidences. That's because you get them for free! If both of your crystals are pumped by the same source, and both are aligned for two-way coincidences, then you should automatically see four-fold coincidences as your alignment starts to improve. Don't be too optimistic, though: 20 four-ways per second with the SLMs off is the best you can hope for.

Remember that we also have not matched the path lengths up. To do this, we scan the translation stage over as large and detailed a range as we have time for with both SLMs set to $\ell = 0$, or even turned off if you want to do it more quickly. It can be difficult to find the dip, so be patient. When you come in one morning after an overnight run over the entire range of the stage to find no hint of a dip, try not to rip the beamsplitter off the table and smash it on the floor. Instead, try doing several smaller range scans with more detail – the dip can be quite narrow depending on what filter widths you are using.

Once we have found the dip, we are ready to perform our actual experiment! Change the single-mode fibres in arms B and C for multi-mode fibres, and start the measurements. Congrats. You should only have to come back and repeat this alignment procedure once or twice a day for the next several months of measurements. It's not that frustrating, not even when one day all the counts in one arm are completely gone, and it turns out a ghost has come in the night and unscrewed one of your mirrors entirely. However, I will admit it does get a tiny bit frustrating when that happens a second time with a different mirror. But really, besides that, it's plenty of fun. Good luck!

References

[1] Einstein, A., Podolsky, B. & Rosen, N. Can quantum-mechanical description of physical reality be considered complete? *Physical Review* **47**, 777 (1935).

[2] Bell, J. S. On the Einstein-Podolsky-Rosen paradox. *Physics* **1**, 195 (1964).

[3] Clauser, J. F., Horne, M. A., Shimony, A. & Holt, R. A. Proposed experiment to test local hidden-variable theories. *Physical Review Letters* **23**, 880 (1969).

[4] Aspect, A., Grangier, P. & Roger, G. Experimental tests of realistic local theories via Bell's theorem. *Physical Review Letters* **47**, 460 (1981).

[5] Ou, Z. & Mandel, L. Violation of Bell's inequality and classical probability in a two-photon correlation experiment. *Physical Review Letters* **61**, 50 (1988).

[6] Weihs, G., Jennewein, T., Simon, C., Weinfurter, H. & Zeilinger, A. Violation of Bell's inequality under strict Einstein locality conditions. *Physical Review Letters* **81**, 5039 (1998).

[7] Rowe, M. A. *et al.* Experimental violation of a Bell's inequality with efficient detection. *Nature* **409**, 791 (2001).

[8] Ansmann, M. *et al.* Violation of Bell's inequality in Josephson phase qubits. *Nature* **461**, 504 (2009).

[9] Dada, A. C., Leach, J., Buller, G. S., Padgett, M. J. & Andersson, E. Experimental high-dimensional two-photon entanglement and violations of generalized Bell inequalities. *Nature Physics* **7**, 677 (2011).

[10] Hensen, B. *et al.* Loophole-free Bell inequality violation using electron spins separated by 1.3 kilometres. *Nature* **526**, 682 (2015).

[11] Shalm, L. K. *et al.* Strong loophole-free test of local realism. *Physical Review Letters* **115**, 250402 (2015).

[12] Ringbauer, M. *et al.* Measurements on the reality of the wavefunction. *Nature Physics* **11**, 249 (2015).

[13] Ried, K. *et al.* A quantum advantage for inferring causal structure. *Nature Physics* **11**, 414 (2015).

[14] Fitzsimons, J. F., Jones, J. A. & Vedral, V. Quantum correlations which imply causation. *Scientific Reports* **5**, 18281 (2015).

[15] Nielsen, M. A. & Chuang, I. L. *Quantum Computation and Quantum Information* (Cambridge Univ. Press, 2000).

[16] Shor, P. W. Proceedings of the 35th annual symposium on foundations of computer science. *IEEE Computer Society Press, Santa Fe, NM* (1994).

[17] Parker, S. & Plenio, M. B. Efficient factorization with a single pure qubit and logN mixed qubits. *Physical Review Letters* **85**, 3049 (2000).

[18] Lanyon, B. P. *et al.* Experimental demonstration of a compiled version of Shor's algorithm with quantum entanglement. *Physical Review Letters* **99**, 250505 (2007).

[19] Lu, C.-Y., Browne, D. E., Yang, T. & Pan, J.-W. Demonstration of a compiled version of Shor's quantum factoring algorithm using photonic qubits. *Physical Review Letters* **99**, 250504 (2007).

[20] Politi, A., Matthews, J. C. & O'brien, J. L. Shor's quantum factoring algorithm on a photonic chip. *Science* **325**, 1221–1221 (2009).

[21] Monz, T. *et al.* Realization of a scalable Shor algorithm. *Science* **351**, 1068 (2016).

[22] Martín-López, E. *et al.* Experimental realization of Shor's quantum factoring algorithm using qubit recycling. *Nature Photonics* **6**, 773 (2012).

[23] Gisin, N., Ribordy, G., Tittel, W. & Zbinden, H. Quantum cryptography. *Reviews of Modern Physics* **74**, 145 (2002).

[24] Scarani, V. *et al.* The security of practical quantum key distribution. *Reviews of Modern Physics* **81**, 1301 (2009).

[25] Pan, J.-W., Bouwmeester, D., Weinfurter, H. & Zeilinger, A. Experimental Entanglement Swapping: Entangling Photons That Never Interacted. *Physical Review Letters* **80**, 3891 (1998).

[26] Shi, B.-S., Jiang, Y.-K. & Guo, G.-C. Optimal entanglement purification via entanglement swapping. *Physical Review A* **62**, 054301 (2000).

[27] Jennewein, T., Weihs, G., Pan, J.-W. & Zeilinger, A. Experimental Nonlocality Proof of Quantum Teleportation and Entanglement Swapping. *Physical Review Letters* **88**, 017903 (2001).

[28] de Riedmatten, H. *et al.* Long-distance entanglement swapping with photons from separated sources. *Physical Review A* **71**, 050302 (2005).

[29] Kaltenbaek, R., Prevedel, R., Aspelmeyer, M. & Zeilinger, A. High-fidelity entanglement swapping with fully independent sources. *Physical Review A* **79**, 040302 (2009).

[30] Ma, X.-S. *et al.* Experimental delayed-choice entanglement swapping. *Nature Physics* **8**, 479 (2012).

[31] Mair, A., Vaziri, A., Weihs, G. & Zeilinger, A. Entanglement of the orbital angular momentum states of photons. *Nature* **412**, 313 (2001).

[32] Leach, J. *et al.* Quantum Correlations in Optical Angle-Orbital Angular Momentum Variables. *Science* **329**, 662 (2010).

[33] Pors, B.-J., Monken, C. H., Eliel, E. R. & Woerdman, J. P. Transport of orbital-angular-momentum entanglement through a turbulent atmosphere. *Optics Express* **19**, 6671 (2011).

[34] Edgar, M. P. *et al.* Imaging high-dimensional spatial entanglement with a camera. *Nature Communications* **3**, 984 (2012).

[35] Fickler, R. *et al.* Interface between path and orbital angular momentum entanglement for high-dimensional photonic quantum information. *Nature Communications* **5**, 4502 (2014).

[36] Tittel, W., Brendel, J., Zbinden, H. & Gisin, N. Violation of Bell inequalities by photons more than 10 km apart. *Physical Review Letters* **81**, 3563–3566 (1998).

[37] Brendel, J., Gisin, N., Tittel, W. & Zbinden, H. Pulsed energy-time entangled twin-photon source for quantum communication. *Physical Review Letters* **82**, 2594–2597 (1999).

[38] Tittel, W., Brendel, J., Zbinden, H. & Gisin, N. Quantum cryptography using entangled photons in energy-time Bell states. *Physical Review Letters* **84**, 4737–4740 (2000).

[39] Marcikic, I. *et al.* Time-bin entangled qubits for quantum communication created by femtosecond pulses. *Phys. Rev. A* **66**, 062308 (2002).

[40] Marcikic, I. *et al.* Distribution of time-bin entangled qubits over 50 km of optical fiber. *Physical Review Letters* **93**, 180502 (2004).

[41] Martin, A. *et al.* Cross time-bin photonic entanglement for quantum key distribution. *Phys. Rev. A* **87**, 020301 (2013).

[42] Donohue, J. M., Agnew, M., Lavoie, J. & Resch, K. J. Coherent Ultrafast Measurement of Time-Bin Encoded Photons. *Physical Review Letters* **111**, 153602 (2013).

[43] Bennett, C. H. & Wiesner, S. J. Communication via one-and two-particle operators on Einstein-Podolsky-Rosen states. *Physical Review Letters* **69**, 2881 (1992).

[44] Mattle, K., Weinfurter, H., Kwiat, P. G. & Zeilinger, A. Dense coding in experimental quantum communication. *Physical Review Letters* **76**, 4656 (1996).

[45] Barreiro, J. T., Wei, T.-C. & Kwiat, P. G. Beating the channel capacity limit for linear photonic superdense coding. *Nature Physics* **4**, 282 (2008).

[46] Lütkenhaus, N., Calsamiglia, J. & Suominen, K. A. Bell measurements for teleportation. *Physical Review A* **59**, 3295 (1999).

[47] Bennett, C.H. & Brassard, G. Quantum cryptography: Public-key distribution and coin tossing. *Proc. IEEE Int. Conf. Comp. Syst. Sig. Process., Bangalore, India*, 175 (1984).

[48] Ekert, A. K. Quantum cryptography based on Bell's theorem. *Physical Review Letters* **67**, 661 (1991).

[49] Pittman, T. B., Shih, Y. H., Strekalov, D. V. & Sergienko, A. V. Optical imaging by means of two-photon quantum entanglement. *Physical Review A* **52**, R3429 (1995).

[50] Bennink, R. S., Bentley, S. J. & Boyd, R. W. "Two-Photon" Coincidence Imaging with a Classical Source. *Physical Review Letters* **89**, 3 (2002).

[51] Bennett, C. H. *et al.* Teleporting an unknown quantum state via dual classical and Einstein-Podolsky-Rosen channels. *Physical Review Letters* **70**, 1895 (1993).

[52] Bouwmeester, D., Pan, J. W., Mattle, K., Eibl, M. & Weinfurter, H. Experimental quantum teleportation. *Nature* **390**, 575 (1997).

[53] Wang, X.-L. *et al.* Quantum teleportation of multiple degrees of freedom of a single photon. *Nature* **518**, 516 (2015).

[54] Graham, T. M., Bernstein, H. J., Wei, T.-C., Junge, M. & Kwiat, P. G. Superdense teleportation using hyperentangled photons. *Nature Communications* **6**, 7185 (2015).

[55] Jin, X.-M. *et al.* Experimental free-space quantum teleportation. *Nature Photonics* **4**, 376 (2010).

[56] Yin, J. *et al.* Quantum teleportation and entanglement distribution over 100-kilometre free-space channels. *Nature* **488**, 185 (2012).

[57] Ma, X.-S. *et al.* Quantum teleportation over 143 kilometres using active feed-forward. *Nature* **489**, 269 (2012).

[58] Marcikic, I., de Riedmatten, H., Tittel, W., Nature, H. Z. & Gisin, N. Long-distance teleportation of qubits at telecommunication wavelengths. *Nature* **421**, 509 (2003).

[59] Takesue, H. *et al.* Quantum teleportation over 100 km of fiber using highly efficient superconducting nanowire single-photon detectors. *Optica* **2**, 832 (2015).

[60] Sun, Q.-C. *et al.* Quantum teleportation with independent sources and prior entanglement distribution over a network. *Nature Photonics* **10**, 671 (2016).

[61] Valivarthi, R. *et al.* Quantum teleportation across a metropolitan fibre network. *Nature Photonics* **10**, 676 (2016).

[62] Ren, J.-G. *et al.* Ground-to-satellite quantum teleportation. *Nature* **549**, 70 (2017).

[63] Hong, C. K., Ou, Z. Y. & Mandel, L. Measurement of subpicosecond time intervals between two photons by interference. *Physical Review Letters* **59**, 2044 (1987).

[64] Allen, L., Beijersbergen, M. W. & Spreeuw, R. Orbital angular momentum of light and the transformation of Laguerre-Gaussian laser modes. *Physical Review A* **45**, 8185 (1992).

[65] Padgett, M. J. & Courtial, J. Poincaré-sphere equivalent for light beams containing orbital angular momentum. *Optics Letters* **24**, 430 (1999).

[66] Yao, A. M. & Padgett, M. J. Orbital angular momentum: origins, behavior and applications. *Advances in Optics and Photonics* **3**, 161 (2011).

[67] Leuenberger, M. N. & Loss, D. Quantum computing in molecular magnets. *Nature* **410**, 789 (2001).

[68] Walther, P. *et al.* Experimental one-way quantum computing. *Nature* **434**, 169 (2005).

[69] Kok, P. *et al.* Linear optical quantum computing with photonic qubits. *Reviews of Modern Physics* **79**, 135 (2007).

[70] Lanyon, B., Barbieri, M., Almeida, M. & White, A. Experimental quantum computing without entanglement. *Physical Review Letters* **101**, 200501 (2008).

[71] Bennett, C. H. Quantum cryptography using any two nonorthogonal states. *Physical Review Letters* **68**, 3121–3124 (1992).

[72] Muller, A., Breguet, J. & Gisin, N. Experimental demonstration of quantum cryptography using polarized photons in optical fibre over more than 1 km. *Europhysics Letters* **23**, 383 (1993).

[73] Muller, A., Zbinden, H. & Gisin, N. Quantum cryptography over 23 km in installed under-lake telecom fibre. *Europhysics Letters* **33**, 335 (1996).

[74] Bethune, D. S. & Risk, W. P. An autocompensating fiber-optic quantum cryptography system based on polarization splitting of light. *IEEE Journal of Quantum Electronics* **36**, 340 (2000).

[75] Jennewein, T., Simon, C., Weihs, G., Weinfurter, H. & Zeilinger, A. Quantum cryptography with entangled photons. *Physical Review Letters* **84**, 4729 (2000).

[76] Kurtsiefer, C. *et al.* Quantum cryptography: A step towards global key distribution. *Nature* **419**, 450 (2002).

[77] Leach, J. *et al.* Violation of a Bell inequality in two-dimensional orbital angular momentum state-spaces. *Optics Express* **17**, 8287 (2009).

[78] Koppens, F. *et al.* Driven coherent oscillations of a single electron spin in a quantum dot. *Nature* **442**, 766 (2006).

[79] Warren, W. S. The usefulness of NMR quantum computing. *Science* **277**, 1688 (1997).

[80] Devoret, M. H. & Schoelkopf, R. J. Superconducting Circuits for Quantum Information: An Outlook. *Science* **339**, 1169 (2013).

[81] Gibson, G. *et al.* Free-space information transfer using light beams carrying orbital angular momentum. *Optics Express* **12**, 5448 (2004).

[82] Franke-Arnold, S., Allen, L. & Padgett, M. Advances in optical angular momentum. *Laser & Photonics Reviews* **2**, 299 (2008).

[83] Malik, M. *et al.* Influence of atmospheric turbulence on optical communications using orbital angular momentum for encoding. *Optics Express* **20**, 13195 (2012).

[84] Wang, J. *et al.* Terabit free-space data transmission employing orbital angular momentum multiplexing. *Nature Photonics* **6**, 488 (2012).

[85] Leach, J., Padgett, M. J., Barnett, S. M., Franke-Arnold, S. & Courtial, J. Measuring the Orbital Angular Momentum of a Single Photon. *Physical Review Letters* **88**, 257901 (2002).

[86] Franke-Arnold, S., Barnett, S. M., Padgett, M. J. & Allen, L. Two-photon entanglement of orbital angular momentum states. *Physical Review A* **65**, 033823 (2002).

[87] Paterson, C. Atmospheric turbulence and orbital angular momentum of single photons for optical communication. *Physical Review Letters* **94**, 153901 (2005).

[88] Peeters, W. H., Verstegen, E. J. K. & van Exter, M. P. Orbital angular momentum analysis of high-dimensional entanglement. *Physical Review A* **76**, 042302 (2007).

[89] Di Lorenzo Pires, H., Florijn, H. C. B. & van Exter, M. P. Measurement of the Spiral Spectrum of Entangled Two-Photon States. *Physical Review Letters* **104**, 020505 (2010).

[90] Nagali, E. *et al.* Experimental Optimal Cloning of Four-Dimensional Quantum States of Photons. *Physical Review Letters* **105**, 073602 (2010).

[91] Vértesi, T., Pironio, S. & Brunner, N. Closing the Detection Loophole in Bell Experiments Using Qudits. *Physical Review Letters* **104**, 060401 (2010).

[92] Agnew, M., Leach, J., McLaren, M., Roux, F. S. & Boyd, R. W. Tomography of the quantum state of photons entangled in high dimensions. *Physical Review A* **84**, 062101 (2011).

[93] Miatto, F. M., Yao, A. M. & Barnett, S. M. Full characterization of the quantum spiral bandwidth of entangled biphotons. *Physical Review A* **83**, 033816 (2011).

[94] Krenn, M. *et al.* Generation and confirmation of a (100 x 100)-dimensional entangled quantum system. *Proceedings of the National Academy of Sciences* **111**, 6243 (2014).

[95] Bolduc, E., Gariepy, G. & Leach, J. Direct measurement of large-scale quantum states via expectation values of non-Hermitian matrices. *Nature Communications* **7**, 10439 (2016).

[96] Malik, M. *et al.* Multi-photon entanglement in high dimensions. *Nature Photonics* **10**, 248 (2016).

[97] Leach, J., Bolduc, E., Gauthier, D. J. & Boyd, R. W. Secure information capacity of photons entangled in many dimensions. *Physical Review A* **85**, 060304 (2012).

[98] Mafu, M. *et al.* Higher-dimensional orbital-angular-momentum-based quantum key distribution with mutually unbiased bases. *Physical Review A* **88**, 032305 (2013).

[99] Mirhosseini, M. *et al.* High-dimensional quantum cryptography with twisted light. *New Journal of Physics* **17**, 033033 (2015).

[100] Nicolas, A. *et al.* A quantum memory for orbital angular momentum photonic qubits. *Nature Photonics* **8**, 234 (2014).

[101] Ding, D.-S. *et al.* Quantum Storage of Orbital Angular Momentum Entanglement in an Atomic Ensemble. *Physical Review Letters* **114**, 050502 (2015).

[102] Bain, L. J. & Engelhardt, M. *Introduction to probability and mathematical statistics* (Brooks/Cole, 1987).

[103] Berkhout, G. C. G., Lavery, M. P. J., Courtial, J., Beijersbergen, M. W. & Padgett, M. J. Efficient Sorting of Orbital Angular Momentum States of Light. *Physical Review Letters* **105**, 153601 (2010).

[104] Turnbull, G., Robertson, D., Smith, G., Allen, L. & Padgett, M. The generation of free-space laguerre-gaussian modes at millimetre-wave frequencies by use of a spiral phaseplate. *Optics Communications* **127**, 183 (1996).

[105] James, D. F. V., Kwiat, P. G., Munro, W. J. & White, A. G. Measurement of qubits. *Physical Review A* **64**, 052312 (2001).

[106] Schrödinger, E. Discussion of probability relations between separated systems, in *Mathematical Proceedings of the Cambridge Philosophical Society*, **31**, 555 (Cambridge University Press, 1935).

[107] Gühne, O. & Tóth, G. Entanglement detection. *Physics Reports* **474**, 1 (2009).

[108] Torres, J. P., Alexandrescu, A. & Torner, L. Quantum spiral bandwidth of entangled two-photon states. *Physical Review A* **68**, 050301 (2003).

[109] Bennett, C. H. *et al.* Remote State Preparation. *Physical Review Letters* **87**, 077902 (2001).

[110] Bennett, C. H., Bernstein, H. J., Popescu, S. & Schumacher, B. Concentrating partial entanglement by local operations. *Physical Review A* **53**, 2046 (1996).

[111] Werner, R. F. Quantum states with Einstein-Podolsky-Rosen correlations admitting a hidden-variable model. *Physical Review A* **40**, 4277 (1989).

[112] Zhang, Y. *et al.* Engineering two-photon high-dimensional states through quantum interference. *Science Advances* **2**, e1501165 (2016).

[113] Kok, P. & Lovett, B. W. *Introduction to optical quantum information processing* (Cambridge University Press, 2010).

[114] Irvine, W. T., Linares, A. L., de Dood, M. J. & Bouwmeester, D. Optimal quantum cloning on a beam splitter. *Physical Review Letters* **92**, 047902 (2004).

[115] Nagali, E. *et al.* Optimal quantum cloning of orbital angular momentum photon qubits through Hong–Ou–Mandel coalescence. *Nature Photonics* **3**, 720 (2009).

[116] Kwiat, P. G., Steinberg, A. M. & Chiao, R. Y. Observation of a "quantum eraser": A revival of coherence in a two-photon interference experiment. *Physical Review A* **45**, 7729 (1992).

[117] Pittman, T. *et al.* Can two-photon interference be considered the interference of two photons? *Physical Review Letters* **77**, 1917 (1996).

[118] Karimi, E. *et al.* Exploring the quantum nature of the radial degree of freedom of a photon via Hong-Ou-Mandel interference. *Physical Review A* **89**, 013829 (2014).

[119] Walborn, S. P., de Oliveira, A. N., Padua, S. & Monken, C. H. Multimode Hong-Ou-Mandel Interference. *Physical Review Letters* **90**, 143601 (2003).

[120] Fedrizzi, A. *et al.* Anti-symmetrization reveals hidden entanglement. *New Journal of Physics* **11**, 103052 (2009).

[121] Nagali, E. *et al.* Quantum information transfer from spin to orbital angular momentum of photons. *Physical Review Letters* **103**, 013601 (2009).

[122] Giovannini, D., Romero, J. & Padgett, M. Interference of probability amplitudes: a simple demonstration within the Hong–Ou–Mandel experiment. *Journal of Optics* **16**, 032002 (2014).

[123] Kaltenbaek, R., Blauensteiner, B., Żukowski, M., Aspelmeyer, M. & Zeilinger, A. Experimental interference of independent photons. *Physical Review Letters* **96**, 240502 (2006).

[124] Bechmann-Pasquinucci, H. & Tittel, W. Quantum cryptography using larger alphabets. *Physical Review A* **61**, 062308 (2000).

[125] Thew, R. T., Acin, A., Zbinden, H. & Gisin, N. Bell-type test of energy-time entangled qutrits. *Physical Review Letters* **93**, 010503 (2004).

[126] O'Sullivan-Hale, M. N., Ali Khan, I., Boyd, R. W. & Howell, J. C. Pixel Entanglement: Experimental Realization of Optically Entangled d=3 and d=6 Qudits. *Physical Review Letters* **94**, 753 (2005).

[127] McLaren, M. *et al.* Entangled Bessel-Gaussian beams. *Optics Express* **20**, 23589 (2012).

[128] Kwiat, P. G. & Weinfurter, H. Embedded Bell-state analysis. *Physical Review A* **58**, R2623 (1998).

[129] Barreiro, J. T., Langford, N. K., Peters, N. A. & Kwiat, P. G. Generation of Hyperentangled Photon Pairs. *Physical Review Letters* **95**, 260501 (2005).

[130] Molina-Terriza, G., Torres, J. P. & Torner, L. Twisted photons. *Nature Physics* **3**, 305 (2007).

[131] Goyal, S. K. & Konrad, T. Teleporting photonic qudits using multimode quantum scissors. *Scientific Reports* **3**, 3548 (2013).

[132] Goyal, S. K., Boukama-Dzoussi, P. E., Ghosh, S., Roux, F. S. & Konrad, T. Qudit-Teleportation for photons with linear optics. *Scientific Reports* **4**, 4543 (2014).

[133] Briegel, H. J., Dür, W., Cirac, J. I. & Zoller, P. Quantum Repeaters: The Role of Imperfect Local Operations in Quantum Communication. *Physical Review Letters* **81**, 5932 (1998).

[134] Gonzalez, N., Molina-Terriza, G. & Torres, J. P. How a Dove prism transforms the orbital angular momentum of a light beam. *Optics Express* **14**, 9093 (2006).

[135] Zhang, Y. *et al.* Simultaneous entanglement swapping of multiple orbital angular momentum states of light. *Nature Communications* **8**, 632 (2017).

[136] Walborn, S. P., de Oliveira, A. N., Thebaldi, R. S. & Monken, C. H. Entanglement and conservation of orbital angular momentum in spontaneous parametric down-conversion. *Physical Review A* **69**, 023811 (2004).

[137] Matthews, J. C. F., Politi, A., Stefanov, A. & O'Brien, J. L. Manipulation of multiphoton entanglement in waveguide quantum circuits. *Nature Photonics* **3**, 346 (2009).

[138] Karimi, E. *et al.* Spin-orbit hybrid entanglement of photons and quantum contextuality. *Physical Review A* **82**, 022115 (2010).

[139] Hiesmayr, B. C., de Dood, M. J. A. & Löffler, W. Observation of Four-Photon Orbital Angular Momentum Entanglement. *Physical Review Letters* **116**, 073601 (2016).

[140] Guerreiro, T. *et al.* Interaction of independent single photons based on integrated nonlinear optics. *Nature Communications* **4**, 2324 (2013).

[141] Wootters, W. K. & Zurek, W. H. A single quantum cannot be cloned. *Nature* **299**, 802 (1982).

[142] Gottesman, D. & Chuang, I. L. Demonstrating the viability of universal quantum computation using teleportation and single-qubit operations. *Nature* **402**, 390 (1999).

[143] Riebe, M. *et al.* Deterministic quantum teleportation with atoms. *Nature* **429**, 734 (2004).

[144] Barrett, M. *et al.* Deterministic quantum teleportation of atomic qubits. *Nature* **429**, 737 (2004).

[145] Nielsen, M. A., Knill, E. & Laflamme, R. Complete quantum teleportation using nuclear magnetic resonance. *Nature* **396**, 52 (1998).

[146] Kim, Y.-H., Kulik, S. P. & Shih, Y. Quantum teleportation of a polarization state with a complete Bell state measurement. *Physical Review Letters* **86**, 1370 (2001).

[147] Massar, S. & Popescu, S. Optimal extraction of information from finite quantum ensembles. *Physical Review Letters* **74**, 1259 (1995).

[148] Strekalov, D. V., Sergienko, A. V., Klyshko, D. N. & Shih, Y. H. Observation of Two-Photon "Ghost" Interference and Diffraction. *Physical Review Letters* **74**, 3600 (1995).

[149] Abouraddy, A. F., Saleh, B. E. A., Sergienko, A. V. & Teich, M. C. Role of Entanglement in Two-Photon Imaging. *Physical Review Letters* **87**, 3600 (2001).

[150] Gatti, A., Brambilla, E. & Lugiato, L. A. Entangled Imaging and Wave-Particle Duality: From the Microscopic to the Macroscopic Realm. *Physical Review Letters* **90**, S288–4 (2003).

[151] Gatti, A., Brambilla, E., Bache, M. & Lugiato, L. A. Ghost Imaging with Thermal Light: Comparing Entanglement and Classical Correlation. *Physical Review Letters* **93**, 093602 (2004).

[152] Zerom, P., Chan, K. W. C., Howell, J. C. & Boyd, R. W. Entangled-photon compressive ghost imaging. *Physical Review A* **84**, 061804 (2011).

[153] Shapiro, J. H. & Boyd, R. W. The physics of ghost imaging. *Quantum Information Processing* **11**, 949 (2012).

[154] Bennink, R. S., Bentley, S. J., Boyd, R. W. & Howell, J. C. Quantum and Classical Coincidence Imaging. *Physical Review Letters* **92**, 3 (2004).

[155] Cai, Y. & Zhu, S.-Y. Ghost imaging with incoherent and partially coherent light radiation. *Physical Review E* **71**, 056607 (2005).

[156] Gatti, A. *et al.* Coherent imaging with pseudo-thermal incoherent light. *Journal of Modern Optics* **53**, 739 (2006).

[157] Meyers, R., Deacon, K. S. & Shih, Y. Ghost-imaging experiment by measuring reflected photons. *Physical Review A* **77**, 041801 (2008).

[158] Ferri, F., Magatti, D., Lugiato, L. A. & Gatti, A. Differential Ghost Imaging. *Physical Review Letters* **104**, 253603 (2010).

[159] Meyers, R. E., Deacon, K. S. & Shih, Y. Turbulence-free ghost imaging. *Applied Physics Letters* **98**, 111115 (2011).

[160] Shapiro, J. H. Computational ghost imaging. *Physical Review A* **78**, 061802(R) (2008).

[161] Bromberg, Y., Katz, O. & Silberberg, Y. Ghost imaging with a single detector. *Physical Review A* **79**, 053840 (2009).

[162] Katz, O., Bromberg, Y. & Silberberg, Y. Compressive ghost imaging. *Applied Physics Letters* **95**, 131110 (2009).

[163] Clemente, P., Durán, V., Torres-Company, V., Tajahuerce, E. & Lancis, J. Optical encryption based on computational ghost imaging. *Optics Letters* **35**, 2391 (2010).

[164] Sun, B., Welsh, S. S., Edgar, M. P., Shapiro, J. H. & Padgett, M. J. Normalized ghost imaging. *Optics Express* **20**, 16892 (2012).